Ab initio Study of Alkali Diffusion and Intercalation on Transition Metal Dichalcogenides

Dissertation
zur Erlangung des Doktorgrades
der Mathematisch-Naturwissenschaftlichen Fakultät
der Christian-Albrechts-Universität
zu Kiel

vorgelegt von
Claudia del Pilar Ramírez García

Kiel
2003

Referent/in: Prof. Dr. W. Schattke

Korreferent/in: Priv-Doz. Dr. Eugene E Krasovskii und Prof. Dr. E. Pehlke

Tag der mündlichen Prüfung: 16.12.02

Zum Druck genehmigt: Kiel, den

Der Dekan

To Andrea,
whose love kept me going all this time.

Contents

Chapter 1

Introduction

The transition metal dichalcogenides (TMDCs) exhibit some remarkable properties associated with their reduced dimensionality, that make them suitable materials for fundamental and applied research. These compounds have a layered structure made up of chalcogen-metal-chalcogen layers which are held together by weak van der Waals forces, while within the layers strong covalent and ionic bonding dominates [1, 2]. As a result, the TMDCs exhibit high anisotropy in many of their physical properties and display a rich variety of structural phase transitions associated with charge density waves [1]. In the last years several band structures calculations based on different theoretical methods have been performed for a number of TMDCs [3, 4, 5, 6, 7]. The calculated bands reveal significant dispersion perpendicular to the basal planes supported by p_z orbitals with admixtures of d_{z^2}. Those bands related to layer parallel orbitals show almost no dispersion in this direction. These calculations have been effectively verified by angle-resolved photoemission and inverse photoemission [8, 9, 10].

The two-dimensionality of the TMDCs structure also offers the possibility of forming intercalation compounds by inserting additional atoms or molecules in the van der Waals gap between the layers. This mechanism has provided the basis in the development of new types of batteries [11, 12]. In the first investigation of TMDCs intercalated compounds, these were produced by electrochemical methods. It was only until recently that *in situ* intercalated compounds were obtained by deposition of alkali or noble metal atom onto the surface of TMDCs under ultra-high vacuum conditions [13, 14, 15, 16]. This intercalation method had opened the possibility to study the samples in every step of the reaction by means of angle-resolved photoelectron spectroscopy in combination with scanning tunnelling microscopy, providing new insights into the electronic and geometric structures of these compounds.

Recently in the Institut für Experimentelle und Angewandte Physik der Universität Kiel it was found that deposition of Rb on TMDCs (0001) surfaces leads to the formation of metallic nanowire networks [17, 18]. According to these results rubidium does not intercalate, and the electronic changes commonly associated with alkali intercalation are related to the nanowires. Given the technological relevance of nanostructuring perfect wire networks on surfaces it is desirable to understand the factors that favoured

either the formation of nanowires or the intercalation. Therefore it is necessary to study the dynamical properties of these adsorbate-substrate systems in detail.

The aim of this work is to develop a model of alkali metal intercalation into TMDCs from first-principles total-energy calculations. The main question is, how the alkali atoms find their way from the TMDCs surface to the thermodynamically stable sites in the van der Waals gap? It has been argued that the alkali atoms intercalated from the surface into the bulk through defects and via crystal edges and surface steps [19], but the underlying microscopic processes such as adsorption, diffusion, and nucleation are still poorly undestood. Here the adsorption and diffusion barrier on the $TiSe_2$ (0001) surface will be studied for Li, Na, Rb, and Cs adatoms.

In the present work the system Li-$TiSe_2$ has been chosen, as a prototype of alkali intercalated TMDCs for which *in situ* intercalation seems to be well established [13]. The attention is mainly focused on simulating structural and energy changes during the intercalation process in order to get insight into the alkali ion's favoured movility paths, and to estimate the corresponding activation energies.

Firstly, the adsorption sites of Li on $TiSe_2$ (0001) defect-free surface will be calculated as well as the diffusion barriers. In the second place, the corresponding values in the van der Waals will be also computed. Finally, the most energetically favoured pathway that connects the surface with the van der Waals sites will be investigated. This will be done considering two options: a pathway within $TiSe_2$ interlayer spacing and a pathway across $(10\bar{1}0)$ and $(\bar{1}2\bar{1}1)$ steps.

The core of this work is the density functional theory of Hohenberg, Kohn and Sham, and in particular the local density approximation. The selfconsistent solution of the Kohn-Sham equations together with the determination of the atomic positions will be treated as a minimization problem of the total energy. The electronic configuration of the ground state and the equilibrium positions of the atoms will be computed simultaneously.

This thesis is divided in seven chapters: after this brief introduction, the second chapter will describe the theoretical grounds of this study: density functional theory and the plane-wave pseudopotential method. Chapter 3 is dedicated to review general properties of TMDCs and their intercalated compounds. Results will be also presented concerning the electronic band structures of $TiSe_2$- and $LiTiSe_2$-bulk, which were calculated to verify the reliability of the pseudopotentials generated following the scheme of Troullier and Martins [20]. In Chapter 4 a detailed analysis of Li adatom adsorption and diffusion on $TiSe_2$ (0001) is carried out. Also, the energetical stable sites in the van der Waals gap and the diffusion barrier are calculated. Since the problem of surface diffusion is intimately related to the morphology of the surface on which the diffusion process takes place, the properties of the clean (0001) surface of $TiSe_2$ are first addressed. Chapter 5 is dedicated to explore the most energetically favoured path for Li intercalation from the (0001) defect-free surface through the atomic planes of $TiSe_2$. In Chapter 6 the results regarding diffusion across and along stepped TMDCs surfaces are presented. Finally, the seventh chapter will briefly summarize the results obtained in the present work.

Chapter 2

Theoretical Background

2.1 Introduction

This chapter summarizes briefly the theory on which the calculations of the present work is based. In the last decades the field of the theoretical physics has been enriched by the development of computational methods, making it possible to predict properties of solid-state systems which were formerly inaccessible to theory or experiment. *Ab-initio* calculations attempt to solve the quantum mechanical equations governing the behaviour of the system studied. In contrast to semi-empirical approaches, the *ab-initio* approach does not depend upon any external parameters except the atomic numbers of the constituent atoms to be modelled and cannot therefore be influenced by preconceptions about the final result. However, traditional minimization techniques based on the diagonalization of the Hamiltonian require a computational effort which scales with the cube of the system size N^3 (N the number of atoms), making this kind of calculations too costly to be of significant practical use. However, controlled and well understood approximations can be employed to reduce the complexity to a tractable level and solve efficiently the equations without loosing the parameter-free nature of quantum-mechanical calculations. One such approximations, that within density-functional theory, together with a simple description of the quantum-mechanical effects of exchange and correlation and the pseudopotential approximation, has proved to be remarkably successful and is currently applied by scientists in a wide range of disciplines.

2.2 The many-body Schrödinger equation

The starting point for the description of a system containing N_e electrons with coordinates $\mathbf{r} \equiv \{\mathbf{r}_i\}$ and N_i ions at points $\mathbf{R} \equiv \{\mathbf{R}_I\}$ is to solve the time independent Schrödinger equation:

$$\hat{H}\Psi(\mathbf{r},\mathbf{R}) \quad = \quad E\Psi(\mathbf{r},\mathbf{R}), \tag{2.1}$$

where Ψ is the many-body wave function and E is the total energy. The Hamiltonian $\hat{H}$ is given by the kinetic energy of the nuclei $(\hat{T}_\mathrm{i})$ and electrons $(\hat{T}_\mathrm{e})$, the electrostatic interactions between the nuclei and the electrons (V_ei), and the internuclear (V_ii) and interelectronic repulsions (V_ee).

$$\hat{H} \quad = \quad \hat{T}_\mathrm{i} + \hat{T}_\mathrm{e} + \hat{V}_\mathrm{ei} + \hat{V}_\mathrm{ii} + \hat{V}_\mathrm{ee}, \tag{2.2}$$

with

$$\hat{T}_\mathrm{i} = -\sum_{I}^{\mathrm{N_i}} \frac{\hbar^2}{2M_I}\frac{\partial^2}{\partial R_I^2}, \quad \hat{T}_\mathrm{e} = -\sum_{i}^{\mathrm{N_e}} \frac{\hbar^2}{2m_e}\frac{\partial^2}{\partial r_i^2},$$

$$\hat{V}_\mathrm{ii} = \frac{1}{2}\sum_{I,J,I\neq J}^{\mathbf{N_i},\mathbf{N_i}} \frac{e^2}{4\pi\varepsilon_0}\frac{Z_I Z_J}{|R_I - R_J|}, \hat{V}_\mathrm{ee} = \frac{1}{2}\sum_{i,j,i\neq j}^{\mathrm{N_e},\mathrm{N_e}} \frac{e^2}{4\pi\varepsilon_0}\frac{1}{|r_i - r_j|}, \hat{V}_\mathrm{ei} = -\sum_{i,I}^{\mathrm{N_e},\mathrm{N_i}} \frac{e^2}{4\pi\varepsilon_0}\frac{Z_I}{|r_i - R_I|}$$

where M_I and m_e are the masses of the nuclei and electrons, respectively, and Z_I the nuclear charge.

From now on atomic units ($e = m_e = \hbar = 4\pi\varepsilon_0 = 1$) will be used, since they are more convenient for quantum mechanical problems. Length is expressed in Bohrs and energy in hartrees (1 $a_{Bohr} = 5.2917 \times 10^{-11}$ m, 1 Ha = 2 Ryd = 27.2116 eV).

2.3 Born-Oppenheimer Approximation

In a solid the number of particles is greater than 10^{23}, thus it is clear that without an approximation the Schrödinger equation of the solid will be impossible to solve analytically. One of the most important approximations is the Born-Oppenheimer approximation [21], which states that the degrees of freedom of the electrons and the ions can be uncoupled. It is based on the fact that the masses of the nuclei are much greater than the electrons, which will therefore respond almost instantaneously to any change in the potential caused by the movement of the nuclei. Thus, it can be considered that the electrons are moving in a field of fixed nuclei. The total wave function can be expressed as the product of the nuclear and electronic parts:

$$\Psi(\mathbf{r},\mathbf{R}) \quad = \quad \Psi_\mathrm{el}(\mathbf{r}:\mathbf{R})\Psi_\mathrm{i}(\mathbf{R}) \tag{2.3}$$

where the electronic wave function depends on the nuclear positions only parametrically, i.e. a different wave function is defined for each nuclear configuration.

The quantum effects are limited to the electronic wave functions Ψ_{el}, which obeys a simpler Schrödinger equation:

$$\hat{H}_{\rm el}\,\Psi_{\rm el}(\mathbf{r}:\mathbf{R}) \;=\; E^n_{\rm el}(\mathbf{R})\Psi_{\rm el}(\mathbf{r}:\mathbf{R}) \tag{2.4}$$

with

$$\hat{H}_{\rm el} \;=\; \hat{T}_{\rm e}+\hat{V}_{\rm ee}+\hat{V}_{\rm ei}. \tag{2.5}$$

Taking this into account Eq. (2.2) can be expressed as

$$\hat{H} \;=\; \hat{H}_{\rm el}+\hat{T}_{\rm i}+\hat{V}_{\rm ii}. \tag{2.6}$$

Within the Born-Oppenheimer approximation the kinetic energy of the nuclei $T_{\rm i}$ can be separated from the electronic motion, and $V_{\rm ii}$ will be a constant for a fixed configuration $\mathbf{R}_I$ of the nuclei $V_{\rm ii}$. The total energy of the many-body system is simply given by $E_n(\mathbf{R}_I) = E^n_{\rm el}(\mathbf{R}_I) + V_{\rm ii}(\mathbf{R}_I)$, where $E^n_{\rm el}(\mathbf{R}_I)$ is the spectrum of the many-electron Hamiltonian $H_{\rm el}$ (Eq. (2.5)). In the Born-Oppenheimer approximation the assumption is made that the electronic component stays in its ground state, $n = 0$, thus in the following the term (ground-state) *total energy* for a particular configuration $\mathbf{R}_I$ will refer to

$$E(\mathbf{R}_I) \;=\; E^0_{\rm el}(\mathbf{R}_I)+V_{\rm ii}(\mathbf{R}_I) \tag{2.7}$$

Repeating the calculation with a different nuclear arrangement allows the *potential energy surface* to be mapped out and the equilibrium geometry to be found.

To calculate $\Psi_{\rm el}$ in Eq. (2.4) there are many approaches, e.g., one of the simplest is the Hartree-Fock approximation, where the antisymmetric many-electron wave function is written as a Slater determinant, which has to be solved selfconsistently. The approach which is by far the most widely used at the present time for the calculation of the total energy and other ground state properties of matter is the density functional theory (DFT). In DFT the ground state electron density of a system is considered to be the basic variable, rather than the wave function as in the general theory. The DFT results in the Kohn-Sham equations, which reduce the original many-body problem to an effective one-particle equation.

2.4 The density functional theory

The density functional theory is based on the Hohenberg-Kohn Theorem, which states that the total energy of a system of interacting electrons moving in an external potential $V_{\rm ext}(\mathbf{r})$ (potential caused by the nuclei) is a unique functional of the ground state electronic density $n_0(\mathbf{r})$ [22].

$$E_v[n] = \int n(\mathbf{r})V_{\rm ext}(\mathbf{r})d^3\mathbf{r} + \mathcal{F}[n]. \tag{2.8}$$

Furthermore, the minimum value of this universal functional $E_v[n]$ is the ground state electronic energy E_0, i.e.

$$E_0 = E_v[n_0] \leq E_v[n] \tag{2.9}$$

The Hohenberg-Kohn theorem declares the existence of the functional but not its form. Kohn and Sham postulated [23] that this functional could be written as:

$$E_v[n] = T_s[n] + \int n(\mathbf{r}) V_{\text{ext}}(\mathbf{r}) d^3\mathbf{r} + E_{\text{H}}[n] + E_{\text{XC}}[n], \tag{2.10}$$

where $T_s[n]$ is the functional of the kinetic energy of a system of N_e *non-interacting* electrons with density $n(\mathbf{r})$, $E_H[n]$ the Hartree energy and, $E_{\text{XC}}[n]$ the so-called exchange-correlation functional.

The Hartree energy is given by the electrostatic interaction between electrons

$$E_{\text{H}}[n] = \frac{1}{2}\int\int \frac{n(\mathbf{r}')n(\mathbf{r})}{|\mathbf{r}-\mathbf{r}'|} d^3\mathbf{r} d^3\mathbf{r}'. \tag{2.11}$$

Therefore, the energy functional is written as:

$$E_v[n] = T_s[n] + \int n(\mathbf{r}) V_{\text{ext}}(\mathbf{r}) d^3\mathbf{r} + \frac{1}{2}\int\int \frac{n(\mathbf{r}')n(\mathbf{r})}{|\mathbf{r}-\mathbf{r}'|} d^3\mathbf{r} d^3\mathbf{r}' + E_{\text{XC}}[n]. \tag{2.12}$$

With the electron density expressed in terms of a set of single particle wave functions $\psi_i(\mathbf{r})$ such that

$$n(\mathbf{r}) = \sum_i^{\text{N}_\text{e}} |\psi_i(\mathbf{r})|^2, \tag{2.13}$$

the kinetic energy of all N_e non-interacting electrons may be written as:

$$T_s[n(\mathbf{r})] = -\frac{1}{2}\sum_i^{\text{N}_\text{e}} \int \psi_i^*(\mathbf{r}) \nabla^2 \psi_i(\mathbf{r}) d^3\mathbf{r}, \tag{2.14}$$

Minimizing $E_v[n(\mathbf{r})]$ with respect to $n(\mathbf{r})$, under the constraint that the number of electrons be constant,

$$\int n(\mathbf{r}) d^3\mathbf{r} = \text{N}_\text{e}, \tag{2.15}$$

leads to:

$$\frac{\delta}{\delta n(\mathbf{r})}\left[E_v[n(\mathbf{r})] - \mu \int n(\mathbf{r}) d^3\mathbf{r}\right] = 0,$$

$$\Rightarrow \frac{\delta E_v[n(\mathbf{r})]}{\delta n(\mathbf{r})} = \mu, \tag{2.16}$$

where μ is the Lagrange multiplier arising from (2.15) and corresponding to the chemical potential of the electrons. Substituting Eq. (2.12) in (2.16) gives:

$$\frac{\delta T_s[n(\mathbf{r})]}{\delta n(\mathbf{r})} + V_{\text{ext}}(\mathbf{r}) + \int \frac{n(\mathbf{r}')}{|\mathbf{r}-\mathbf{r}'|} d^3\mathbf{r}' + \frac{\delta E_{\text{XC}}[n(\mathbf{r})]}{\delta n(\mathbf{r})} = \mu. \tag{2.17}$$

Equation (2.17) leads to the one-particle Schrödinger-like equations —the Kohn-Sham equations— for non-interacting electrons moving in an effective potential

$$\left(-\frac{1}{2}\nabla_i^2 + V_{\text{eff}}(\mathbf{r}) - \varepsilon_i\right)\psi_i(\mathbf{r}) = 0, \tag{2.18}$$

where

$$V_{\text{eff}}(\mathbf{r}) = V_{\text{ext}}(\mathbf{r}) + \int \frac{n(\mathbf{r}')}{|\mathbf{r}-\mathbf{r}'|} d^3\mathbf{r}' + \frac{\delta E_{\text{XC}}[n(\mathbf{r})]}{\delta n(\mathbf{r})}. \tag{2.19}$$

To find the ground state energy E_0 and the ground state density n_0 the Kohn-Sham equations (2.18) have to be solved self-consistently together with (2.13) and (2.19) due to the dependence of $V_{\text{eff}}(\mathbf{r})$ on $n(\mathbf{r})$. For a density computed from a set of trial wave functions, the potential V_{eff} is calculated, and inserted in (2.18). Then, from Eq. (2.13) a better set of wave functions $\psi_i(\mathbf{r})$ is obtained and a new density is computed. The procedure is repeated until no changes in the density occur.

2.4.1 The local density approximation

The ground state energy of an interacting system can be obtained provided the form of E_{XC} is known. At present numerical exchange-correlation potentials have only been determined for a few simple model systems, therefore an approximation must be used. The simplest approximation is the Local Density Approximation (LDA). In LDA, E_{XC} is defined as

$$E_{\text{XC}}^{\text{LDA}}[n(\mathbf{r})] = \int \varepsilon_{\text{XC}}(n(\mathbf{r}))n(\mathbf{r})d^3\mathbf{r}, \tag{2.20}$$

where $\varepsilon_{\text{XC}}(n(\mathbf{r}))$ is the exchange-correlation energy per unit volume of a homogeneous electron gas of density $n(\mathbf{r})$. Several parameterisations for $\varepsilon_{\text{XC}}(n(\mathbf{r}))$ exist, in this work it was used that of Perdew and Zunger [24]. This parameterisation is based on the quantum Monte Carlo calculations of Ceperley and Alder [25] on homogeneous electron gases at various densities.

LDA uses the exchange-correlation energy for the uniform electron gas at every point in the system regardless of the inhomogeneity of the real charge density. For

nonuniform charge densities the exchange-correlation energy can be expressed in terms of the gradient and higher spatial derivatives of the total charge density. This approximation is usually termed as Generalized Gradient Approximation (GGA). For systems where the charge density is slowly varying, the GGA has proved to be an improvement over LDA.

2.5 Pseudopotential total energy calculation

2.5.1 Periodic supercell with a plane wave basis

To describe the electron wave functions of the system studied it is necessary to choose a suitable set of simple basis functions in terms of which the electronic wave functions can be expanded. According to Bloch's theorem the wave functions in a periodic solid can be written as the product of a wave-like part and a cell-periodic function $f_{n,\mathbf{k}}(\mathbf{r})$.

$$\psi_{n,\mathbf{k}}(\mathbf{r}) = e^{i\mathbf{kr}} f_{n,\mathbf{k}}(\mathbf{r}). \tag{2.21}$$

The cell-periodic function can be described by a set of plane waves whose vectors are reciprocal lattice vectors:

$$f_{n,\mathbf{k}}(\mathbf{r}) = \sum_{\mathbf{G}} c_{n,\mathbf{k}}(\mathbf{G}) e^{i\mathbf{Gr}}. \tag{2.22}$$

In this way each electronic wave function can be expressed as a linear combination of plane waves,

$$\psi_{n,\mathbf{k}}(\mathbf{r}) = \sum_{\mathbf{G}} c_{n,\mathbf{k}}(\mathbf{G}) e^{i(\mathbf{k}+\mathbf{G})\mathbf{r}}. \tag{2.23}$$

The use of plane waves as a basis set may only be applied to a system exhibiting three dimensional translational symmetry. A surface, for example, cannot show periodicity in the direction perpendicular to the surface, so to be represented it would require a continuous plane wave basis set and therefore an infinite number of plane wave basis functions.

In order to reintroduce the required periodicity into the calculation, the surface will be contained within a supercell which will be then replicated periodically in vertical and lateral directions. This is illustrated schematically in Figure (2.1). The supercell will be formed by a slab and a region of vacuum, wide enough so that adjacent slabs do not interact significantly. Provided the supercell is sufficiently large so that the interactions between the surfaces are negligible, the energy per supercell will be identical to that of a single surface.

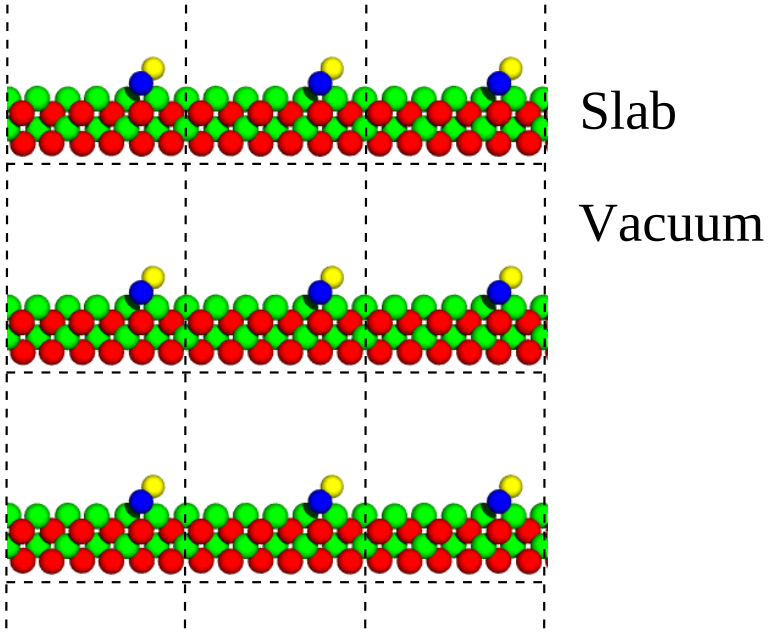

Figure 2.1: Schematic display of a supercell employed to represent a surface.

The plane wave basis set for the expansion of the wave functions and the Kohn-Sham operator can be written as:

$$< \mathbf{r}|\mathbf{k}+\mathbf{G} > \quad = \quad \frac{1}{\sqrt{\Omega}} e^{i(\mathbf{k}+\mathbf{G})\mathbf{r}}, \tag{2.24}$$

where **G** is a reciprocal lattice vector and Ω the volume of the supercell. **k** is a vector of the first Brillouin-Zone.

As for any basis set, the plane-wave basis must be truncated. This is accomplished by including all plane waves with kinetic energy less than or equal to a cutoff energy, $|\mathbf{k}+\mathbf{G}|^2 \leq E_{cut}$.

The electronic density for the single-particle state $\psi_{n,\mathbf{k}}(\mathbf{r})$ is now defined as

$$n(\mathbf{r}) \quad = \quad \frac{\Omega}{(2\pi^3)} \sum_n \int_{BZ} f_{n,\mathbf{k}}^{occ} |\psi_{n,\mathbf{k}}(\mathbf{r})|^2 d^3\mathbf{k}. \tag{2.25}$$

Hereby is $f_{n,\mathbf{k}}^{occ}$ the occupation number of the state $|\psi_{n,\mathbf{k}}>$ which is determined by the Fermi distribution.

The Brillouin zone integral (2.25) over the **k**-points is replaced by a sum over a number $N_{\mathbf{k}}$ of special **k**-points.

$$\frac{\Omega}{(2\pi^3)} \int_{BZ} d^3\mathbf{k} \rightarrow \sum_{\mathbf{k}} w_{\mathbf{k}}. \tag{2.26}$$

There are many methods for generating these special **k**-points. The one developed by Monkhorst and Pack [26] was used in the present work.

2.5.2 The pseudopotential approximation

According to their chemical behavior the electrons of an atom can be divided into two groups. While the core-electrons close to the nucleus are strongly localized and react weakly to the chemical environment, the valence-electrons occupy the external shells and are responsible for the chemical bonds in the solid. In a calculation without approximations the ground state of each electron has to be computed explicitly. The wavefunctions of the core-electrons and the rapidly oscillating wavefunctions of the valence-electrons in the core-region are difficult to fit with Gaussians or plane-waves and required an extremely large basis-set. Within the frozen-core approximation [27], the chemically inert core electrons are considered together with the nuclei as rigid ion cores. Based in this principle the pseudopotential approximation removes the core electrons and replaces the strong ionic potential by a weaker pseudopotential. In this way the pseudopotential will act on a set of pseudo wave functions rather than the true valence wave functions. Figure (2.2) displays the $4p$ all-electron wave function for selenium together with the $2p$ pseudo wave function. While the all-electron wave function oscillates in the region occupied by the core electrons, the pseudo wave function has no nodes, thus a set with a less number of plane waves will be required to represent it. It can be seen that beyond a chosen core cutoff radius r_c^l both wave functions coincide.

There are many schemes to construct a pseudopotential [28, 29, 30, 20]. In the present work norm-conserving pseudopotentials were constructed following the scheme of Troullier and Martins [20]. Norm-conserving pseudopotentials fulfil the following general properties [31]:

- The all-electron wave functions and the pseudo wave functions must be identical beyond a chosen core cutoff radius r_c^l, that can have a different value for each orbital with different angular momentum.
- The electronic density inside r_c^l is identical for the all-electron and the pseudoatom (norm-conserving property).

$$\int_0^{r_c^l} |R_l^{ps}(r)|^2 r^2 dr \quad = \quad \int_0^{r_c^l} |R_l^{ae}(r)|^2 r^2 dr, \tag{2.27}$$

  where R_l^{ps} and R_l^{ae} are the radial part of the pseudo- and all-electron wave functions, respectively.
- Pseudo-electron eigenvalues must be the same as the valence eigenvalues obtained from the atomic wave functions.

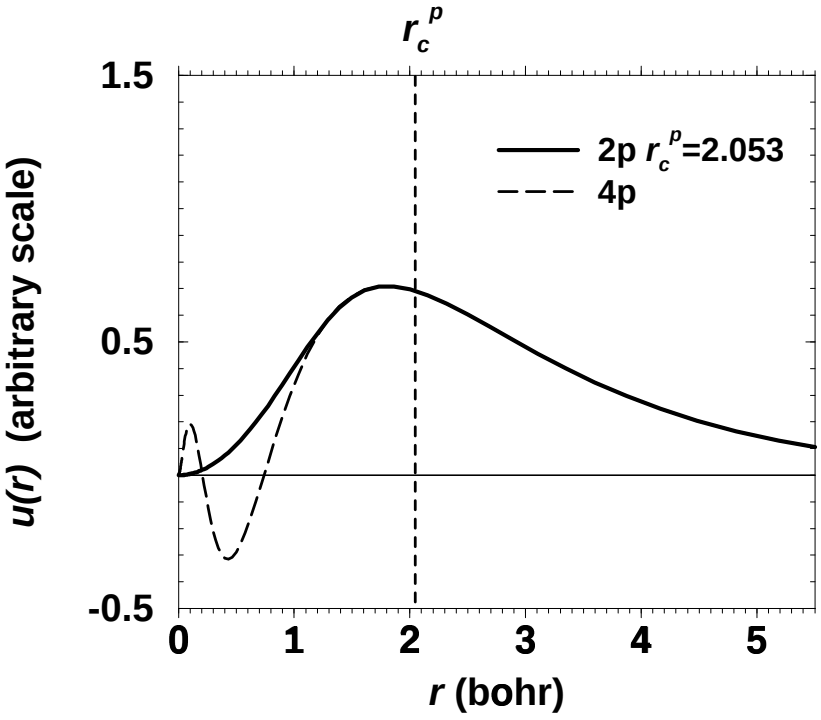

Figure 2.2: Selenium atom: $2p$ valence wave-function for the pseudo atom (solid line) and $4p$ all-electron atom (dashed). The legend gives the core cutoff radius r_c^l (in bohr).

$$\varepsilon_l^{\mathrm{ps}} \equiv \varepsilon_l \tag{2.28}$$

- The pseudopotential must be transferable, i.e. they have to reproduce the scattering properties of an ion in a variety of atomic environments.
- The pseudowave functions must be non-oscillatory and smooth.
- The pseudopotential must be a smooth function.
- The pseudopotential can be chosen non-local, that is, it can be different for each angular momentum component.

From the norm-conserving condition follows that a different pseudopotential $V_{\mathrm{pseu}}^l(\mathbf{r})$ is required for each valence state (s, p or d). Applying a projection operator on each component, the pseudopotentials can be combined in a general potential:

$$V_{\text{pseu}}(\mathbf{r}) \;=\; \sum_{l,m} V^{l}_{\text{pseu}}(\text{r})|lm><lm|. \tag{2.29}$$

All pseudopotential components $V^{l}_{\text{pseu}}(\mathbf{r})$ at large r are reduced to the ionic Coulomb potential, $-Z_{\text{va}}/r$, (where Z_{va} corresponds to the number of valence electrons) becoming l independent. Therefore, they can be expressed as the sum of an l-independent long-range term which is equal for all V^{l}_{pseu}, and an l-dependent short-ranged part.

$$V_{\text{pseu}}(\mathbf{r}) \;=\; V_{\text{local}}(\mathbf{r}) + \sum_{l,m} \Delta V^{l}_{\text{pseu}}(\text{r})|lm><lm|. \tag{2.30}$$

It is important to ensure the transferability of the pseudopotentials, that is, that they reproduce the scattering properties, excitation energies and chemical hardness properties [32, 33] of the corresponding all-electron atom in a wide range of environments. For this purpose, the logaritmic derivatives of the valence wave-functions, total energies and orbital eigenvalues for different valence configurations are evaluted and compared with those of the all-electron atom.

To reduce the computational costs Kleinman and Bylander [34] replaced the short-ranged semilocal term by a fully nonlocal operator.

$$\Delta V^{l}_{\text{pseu}} \rightarrow E^{\text{KB}}_{l}|\chi^{\text{KB}}_{l}><\chi^{\text{KB}}_{l}|, \tag{2.31}$$

with

$$\chi^{\text{KB}}_{l}(\text{r}) \;=\; \frac{\Delta V_{l}(\text{r})R^{\text{ps}}_{l}(\text{r})}{(<R^{\text{ps}}_{l}|(\Delta V_{l})^{2}|R^{\text{ps}}_{l}>)^{\frac{1}{2}}}, \tag{2.32}$$

and the Kleinman-Bylander energies E^{KB}_{l}

$$E^{\text{KB}}_{l} \;=\; \frac{<R^{\text{ps}}_{l}|\Delta V^{2}_{l}|R^{\text{ps}}_{l}>}{<R^{\text{ps}}_{l}|\Delta V_{l}|R^{\text{ps}}_{l}>} \tag{2.33}$$

The Kleinman-Bylander pseudopotentials show good transferability in general, but also under some conditions they can lead to ”ghost states”, i.e. unphysical bound states or resonances appearing in the valence spectrum. The energy levels of these states are below those of the physical valence states. By applying the analysis by Gonze *et al.* [35] these ”ghost states” can be found and eliminated, e.g. by choosing a different component of the semilocal pseudopotential as the local potential or adjusting the core cutoff radii r^{l}_{c}.

2.5.3 Calculation of the total energy

The total energy of a supercell results from the sum of all electronic and ionic contributions, whereby some terms are evaluated either in the real- or reciprocal space:

$$E[n] = T_s[n] + E_{\mathrm{H}}[n] + E_{\mathrm{ps,local}}[n] + E_{\mathrm{ps,nl}}[n] + E_{\mathrm{XC}}[n] + V_{\mathrm{ii}} \tag{2.34}$$

Until recently the solution of the Kohn-Sham equations (2.18) was based on techniques which required computationally expensive matrix diagonalization methods. Since the cost of matrix diagonalization increases with the third power of the total number of basis functions, the number of plane waves allowed in a calculation was limited. Consequently, the number of atoms per unit cell would be restricted to about 10.

In 1985 Car and Parrinello [36] introduced a new iterative method based on classical and statistical mechanics to solve Kohn-Sham equations without diagonalization. In this scheme the Kohn-Sham energy functional $E[\psi_i]$ is a functional of the Kohn-Sham single-electron wave functions $\{\psi_i\}$. The main idea is to consider $\{\psi_i\}$ as objects (with a given kinetic energy) that propagate through a space. Performing a molecular dynamics simulation the temperature of the system is gradually reduced until the wave functions eventually become stationary, thereby minimizing the Kohn-Sham functional.

Following [23] Car and Parrinello wrote the electron density in terms of occupied single-particle orthonormal orbitals $n(\mathbf{r}) = \sum_i |\psi_i(\mathbf{r})|^2$. The total energy can be minimized with respect to $\{\psi_i\}$ applying the variational principle

$$E_0[n] = \min_{\{\psi_i\}} E[\{\psi_i\}, \{\mathbf{R}_I\}], \tag{2.35}$$

where $\{R_I\}$ are the positions of the atoms in the unit cell. Since the wave functions are treated as dynamical variables, a Lagrangian is defined for the system:

$$\begin{aligned} L &= \frac{1}{2}\sum_i \mu \int d^3\mathbf{r} |\dot{\psi}_i(\mathbf{r},t)|^2 + \frac{1}{2}\sum_I M_I \dot{\mathbf{R}}_I(t)^2 - E[\{\psi_i(t)\}, \{\mathbf{R}_I(t)\}] \\ &+ \sum_{i,j} \Lambda_{ij} \left[\int d^3\mathbf{r} \psi_i^*(\mathbf{r},t)\psi_j(\mathbf{r},t) - \delta_{ij} \right], \end{aligned} \tag{2.36}$$

where μ is a fictitious mass associated with the electronic wave functions, M_I are the ionic masses, and E the Kohn-Sham energy functional which takes the place of the potential energy in the Lagrangian formulation. The wave functions are subject to the constraint of orthonormality

$$\int \psi_i^*(\mathbf{r})\,\psi_j(\mathbf{r}) d\mathbf{r} = \delta_{ij}, \tag{2.37}$$

which is required to ensure that the wave functions converge to different eigenstates. In the last term of Eq. (2.36) Λ_{ij} are the Lagrange multipliers that ensure this orthonormality condition.

Using the formulation of classical Lagrangian mechanics the resulting equations of motion are given by

$$\mu\ddot{\psi}_i(\mathbf{r},t) = -\mathbf{H}\psi_i(\mathbf{r},t) + \sum_j \Lambda_{ij}\psi_j(\mathbf{r},t) \tag{2.38}$$

$$M_I\ddot{\mathbf{R}}_I(t) = -\nabla_{\mathbf{R}I}E \tag{2.39}$$

where H is the Kohn-Sham Hamiltonian

$$\mathbf{H}\psi_i(\mathbf{r},t) = \int d^3\mathbf{r}' \frac{\delta E[n(\mathbf{r})]}{\delta n(\mathbf{r}')}\frac{\delta n(\mathbf{r}')}{\delta\psi_i^*(\mathbf{r})} = \frac{\delta E[n(\mathbf{r})]}{\delta\psi^*(\mathbf{r})}.$$

Equation (2.38) describes the fictitious classical electron dynamics, whereas Eq. (2.39) represents the ion dynamics. In Eq. (2.38) both terms $-\mathbf{H}\psi_i$ and $\Lambda_{ij}\psi_j$ can be considered as forces that influenced the propagation of the wave function. The simulated annealing method introduced by Kirkpatrick *et al.* [37] can be used as a general method for optimization problems. According to this method the system can be started at some high temperature and "cooled" gradually to zero temperature, to find the ground state of both electrons and ions simultaneously. At equilibrium $\ddot{\psi}_i = 0$, E is minimal, and Eq. (2.38) becomes transformable to the Kohn-Sham equation (2.18) with $\Lambda_{i,j}$ as the Kohn-Sham eigenvalues.

Car and Parrinello used the Verlet algorithmus [38] to iteratively improve the wave functions. For small Δt the second derivative of the wave function $\ddot{\psi}_i(\mathbf{r},t)$ (Eq. (2.38)) can be approximated by a second-order difference equation

$$\ddot{\psi}_i(t)\,\Delta t^2 = \psi_i(t+\Delta t) - 2\psi_i(t) + \psi_i(t-\Delta t), \tag{2.40}$$

where Δt is the length of the time step, $\psi_i(t)$, $\psi_i(t+\Delta t)$ and $\psi_i(t-\Delta t)$ are the values of the state at the present-, next- and last time step, respectively. Substitution of Eq. (2.38) into Eq. (2.40) gives

$$\psi_i(t+\Delta t) = 2\psi_i(t) - \psi_i(t-\Delta t) - \frac{\Delta t^2}{\mu}[\mathbf{H}-\lambda_i]\,\psi_i(t) \tag{2.41}$$

where λ_i are the eigenvalues of the Hamiltonian. After each time step a Grahm-Schmidt orthogonalization has to be performed to ensure full orthonormality of the wave functions [39].

The problem of solving the Kohn-Sham equations has been reduced to one of solving a set of classical equations of motion. Since the original paper by Car and Parrinello [36], a number of modifications [40, 41] have been presented that improved significantly the efficiency of the iterative solution of the Kohn-Sham equations. The modifications include the introduction of the conjugate gradients method [40, 41, 42] and a direct minimization of the total energy [41]. In the present work the algorithmus proposed by Williams and Soler [43] has been used to improve the wave functions.

2.5.4 Atomic forces

For the integration of the nuclei equations of motion it is necessary to calculate the forces acting on them. The forces acting on an atom with coordinates $\mathbf{R}_I$ result from the negative derivative of the ground state energy with respect to $\mathbf{R}_I$

$$\mathbf{F}_I = -\frac{dE}{d\mathbf{R}_I} \tag{2.42}$$

As the ion's position changes the electronic wave functions will also be altered, therefore the full derivative has to be expressed in terms of these changes,

$$\mathbf{F}_I = -\frac{\partial E}{\partial \mathbf{R}_I} - \sum_i \frac{\partial E}{\partial \psi_i}\frac{d\psi_i}{d\mathbf{R}_I} - \sum_i \frac{\partial E}{\partial \psi_i^*}\frac{d\psi_i^*}{d\mathbf{R}_I} \tag{2.43}$$

Hellmann and Feynman [44, 45] showed that when each electronic orbital is an eigenstate of the Hamiltonian, the sum of the two last terms of Eq. (2.43) is zero, and therefore the partial derivative of the total energy with respect to the ionic positions is the force felt by the ions. In practice, the wave functions are only calculated to a given accuracy, so they are not exact eigenstates of the Kohn-Sham Hamiltonian. Consequently, in a total energy calculation the wave functions have to be very close to self consistency before the ionic equations of motion can be integrated and a new calculation of the ionic coordinates takes place.

2.5.5 Structure optimization

As already mentioned (see Sec. 2.3) according to the Born-Oppenheimer approximation the electrons respond instantaneously to the slower motion of the ions, so the ions can be considered to move along a "potential energy surface" derived from a single electronic state. When studying diffusion processes it is essential to know the stable and metastable energy minima of this potential energy surface (also called Born-Oppenheimer surface). To this end the energy $E(\{\mathbf{R}_I\})$ has to be minimized with respect to the nuclei coordinates $\mathbf{R}_I$.

$$E_{\min} = \min_{\{\mathbf{R}_I\}} E(\{\mathbf{R}_I\}). \tag{2.44}$$

An efficient and numerically stable method to calculate the equilibrium geometry is damped Newton dynamics. From a starting configuration the atomic nuclei are moved according to Newton's equation of motion with an additional damping parameter. These equations of motion will be solved iteratively, so that the new positions $\mathbf{R}_I^{(n_{it}+1)}$ will be obtained from the two preceding positions $\mathbf{R}_I^{(n_{it})}$ and $\mathbf{R}_I^{(n_{it}-1)}$

$$\mathbf{R}_I^{(n_{it}+1)} = (1+\lambda_I)\,\mathbf{R}_I^{(n_{it})} - \lambda_I\,\mathbf{R}_I^{(n_{it}-1)} + \mu_I \mathbf{F}_I\left(\left\{\mathbf{R}_I^{(n_{it})}\right\}\right), \tag{2.45}$$

where λ_I and μ_I are the damping and reciprocal mass parameters, respectively. These parameters determine whether the nuclei loose their potential energy slowly or whether they move direct into the closest local minimum. In such a way, it is possible to overcome small barriers between adjacent minima and find the global minimum.

2.5.6 Computational procedure

All results in the present work have been obtained with the **fhi98md** program [46, 47], developed at the Theory Department of the Fritz-Haber-Institut. The major part of the results were carried out with a parallel version of the program on a CRAY T3E multiprocessor system using from 8 to 128 processing elements. A summary of the computational procedure is given below.

The first step of a total energy calculation is the generation of an initial wave function. This will be done by an explicit diagonalization of the Kohn-Sham Hamiltonian in a mixed-basis-set. The mixed basis-set is a subset of the plane-wave basis. It includes Bloch-states derived from atomic orbitals and plane waves up to an energy cut-off much lower than that of the full basis. This mixed basis-set provides a better initial wave function, which significantly improves the convergence of the calculations. Having obtained the initial wave function the program enters the selfconsistency loop. First, the electron density, and the contributions to energy, potentials and forces are calculated. The forces will be only computed when the electrons are sufficiently close to the Born-Oppenheimer surface. In the next step, the ions will be moved under the influence of the the calculated forces. The wave functions will be then updated using Williams-Soler algorithm and afterwards ortho-normalized with the Grahm-Schmidt scheme. This will be repeated until self-consistent criteria are achieved.

Chapter 3

Structural and electronic properties of $TiSe_2$ and $LiTiSe_2$ bulk

Many interesting physical properties which also yield applications in various technical fields are connected to the quasi two-dimensional behavior of the transition metal dichalcogenides such as Fermi surface nesting, charge density waves, and structural phase transitions. Special interest is focused on the performance of intercalation driven batteries [11, 12], which has motivated numerous experimental studies dealing with the evaporation of alkali metals on TMDCs surfaces in vacuum. The layered compounds TiS_2 and $TiSe_2$ have been intensively investigated for more than three decades because of their interesting electronic structure. While it is well known that $TiSe_2$ is a semimetal, for TiS_2 it is still debated whether it is a semiconductor or a semimetal [48, 49, 50].

In the present Chapter Density Functional Theory studies are performed to examine geometric and electronic properties of pure $TiSe_2$ as well as $LiTiSe_2$ bulk. The total energy value of Li intercalated in the octahedral sites is compared with the corresponding in the tetrahedral site, the first one being preferred by 0.3 eV. Electronic states, total energies, atom forces (used to obtain equilibrium geometries) are computed. The self-consistent valence charge density is analysed to obtain a bonding model consistent with the quasi-two dimensional nature of the electronic structure. In order to study the importance of interlayer coupling in bulk $TiSe_2$ additional studies are carried out on the electronic structure of separated single-layer slabs.

The performance of the pseudopotentials (Ti, Se and Li) used to describe the interaction between electrons and ions is verified.

3.1 Transition metal dichalcogenides

The layered TMDCs are protoype of crystals with two-dimensional structure. Their general formula is TX_2 where T stands for a transition metal of group IV (Ti, Zr or Hf), group V (V, Nb or Ta) or group VI (Cr, Mo or W) and X for a chalcogen (S, Se

or Te). The crystals have a layer or sandwich structure formed by a plane of transition metal atoms in a hexagonal pattern surrounded by two hexagonal chalcogen planes. The two chalcogen planes can be stacked directly above each other making trigonal prismatic holes for the metals, or can be staggered forming octahedral holes. The two types of coordinations observed for the transition metal atoms in the layered TMDCs are shown in Figure (3.1). The interactions between atoms in a layer are mainly covalent, whereas interactions between adjacent layers are weak and supposedly of van der Waals type. For this reason the space between the layers (interlayer space) is often called *van der Waals gap*. Due to the weak interlayer interactions the slabs exhibit a large relative freedom to stack, which results in various polymorphic types of the crystals. To label the different polymorphic types a number and a letter are used, with the first one determining the number of sandwiches required to define the unit cell in the *c* direction and the second the chalcogen arrangement (*T* trigonal, *H* hexagonal, or *R* rhomboedrical).

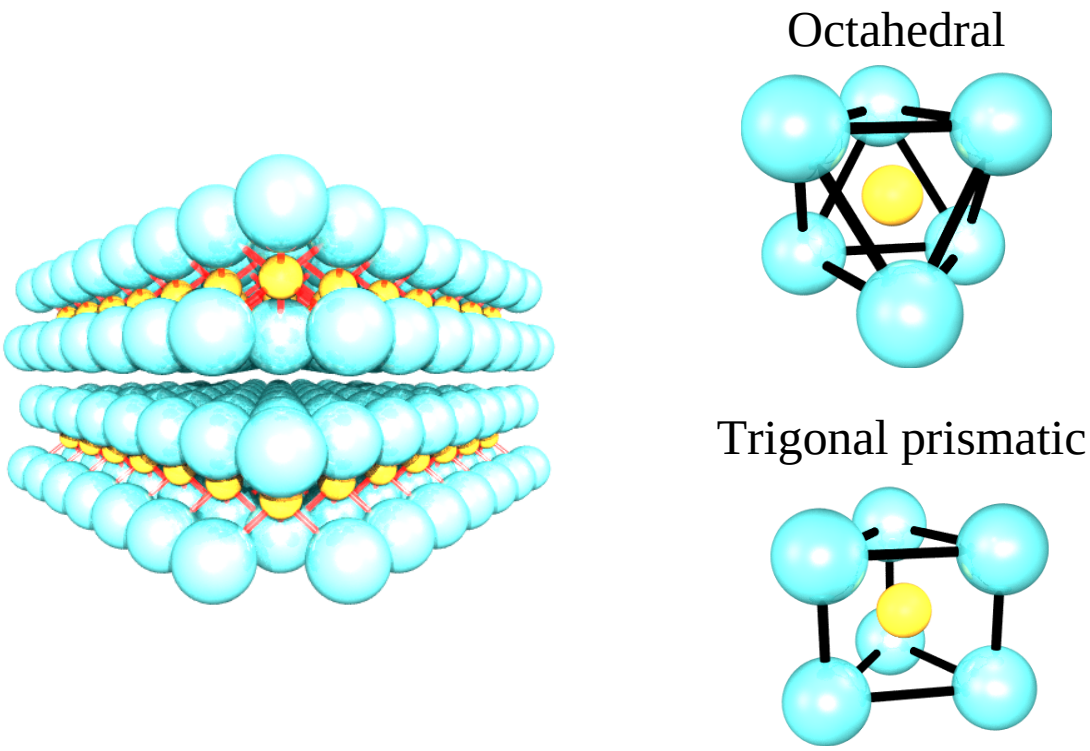

Figure 3.1: (left) Layered sandwich structure of the transition metal dichalcogenides crystals. (right) The two coordination types present in TMDCs layers.

The TMDCs of group IV crystallize in the octahedral 1*T* structure, while in the group V both octahedral and prismatic structures occur. The group VI compounds adopt the trigonal prismatic structure. Since the interactions between the layers are small, the stacking sequence of the sandwiches is not decisive for most properties of

these materials. However, the stacking of the atomic planes within a layer has an important influence on the electronic band structure.

Wilson and Joffe have [1] proposed a schematic energy band model for several groups of TX_2 compounds to explain their optical properties. The density of states as a function of energy is shown in Figure (3.2) for the different layered TMDCs' groups. According to this model the valence band states show mainly chalcogen *s* and *p* character, while the conduction band is derived from transition metal *d* states. The octahedral crystal field splits the *d* level in two bands showing t_{2g} (d_{z^2}, $d_{x^2-y^2}$, d_{xy}) and e_g (d_{xz}, d_{yz}) symmetry. For compounds with octahedral coordination the d_{z^2} orbital shows a small overlap with the higher *d* bands, while in the trigonal prismatic case this sub-band splits off from the remaining *d* bands and hybridizes with the chalcogen *p* bands. The degree of filling of the d_{z^2} orbital determines on a rough scale whether the TMDC is a metal, semimetal or semiconductor. As the transition metal transfers four electrons to the chalcogen atoms (filling the valence band), the metal remains in d^0 (IV), d^1 (V), or d^2 (VI) configuration. Thus, the group IV compounds should present semiconducting or insulating properties as the d_{z^2} orbital is unnocupied. The TMDCs with metals of group VI are also expected to be semiconductors, because the d_{z^2} orbital is completely filled. On the other hand, the group V compounds should show metallic properties due to the half-occupied conduction band.

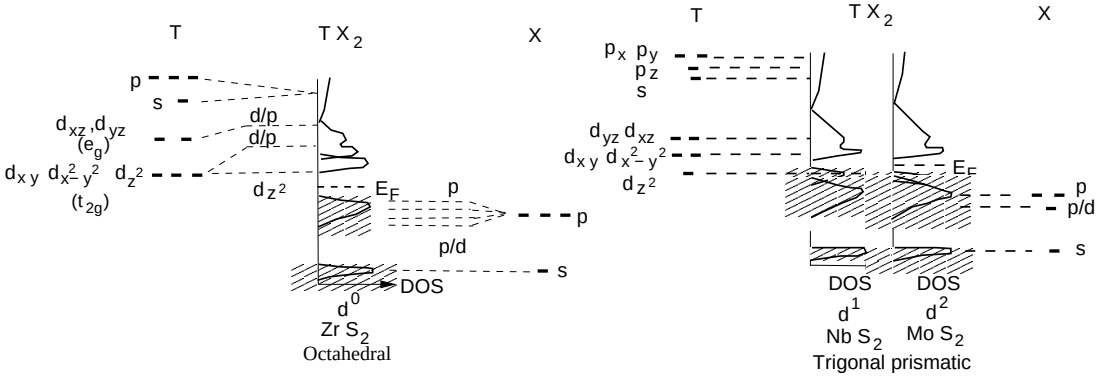

Figure 3.2: Schematic representation of the density of states of the layered Group IV, V, and VI transition metal dichalcogenide (Wilson and Yoffe model) after ref.[2]. The symmetries of the states and atomic orbitals are indicated on the left side of each graphic.

However, there are many exceptions to this general scheme like for example the semimetal $TiSe_2$, compound from the group IV which should be a semiconductor in the simple ionic picture. Also, among the TMDCs with metals of group V there occur structural distortions of the lattice, which give rise to the reduction of their metallic properties.

3.2 TMDCs intercalation compounds

One interesting property of the TMDCs is the possibility to form intercalation complexes by inserting foreign atoms or molecules in between their layers. A large number of articles are currently available in which the properties of TMDCs intercalation complexes are thoroughly discussed [12, 1, 51, 2, 52].

Two main effects of intercalation have been recognized: a) An increase in the interlayer separation necessary to accomodate the intercalants that are larger than the interstitial host sites and b) charge transfer from the intercalant to the host lattice. These effects are often analysed in terms of the rigid-band model. In this model it is assumed that the intercalate atom (which is usually electron-donator) transfers electrons from their outer orbitals to the host lattice. It is further assumed that the host valence band structure remains unchanged by the presence of the intercalate. Many of the observed changes are attributed to the filling of the lowest unoccupied conduction band of the host material. Although it has been demonstrated that this model is not always valid [53, 54], it may still be a useful approximation to understand qualitatively the changes induced by the intercalation.

The intercalated alkali metals can occupy two sites in the van der Waals gap, either in octahedral or trigonal prismatic coordination by the chalcogens. It depends on three factors: the amount of the intercalated alkali, the size of the alkali and the nature of the host material [55]. It has been observed that Li atoms occupy octahedral sites, Na occupy octahedral sites at low concentrations and at higher concentrations they move to trigonal prismatic sites, and for the larger alkali atoms K, Rb and Cs only the trigonal prismatic sites are preferred.

3.3 $TiSe_2$ bulk

3.3.1 Crystal Structure

The nature of the electronic state and the geometrical structure of $TiSe_2$ has become the subject of many experimental studies as well as theoretical calculations. Upon cooling below 200 K, $TiSe_2$ undergoes a structural and electronic phase transition described by a formation of a commensurate real space $2a \times 2b \times 2c$ superlattice with the resultant backfolding of bands in reciprocal space [56]. $TiSe_2$ belongs to the TMDCs of group IV with $1T - CdI_2$ structure, where the Se atoms are arranged in a near octahedral sixfold coordination around the Ti site within each sandwich. After Whittingham and Gamble [57] the lattice parameters of $TiSe_2$ are $a = 6.680$ a_B and $c = 11.345$ a_B (leading to a ratio of $c/a = 1.698$, compared to the ideal $1T$-octahedral value of $c/a = 1.633$). Figure (3.3) displays the unit cell and the first Brillouin zone of the 1T structure. The Bravais cell of the $1T - CdI_2$ structure is hexagonal with the

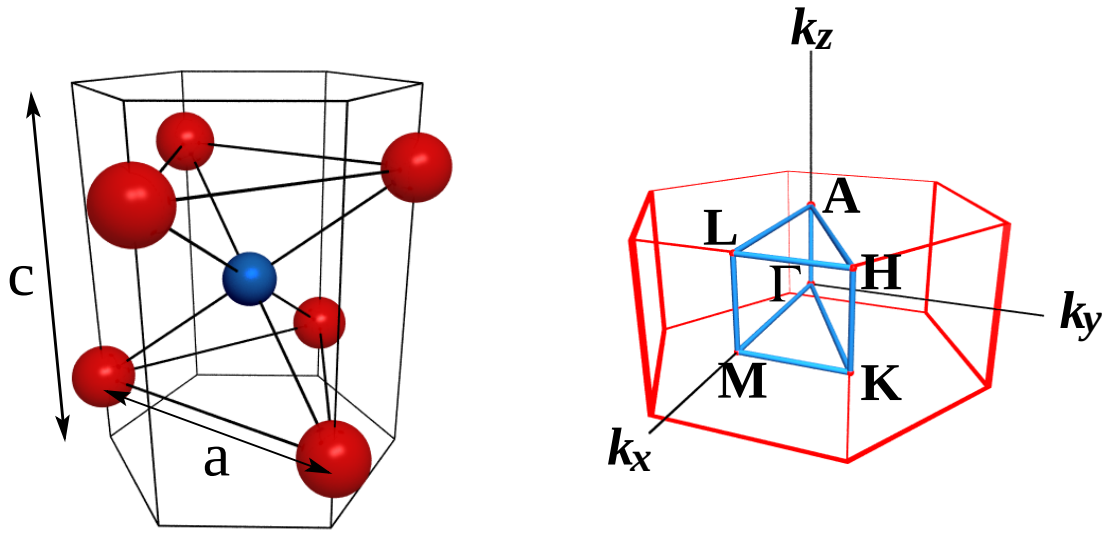

Figure 3.3: (left) Crystal structure of 1*T* $TiSe_2$ and (right) Brillouin zone of the hexagonal lattice with symmetry points labelled.

following primitive translational vectors:

$$\begin{aligned} \mathbf{a}_1 &= a(\frac{1}{2}, -\frac{\sqrt{3}}{2}, 0) \\ \mathbf{a}_2 &= a(\frac{1}{2}, \frac{\sqrt{3}}{2}, 0) \\ \mathbf{a}_3 &= c(0,0,1). \end{aligned} \tag{3.1}$$

The lattice basis consists of a titanium and two selenium atoms with coordinates given by: Ti (0, 0, 0), Se ($\frac{1}{2}a, \pm\frac{1}{2\sqrt{3}}a, \pm cz$), where the parameter $z = 0.2553$ [57] modulates the Ti - Se bond and determines the interlayer separation. Its ideal octahedral value of 0.25 is close to the observed value. The reciprocal lattice is also hexagonal:

$$\begin{aligned} \mathbf{b}_1 &= \frac{2\pi}{a}(1, -\frac{1}{\sqrt{3}}, 0) \\ \mathbf{b}_2 &= \frac{2\pi}{a}(1, \frac{1}{\sqrt{3}}, 0) \\ \mathbf{b}_3 &= \frac{2\pi}{c}(0,0,1), \end{aligned} \tag{3.2}$$

The space group of the 1T - CdI_2 structure is trigonal $P\bar{3}m1$ (D^3_{3d}) which is composed by the following symmetry operations:

$$(D^3_{3d}) = \{E, 2C_3, 3\sigma_d, i, 2iC_3, 3C_2\}.$$

In the coordinate system used E is the identity element of the group, C_3 is the rotation of 120° about an axis perpendicular to the layers (z-axis), i is the inversion operation, iC_3 is the corresponding rotation with inversion. C_2 is a rotation of 180° with respect a titanium-titanium axis in the xy-plane and σ_d is the mirror symmetry with respect to titanium-selenium axes that are perpendicular to the layers.

3.3.2 Electronic structure

In recent years a large number of different methods have been applied to calculate the band structure of TMDCs in general. Particularly, for $TiSe_2$ several bands models have

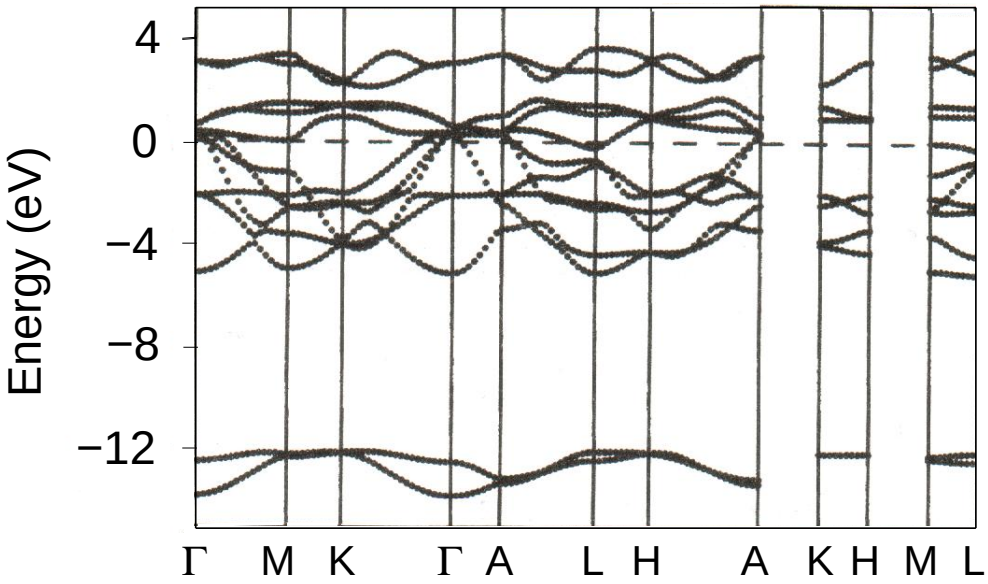

Figure 3.4: The band structure of $TiSe_2$ calculated by Fang *et al.* [48] using the localized spherical wave LSW method.

been published. These include the semi-empirical tight binding [58], the non-self consistent KKR [59] , the self-consistent tight binding [60], the symmetrised OPW [61], the LAPW [62], and more recently the LSW [48]. All models predict an almost equal ordering for the valence bands according to symmetry labels with occasional interchanges. Furthermore, the later self-consistent calculations [60, 62, 48] characterized $TiSe_2$ as a semimetal with a small indirect p/d band overlap ranging from 0.2-0.55 eV. This last result has been confirmed by means of angle-resolved photoemission measurements [8, 63, 64, 65], which reveal significantly dispersing and also cutting the Fermi energy bands (about 2 eV) along the layer perpendicular direction supported by p_z orbitals with admixtures of d_{z^2} (the z-axis is chosen along the c-direction). The bands related to layer parallel orbitals show almost no dispersion in this direction.

The *ab initio* band structure calculated by Fang *et al.* [48] is displayed in Figure (3.4). The two lowest bands are mainly composed of Se 4*s* states. The energy of these two bands is between -13.8 to -12.0 eV. Se $4p$ orbitals are situated between -5.2 and 0.6 eV above the Fermi level. The dispersion of two of the bands in the direction perpendicular to the layers Γ-A is quite large. These are bands of mainly Se $4p_z$ character. The overlap between the Se $4p_z$ orbitals within a slab, and across the van der Waals gap are quite large, leading to a total band width of about 5 eV. There is no net bonding across the van der Waals gap because both bonding and antibonding states are occupied. Above the Fermi level there are five Ti 3*d* bands, which split into a t_{2g}-like triplet and an e_g-like doublet of subbands. An overlap of about 0.8 eV can be observed at Γ and L.

3.3.3 $LiTiSe_2$

The lithium intercalation complexes of $TiSe_2$ (usually written as Li_xTiSe_2, where $0 \leq x \leq 1.0$) are of special interest as they may be used in the construction of high-energy-density batteries. In this material the basic structure of the original $TiSe_2$ lattice is retained on intercalation. As x increases from 0 to 1 the lithium atoms fill up the initially unocuppied octahedral sites of the original compound. With the gradual occupation of the octahedral holes the *a* and *c* lattice parameters increased in a continuous manner from $a = 6.680$ a_B and c = 11.345 a_B for $TiSe_2$ to a= 6.886 a_B and c=12.245361 a_B in $LiTiSe_2$ (with x=1) [57]. When compared with the unintercalated crystal the $LiTiSe_2$ unit cell contains one extra atom, however, it is bounded by the same lattice vectors. The symmetry properties of $LiTiSe_2$ are also summarized by the space group (D^3_{3d}). The Brillouin zone is hexagonal as shown in Figure (3.3). It was demonstrated by Jaegermann *et al.* [13] that lithium intercalates *in situ* under ultra-high vacuum conditions into $TiSe_2$. In Figure (3.5) the experimental valence band spectra of $TiSe_2$ and Li_xTiSe_2 (with $x \approx 0.3$) measured by Jaegermann *et al.* [13] together with the theoretical density of states distribution of TiS_2 and $LiTiS_2$ calculated by Umrigar *et al.* [49] show how the Fermi level is shifted by the occupation of the conduction band states. Additionaly, it can be seen that the intercalated Li ions shift the absolute position of the bands.

3.4 Computational details

The calculations employ density-functional theory together with the local-density approximation for the exchange-correlation functional [24, 25], as implemented in the FHI98md code [46]. Fully separable norm-conserving pseudopotentials constructed by following the scheme of Troullier and Martins are used to describe the interaction between electrons and ions [20]. These were generated using the code developed by Fuchs and Scheffler [66]. For computational efficiency the pseudopotentials are transformed into the separable Kleinman-Bylander form, with the *s*, *p* and *d* pseu-

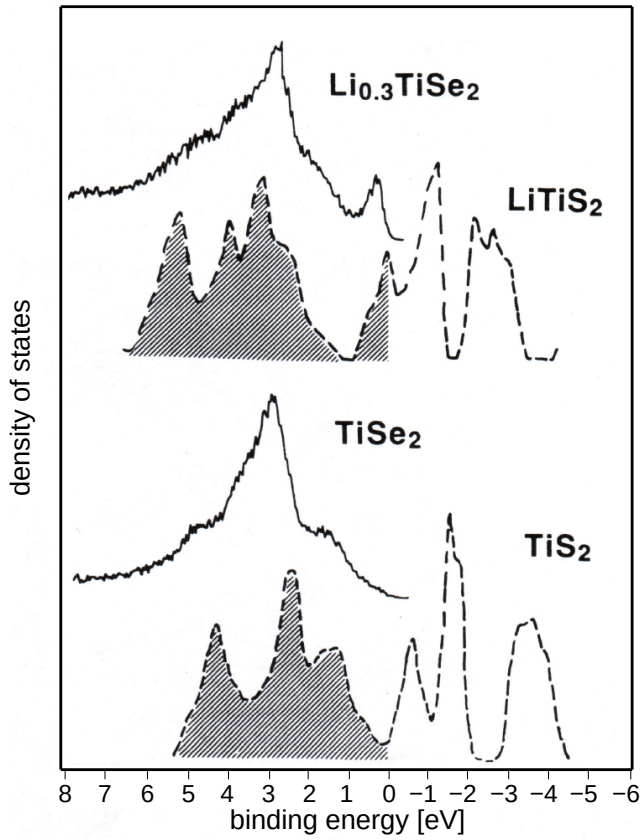

Figure 3.5: Theoretical density of states of TiS_2 and $LiTiS_2$ calculated by Umrigar *et al.* [49] and SXPS valence band spectra of $TiSe_2$ and $Li_{0.3}TiSe_2$ measured by Jaegermann *et al.* [13].

dopotential chosen as the local components for Ti, Se and Li, respectively to avoid the appearence of ghost states. To ensure better transferability of the alkali pseudopotential the nonlinear form of the core-valence exchange-correlation functional is taken into account [67]. These *ab initio* pseudopotential require as input only the atomic number and the starting electronic configuration.

Ti	Se	Li
	Electronic configuration	
$4s^2 4p^0 3d^2$	$4s^2 4p^4 4d^0$	$2s^1 2p^0 3d^0$
	Core radii in a.u.	
2.5, 2.9, 2.3	1.9, 2.1, 2.4	2.2, 2.2, 2.4

Table 3.1: Information about the starting atomic pseudopotentials.

In Table 3.1 are shown the different electronic configurations used to generate the pseudopotentials together with the core radii. The eigenfuctions of the Kohn-Sham operator were expanded in plane waves using a cutoff energy of 60 Ry. Tests were

performed for the electronic structure using a cutoff up to 100 Ry. They did not result in significant changes in the dispersion of the bands or the values of the gaps. The integration in reciprocal space was replaced by a sum of 63 Monkhorst-Pack special **k** points in the irreducible part of the Brillouin zone. In order to attain fast convergence of the Schrödinger equation it was found important to start with initial wave functions obtained from a mixed basis set of pseudo atomic orbitals and plane waves with a cutoff energy of 5 Ry. With these parameters, the total energy precision is better than 0.2 mRy/atom.

The detailed geometry of $TiSe_2$ and $LiTiSe_2$ bulk are obtained in the present calculations by minimizing the total energy of the systems with respect to the lattice constants *a* and *c*. The total energy is calculated for different values of lattice constants *a* and *c* chosen around the experimental values. In these calculations all atoms are allowed to relax without restrictions. The bulk system is considered to be at equilibrium if all force components are smaller than 0.5 mRy/bohr.

3.5 Results

3.5.1 Ti pseudopotential

The method of Troullier and Martins to generate pseudopotentials produces "soft core" pseudopotentials, which reduces considerably the number of plane waves needed to achieved convergence in the calculated properties.

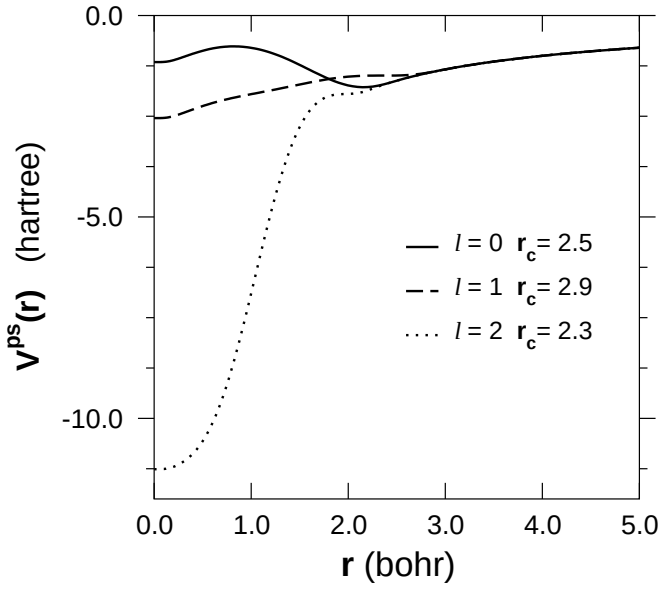

Figure 3.6: Norm-conserving ionic pseudopotentials for Ti ($4s^2 3d^2 4p^0$) using the method developed by Troullier and Martins [20]. The cutoff radius for each *l* component is given.

When separating the pseudopotential via the Kleinman-Bylander transform there is the possibility of generating "ghosts states". If at a reference energy the logarithmic

derivatives of the *s*, *p*, and *d* states obtained from the all-electron atomic potential, Troullier and Martins pseudopotential, and Kleinman-Bylander separable pseudopotential are identical, the existence of "ghosts states" can be excluded. For all the

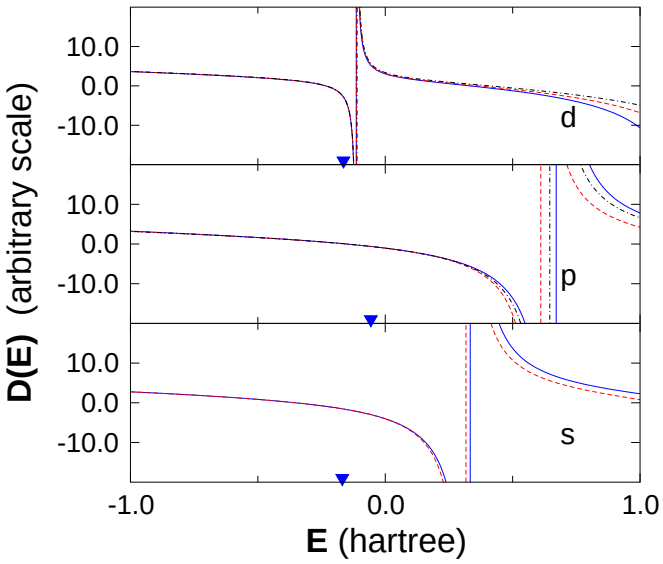

Figure 3.7: Logarithmic derivatives at $r = 3.33$ a_B for the *s* (bottom), *p* (middle), and *d* (top) states of a Ti atom. Solid curves: results of the all-electron calculations. Dashed curves: results using Troullier and Martins potentials. Dot-dashed curve: results using the TM-based Kleinman-Bylander separable potential. At the reference energies (triangle down) $E_s = -0.16$ hartrees, $E_p = -0.06$ hartrees, and $E_d = -0.16$ hartrees the three different potentials give the same result.

pseudopotentials generated in the present work, it has been verified that the choice of local components and core radii did not introduce any ghost states. Also, they have to show a good transferability over a wide energy range. The Ti pseudopotential, shown in Figure (3.6), was generated from the ground state configuration ($4s^2 3d^2 4p^0$) with radial cutoffs of 2.5, 2.9, and 2.3 a_B for the *s*, *p*, and *d* components, respectively, (see Table 3.1). The Ti 4*s* potential was chosen as the local component of the pseudopotential. The transferability of these pseudopotentials is illustrated in Figure (3.7), where the corresponding logarithmic derivatives of the radial component of the wave function are shown. The radial derivatives were generated at a radius of 3.33 a_B. As observed in this figure, there is a good transferability over a wide energy range as well as an absence of any ghost states. The results of the excitation energies test are shown in Figure (3.8). In this test the total energies from different occupational configurations were calculated for the pseudoatom and the all-electron atom (within the frozen-core approximation) and compared with those of the all-electron atom (with relaxed core). The configurations calculated covered excited states, where gradually 1/4 electron was transfered from the 4*s* to the 4*p* state. Also the first ionization potential was calculated. In Figure (3.8) the deviations from the pseudo atom and frozen-core calculations with respect to the all-electron results are shown. The errors due to the use of the pseudopotential should be compared to the errors that result from an all-electron calculation within the frozen-core approximation.

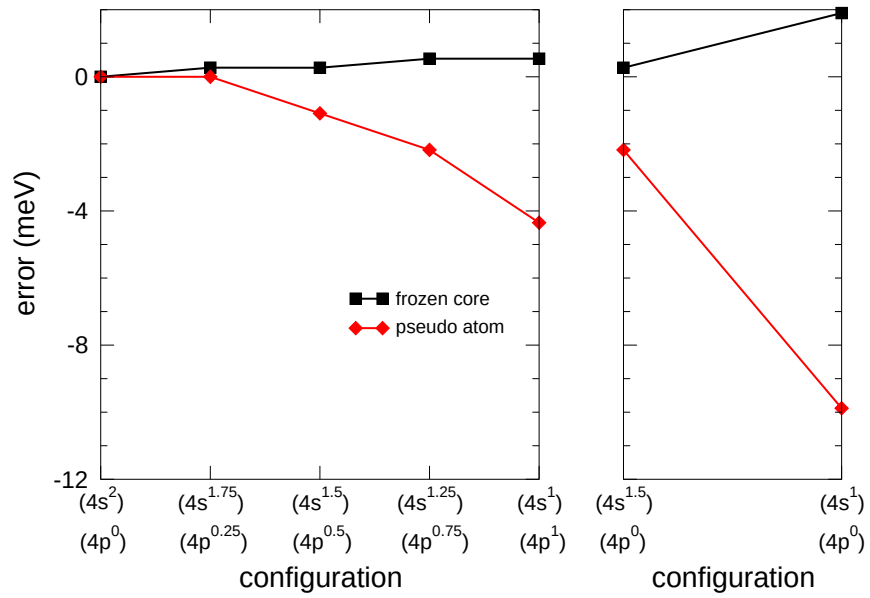

Figure 3.8: Transferability test of Ti pseudopotential: the deviations of (left) excitation energies and (right) first ionization potential of the pseudo atom and frozen-core calculations from the all-electron results with relaxed core for different atomic configurations. The reference configuration is $3d^2 4s^2 4p^0$.

To prove the reliability of Ti pseudopotential the band structure of Ti bulk in the hcp phase was calculated. The unit cell is composed of two Ti atoms at $(0,0,0)$ and $(\sqrt{3}a/2, 0, 1/2c)$, with $a = 5.575$ a$_B$ and $c = 8.850$ a$_B$ the experimental lattice constants [68]. In the present calculation the Brillouin-zone integration have been performed using a $(6 \times 6 \times 6)$ Monkhorst-Pack grid for the unit cell, which are 216 **k** points in the irreducible Brillouin-zone, and a cutoff of 100 Ry. The band structure obtained is presented in Figure (3.9) together with the calculated by Mattheiss [69] using the APW method. As it can be seen, the overall agreement of both band structures is quite satisfactory.

3.5.2 $TiSe_2$ and $LiTiSe_2$

The crystal structure parameters of $TiSe_2$ and $LiTiSe_2$ were optimized; the results are shown in Table 3.2. It can be noted that a reduction of about $2-4\%$ on both lattice constants for both compounds is achieved (with respect to the experimental values), due to the local-density approximation for exchange and correlation used in the calculations, which is generally known to yield lattice constants that are smaller by $2-6$ % with respect to experiment [70]. Li intercalated in $TiSe_2$ occupies the octahedral sites in the van der Waals gap. When placing the Li atom on the tetrahedral site, the total energy of the system increases by 0.3 eV. In $TiSe_2$ the value of z, 0.25,

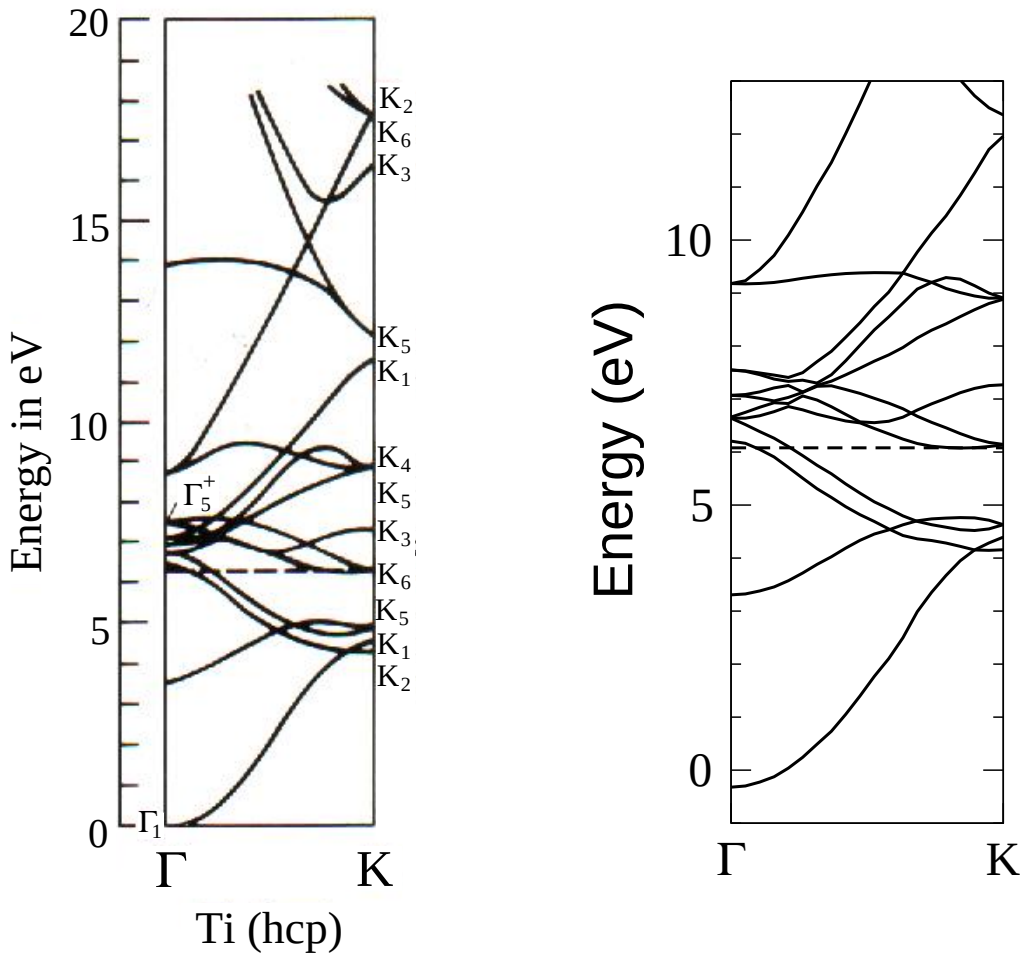

Figure 3.9: Band structure of Ti (hcp structure) obtained using the APW method (after Mattheiss) [69] (left), and with the Troullier and Martins Ti pseudopotential (right). The Fermi level in the (right) is indicated by the dashed line.

indicates that the intersandwich and intrasandwich separations between Se layers is equal. The Se-Ti bonds in $TiSe_2$ and $LiTiSe_2$ are 4.72 and 4.81 a_B, respectively. In $LiTiSe_2$ the distance in *c* direction between Se and Ti planes is 2.93 a_B and between Li and Se 3.02 a_B, while the Se-Li bond length is 4.86 a_B.

3.5.3 Band structure

$TiSe_2$ The band structure along the high-symmetry lines in the Brillouin zone and the density of states of $TiSe_2$ is presented in Figure (3.10). The zero of the energy is chosen to be at the Fermi level. The two lowest lying bands (between -14.4 to -12.5 eV) are mainly composed of Se 4s states. Between -5.7 eV and the Fermi level are

	$TiSe_2$			$LiTiSe_2$	
	a (a_B)	c (a_B)	z	a (a_B)	c (a_B)
LDA (present study)	6.41	10.89	0.25	6.61	11.90
Exp. [57]	6.68	11.34	0.2553	6.80	12.20

Table 3.2: Calculated in the present study and experimentally measured structure parameters of $TiSe_2$ and $LiTiSe_2$.

six bands of Se 4p origin, which are strongly dispersive throughout the Brillouin zone, two of them also along ΓA (perpendicular to the layers). The top of this set of bands is situated at Γ. At (and above) the Fermi energy five Ti 3d-derived conduction bands are found. They can be divided in two groups CB1 and CB2; CB1 with three bands in the range 0-2 eV and CB2 with two bands 2.2-3.8 eV above the Fermi level. In accordance with earlier calculations, $TiSe_2$ is found to be a semimetal with an overlap of 0.45 eV between the top of the Se 4p valence band at Γ and the bottom of the Ti 3d conduction band situated at L. Additionaly, there is an indirect Γ-M overlap of 0.22 eV. On comparing these results with those obtained by Fang *et al.* [48] (see Fig. (3.4)) it is found an agreement on the above mentioned features. However, in the present calculations, the indirect overlap is 0.35 eV smaller than from Fang *et al.* In Table 3.3 the present results are compared with those of previous calculations. The valence band width is in good agreement with both given results. The indirect gaps agree better with Benesh *et al.* [62]. In the lower panel of Figure (3.10), the density of states of $TiSe_2$ is shown. All the main peaks of the density of states are present in the x-ray photoemission spectrum by Jaegermann [13] .

$LiTiSe_2$ The band structure of $LiTiSe_2$ is shown in Figure (3.11). Several significant changes with respect to $TiSe_2$ can be seen. The Se 4s band width decreases by 0.38 eV, and moves down in energy by $\approx$ 0.18 eV. The valence band width decreases by 0.56 eV, moving down by 0.42 eV relative to the Ti 3d-t_{2g} bands. The Ti e_g bands move down by 0.69 eV while the Ti 3d-t_{2g} bands only by $\approx$ 0.23 eV. In Γ the separation between the valence and the conduction bands is increased by 0.80 eV. It can be also observed that the dispersion of bands along the ΓA direction is much less in the intercalate. This is due to the increase in the intersandwich spacing. The deviations from the rigid band model are: (i) the p/d gap increases by 0.8 eV; (ii) bands with Se 4 p_z character become less dispersive in the ΓA direction;

3.5.4 Valence electron density

Figure (3.12) shows the valence electron density of $TiSe_2$. The crystallographic plane shown in this figure is perpendicular to the *c*-axis. The plane crosses the Se atom

	$TiSe_2$			$LiTiSe_2$
	Present	LCAO [60]	LAPW [62]	
Valence band width	5.86	5.8	5.7	5.30
Γ direct gap	0.12	0.35	0.13	0.92
M direct gap	1.77	2.0	1.40	2.17
L direct gap	1.20	1.3	0.86	1.54
ΓM indirect gap	-0.22	0.15	-0.32	0.39
ΓL indirect gap	-0.45	-0.18	-0.55	0.12
Se 4s gap	6.88	-	-	7.04
Se 4s width	1.85	-	-	1.47
CB1 width	2.18	2.3	1.9	1.98
CB2 width	1.60	1.7	1.6	1.44

Table 3.3: Band structure characterists of $TiSe_2$ (compared with other calculations) and $LiTiSe_2$. All data in eV.

in the first atomic plane (indicated by a triangle up), thus the charge density has its maximum around this atom. Also the positions of the Ti- and Se-atoms (in the second and third atomic planes, respectively) can be clearly observed. The broken white line indicates the plane parallel to the *c*-axis in the $[\bar{2}110]$ direction, which is displayed in Figure (3.13) and (3.15). To study the effect of Li intercalation on the electron density also the charge density of $LiTiSe_2$ bulk was calculated. In Figure (3.13) the charge density of $TiSe_2$ and $LiTiSe_2$ structures are shown, where the layered nature of the both structures is clearly seen. Around the Ti atom in $TiSe_2$ the charge shows some angular polarization, in contrast to $LiTiSe_2$, where it is more spherical. In order to know the redistribution of the charge upon Li intercalation, the charge density averaged over the $x-y$ plane as a function of z is plotted in Figure (3.14) (for $TiSe_2$, $LiTiSe_2$ and their difference). In the abscissa's axis the atomic symbol of each element indicates its position on the *c*-axis. From the difference curve it is observed that the additional charge due to intercalation resides primarly between the Li and the Se planes. Also in the Ti plane an accumulation of charge density is obtained, which can be better identified in Figure (3.15), where a plot of the difference in the electron density before and after intercalation is shown.

To have a better picture of the effect of Li intercalation the charge density of both $TiSe_2$ and $LiTiSe_2$ structures are calculated exactly with the same lattice parameters, so that the electron densities can be substracted point by point in the real space. In Figure (3.15) this charge difference is shown in the same plane as in Figure (3.13), while in Figure (3.16) it is displayed in the plane formed by the vectors $[0001]$ and

$[\bar{1}010]$ (indicated by the solid black line in Fig. (3.13)). From these figures it can be seen that most of the guest electron is accepted by Ti and Se. In Figure (3.15) a well localized electron density at Ti ion site is observed, while in Figure (3.16) an accumulation of charge density around the Se atoms (in the first and in the third atomic planes) is well identified. The orbitals involved in this charge transfer can be clearly identified from the charge-difference plot. The electron clouds localized at the Ti sites have the shape of a d_{z^2} and d_{xy} orbitals. This is consistent with the filling of the bands. In $TiSe_2$ the electron coming from the interacalated Li ion fills the t_{2g} band which is comprised mainly of metal $d_{z^2}, d_{xy}, d_{x^2-y^2}$-type orbitals.

3.5.5 $TiSe_2$ single-layer slab

In order to examine the importance of electronic interlayer coupling in $TiSe_2$ bulk, calculations were carried out on the electronic structure of a $TiSe_2$ single-layer slab using a repeated slab geometry. The calculations were performed in a supercell geometry, where the layers are repeated along the (0001) direction with a larger interlayer distance c_{layer}. Test calculations with varying c_{layer} have shown that a value of $c_{\text{layer}} = 14\ a_B$ (corresponding to $1.28c$ with c denoting the respective bulk lattice constant) is sufficient to guarantee electronic separation between adjacent single-layer slabs. An increase of c_{layer} from 1.28 to $1.8c$ results in a difference of only 0.002 eV of the unit cell total energy.

In a first calculation the intralayer lattice parameter z of the single-layer was kept at the calculated value of the bulk. Then, it was optimized by allowing the relaxation of all atoms in the unit cell. Only a minor change in the z parameter was obtained (from 0.25 to 0.249), which implies that the atomic positions in a single layer are essentially identical to those of the single crystal.

In Figure (3.17) the electronic valence band structure of $TiSe_2$ single layer (with optimized positions) together with that of the bulk material (Fig. (3.10)) are shown for comparison. According to Figure (3.17) a single layer of $TiSe_2$ is a semimetal like the bulk material with the valence band maximum at the Γ point, in agreement with previous calculations [48]. The interactions perpendicular to the layers (Γ-A direction) are found to be small, which is indicated by the lack of dispersion for all bands along Γ-A. The conduction band minimum is found at the M and L points of the Brillouin zone, with an energy of -0.04 eV below the Fermi level. The overall appearance of the single layer band structure is very similar to the bulk band structure.

The electronic interlayer coupling in bulk $TiSe_2$ is found to be very weak. This is evident from a comparison of the overall shape of the band structure results of a $TiSe_2$ single-layer slab with that of the bulk. The present geometry optimization of the single-layer slab yields atom positions inside the elementary cell, which are very close to those of the bulk. The geometric and electronic similarity between layer and bulk justifies the use of $TiSe_2$ single-layer slabs as meaningful model for the $TiSe_2$ (0001) surface.

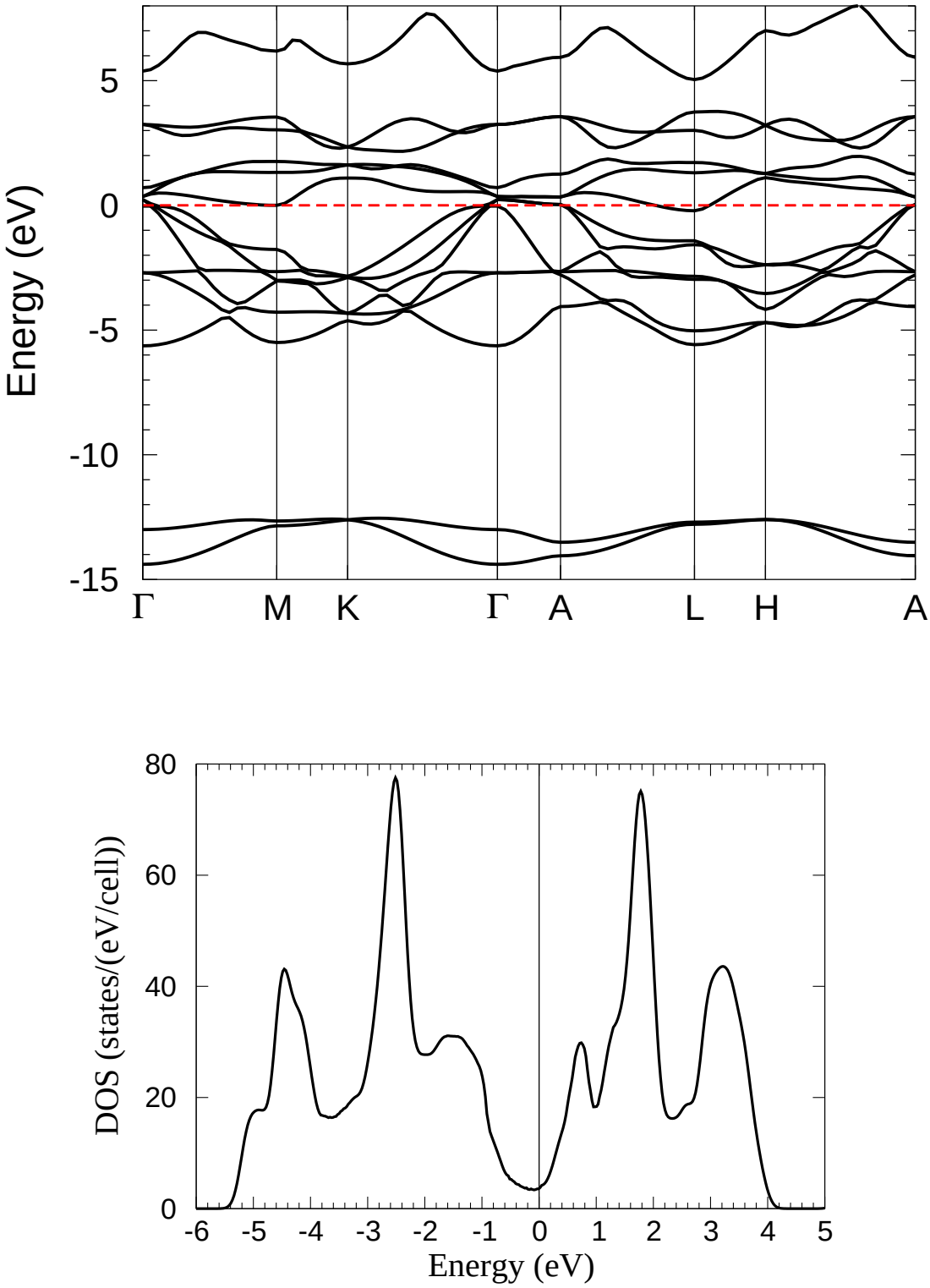

Figure 3.10: (upper) Band structure and (lower) density of states of $TiSe_2$ bulk. The energy bands are shown for characteristic paths connecting high-symmetry points of the irreducible part of the Brillouin zone. For a definition of the high-symmetry points see Fig. (3.3)

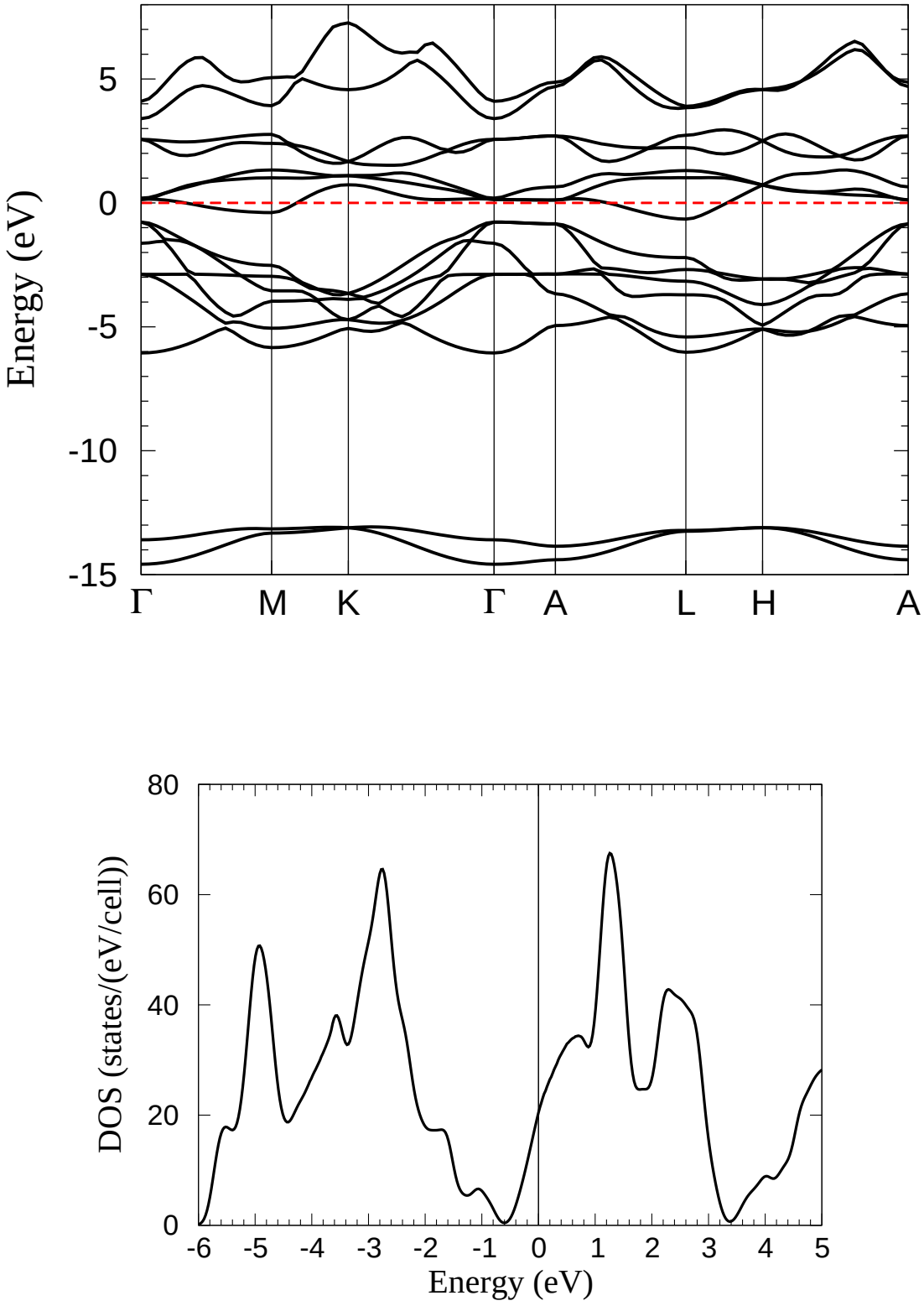

Figure 3.11: (upper) Self-consistent pseudo potential band structure and (lower) density of states of $LiTiSe_2$ bulk intercalated structure.

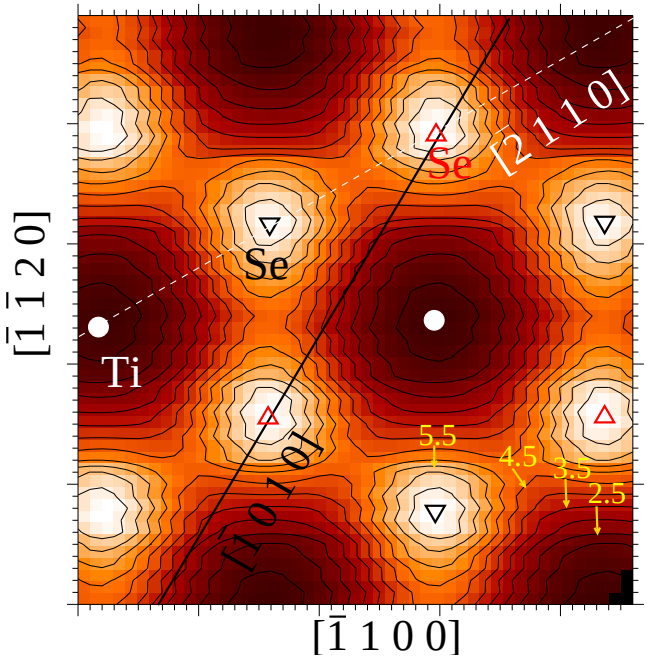

Figure 3.12: Valence electron charge density of $TiSe_2$ in the $x-y$ plane. The position of the Ti atom below the displayed plane is represented by a dot, that of Se as displayed (in the first atomic plane) by a triangle up and that of Se (in the third atomic plane) by a triangle down. The broken and solid lines indicate the cross sections used for Figures (3.13), (3.15), and (3.16), see text. Bright regions correspond to larger density. The units are 10^{-3} electrons/bohr^3 and the interval between adjacent contour lines is 0.5×10^{-3}/ bohr^3.

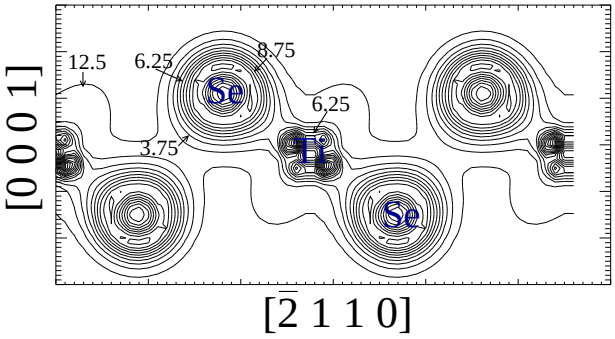

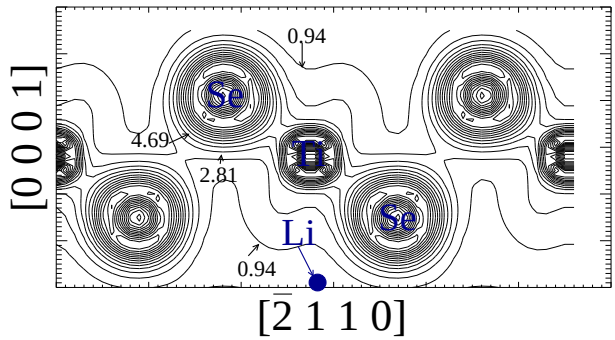

Figure 3.13: (upper) Valence electron charge density for bulk $TiSe_2$. Contour-line spacing is 1.25×10^{-2}. (lower) Valence electron charge density for bulk $LiTiSe_2$. Contour-line spacing is 9.35×10^{-3}. Units are given in 10^{-2} electrons/bohr^3.

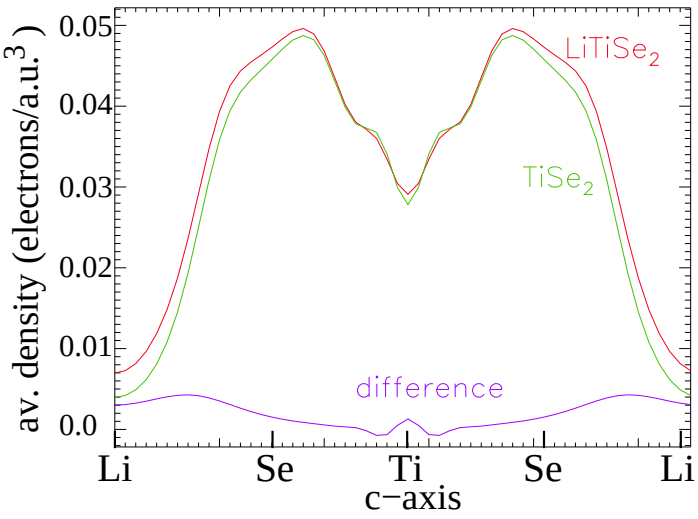

Figure 3.14: Averaged valence charge density of $LiTiSe_2$, $TiSe_2$ and their difference are plotted against z. The z coordinate of the atoms is indicated by the atomic symbols in the axis of abscissas.

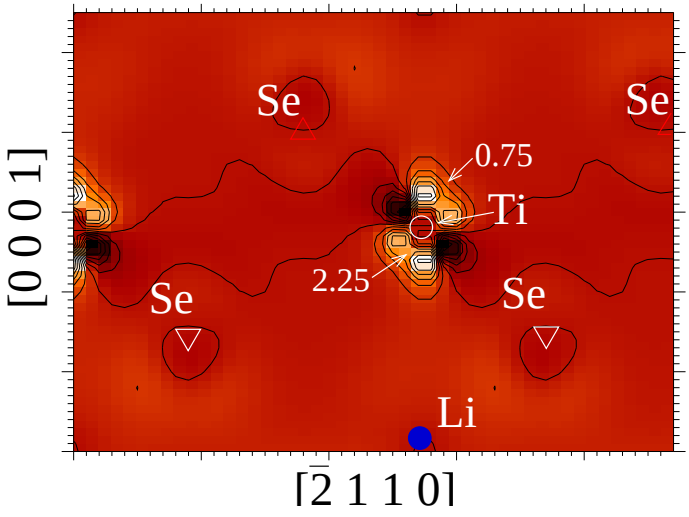

Figure 3.15: Charge density difference of $LiTiSe_2$ and $TiSe_2$ along a plane parallel to the c-axis. Bright regions correspond to larger density. The plane is indicated in Fig. (3.12) by the broken white line. Contour-line spacing is 0.75×10^{-2}, units are given in 10^{-2} electrons/bohr^3.

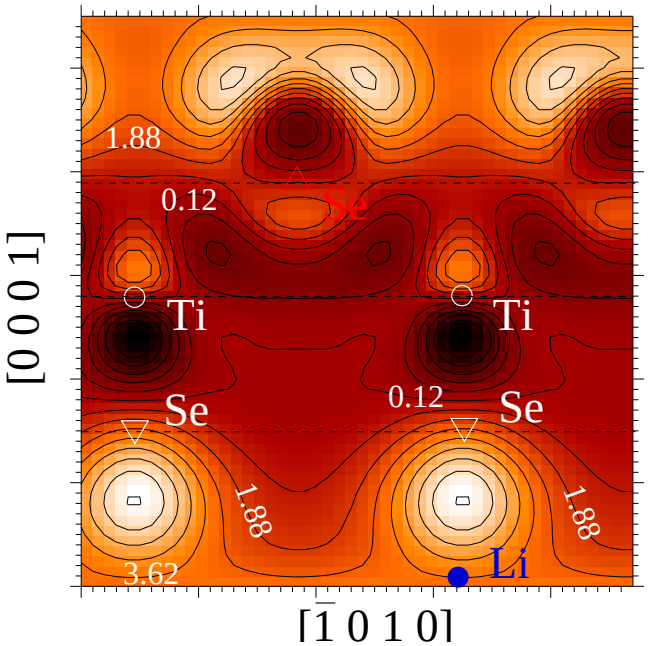

Figure 3.16: Charge density difference of $LiTiSe_2$ and $TiSe_2$ along a plane parallel to the c-axis. The plane is indicated in Fig. (3.12) by the solid black line. Bright regions correspond to larger density. Contour-line spacing is 0.87×10^{-3}, units are given in 10^{-3} electrons/bohr^3.

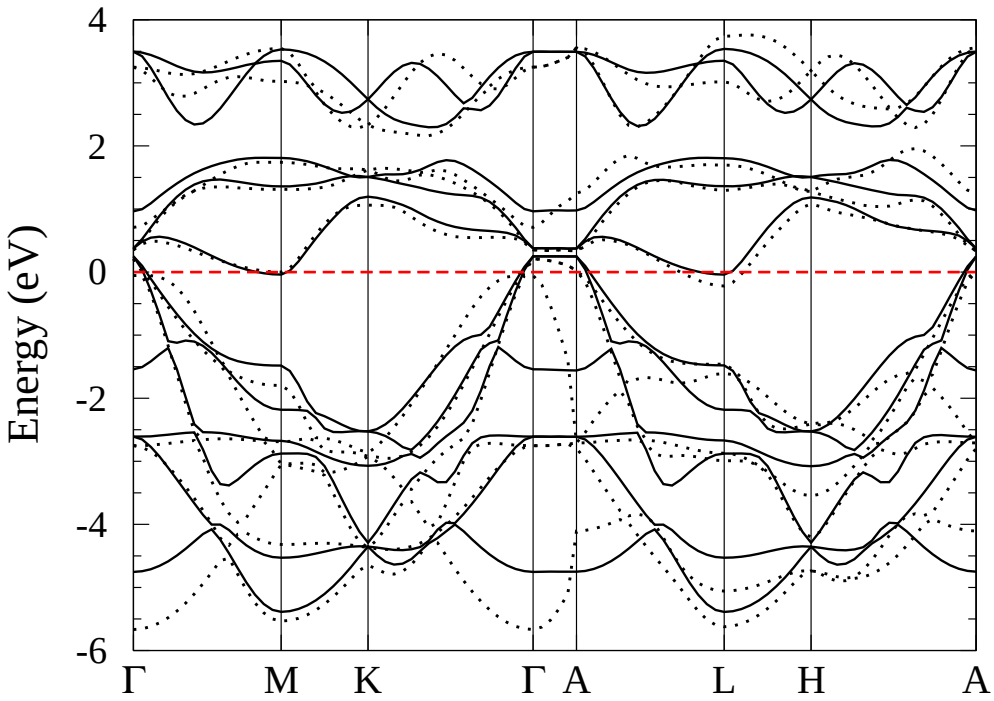

Figure 3.17: Comparison of calculated band structures of single layer- (solid lines) and bulk-$TiSe_2$ (dotted lines).

Chapter 4

Adsorption and Diffusion of Alkali metal on TMDCs (0001) Surface

The present study is accomplished to examine the structural and electronic properties of alkali metal atoms adsorbed at the $TiSe_2$ (0001) surface, as a first step to understand the intercalation process.

Alkali metal atoms deposited on transition metal dichalcogenides can be either adsorbed on top of the surface [71, 17] or intercalate into the van der Waals gaps of the substrate. In order to understand the interplay between adsorption and intercalation of alkali atoms at these layered crystals, I performed a detailed study of the migration and energetics of Li adatom on $TiSe_2$ (0001) surface and along the van der Waals gap.

To get insight into stable and metastable states, diffusion paths and diffusion barriers for the Li adatom, the adatom's potential energy surface (**PES**) is calculated, to find e.g. the hcp site energetically slightly preferred over the fcc site. To obtain information about the adsorbate-substrate bond, the change in the valence electron density, the orbital distribution, and the change of the work function as a function of the alkali coverage are studied. Surface diffusion is also investigated for Na, Rb and Cs adatoms.

4.1 Introduction

One of the most important features present on the TMDCs is their ability to form intercalation compounds with foreign atoms or molecules [2, 52]. Due to their layered structure and weak interlayer bonding the TMDCs represent suitable hosts for intercalation. Over the last decades the intercalation of alkali metals have been studied with interest due to their multiple technological applications, e.g., in solar cells [72], as electrode materials in rechargeable solid state batteries [11, 12], as solid lubricants [73, 74], in photovoltaic devices [75], among others. From the scientific point of view TMDCs represent an ideal substrate for surface science studies owing to their chemically inert surfaces. It has been shown that when alkali metals are deposited on TMDCs surfaces under ultra-high vacuum conditions, they can intercalate into the bulk mate-

rial or be adsorbed on the surface of the substrate forming clusters, as observed for Cs on MoS_2 [76] and on WSe_2 [77], or networks of metallic nanowires, like Rb on $TiTe_2$ [18].

In spite of the thorough investigation done on *in situ* intercalation during the recent last years, the details to fully understand the mechanism behind it are still unknown up to now. Different aspects are still far from being completly comprehended like for example, the path the alkali atoms follow to reach the van der Waals gap, and the energy barriers they have to overcome to intercalate.

Moreover, the design of new battery materials requires a microscopic understanding of the stable sites and diffusion pathways of the alkali ions, as well as the charge redistribution after intercalation, which is very difficult to obtain from experiment.

Data for energy barriers towards diffusion and intercalation at an ideal surface will be valuable to optimize the growth by van-der-Waals epitaxy. The latter has become an important tool for the preparation of interfaces and heterojunctions. [78]

As a prototype for which vacuum intercalation seems to be experimentally well established mainly the system Li with $TiSe_2$ [13] has been explored with *ab initio* calculations to yield:

- How does the TMDCs (0001) surface change with the presence of alkali atoms?
- What are the adsorption positions on the surface?
- How does Li diffuse on the surface and what are the energy barriers?
- How does the diffusion of Li within the van der Waals gap differ from the surface diffusion?
- How is the redistribution of the charge density during the adatom diffusion?
- How does the adsorption energy change with the alkali coverage?
- How does the dipol moment change and therefore the work function as a function of the alkali coverage when Li atoms are adsorbed on the surface or intercalated in the van der Waals gap?

4.2 Calculational Method

The technical details of the density fuctional theory calculations are given in Chapter 2. The clean $TiSe_2$ (0001) surface is modeled by a supercell with a slab consisting of three sandwiches of $TiSe_2$ (9 atomic planes), separated by a 8.3 Å vacuum region, see Figure (4.1).

The adatom plus surface is modeled by taking a periodic arrangement of adatoms on the surface and choosing the resulting surface supercell to be so large that the interaction between adatoms in neighboring cells is negligible. For calculating the adsorption sites and diffusion barriers of alkali adatoms a $(\sqrt{3} \times \sqrt{3})R30^\circ$ $TiSe_2$ (0001)

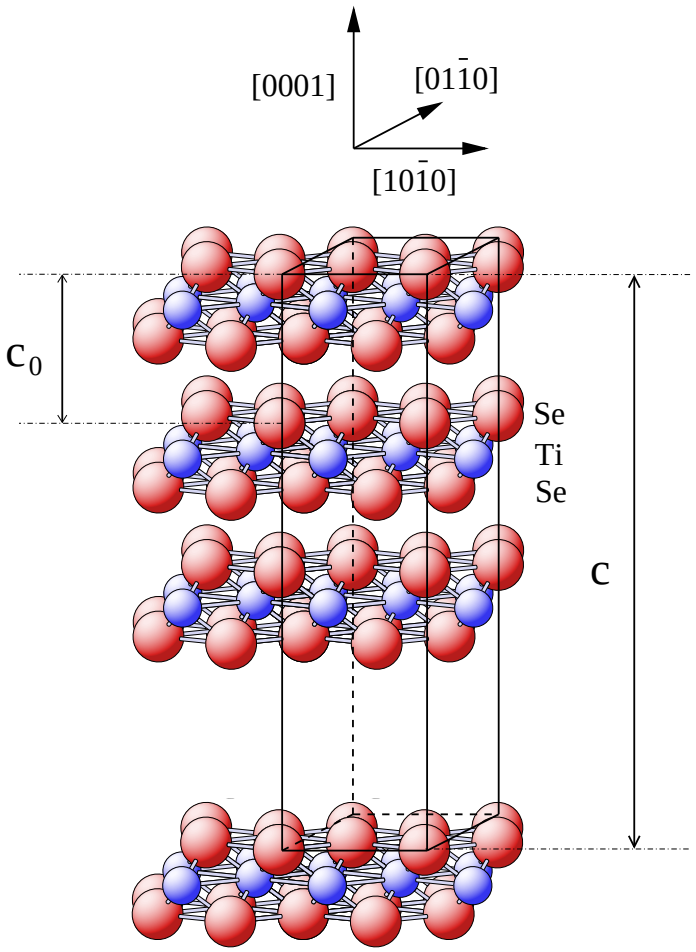

Figure 4.1: Schematic display of the $(\sqrt{3} \times \sqrt{3})R30^{\circ}$ supercell employed to represent the $TiSe_2$ (0001) surface, with c_0 the separation between layers (theoretical lattice constant for $TiSe_2$ bulk fully intercalated with Li), and c, the supercell lattice constant in z-direction.

surface supercell is used. To prevent from artificial adsorbate-adsorbate interactions through the slab, the alkali metal adatom is adsorbed on one side only, where the induced dipole moment is taken into account by applying a dipole correction [80].

When studying the system Rb-$TiSe_2$, the vacuum region was increased from 7.0 Å to 10.3 Å to estimate the interaction of the adatom with the opposite surface. It was obtained a change in the energy differences of about 0.02 eV. The plots of the charge density difference of Rb-$TiSe_2$ with different vacuum region, show that the interaction of the adatom with the opposite surface is similar and negligible in both cases, see Figure (4.2). The electron eigenfunctions are expanded in a plane-wave basis using a cutoff of 40 Ry with three special **k** points in the surface Brillouin zone [81]. Con-

vergence tests performed for a higher number of **k** points did not show any significant variation of the calculated energies. Calculations with 4 layers of $TiSe_2$ and a cut-off of 60 Ry show that the adsorption energy *differences* are accurately given, which means that they change by less than 0.03 eV. In order to improve the quality of the integration in **k** space a Fermi-surface smearing of 0.1 eV is used and the resulting total energies are extrapolated to zero temperature.

The atomic positions of all atoms are allowed to relax, except for the $TiSe_2$ atoms in the bottom sandwich, which are fixed at their relative bulk positions. The total energy surface $E(x,y)$ of the alkali adatom is determined for its diffusion. It is calculated by mapping out the total energy as a function of the adatom position (x,y). At each position the z coordinate of the adatom and the full relaxation of the substrate atoms is calculated by energy minimization. The minimum total energy defines the binding

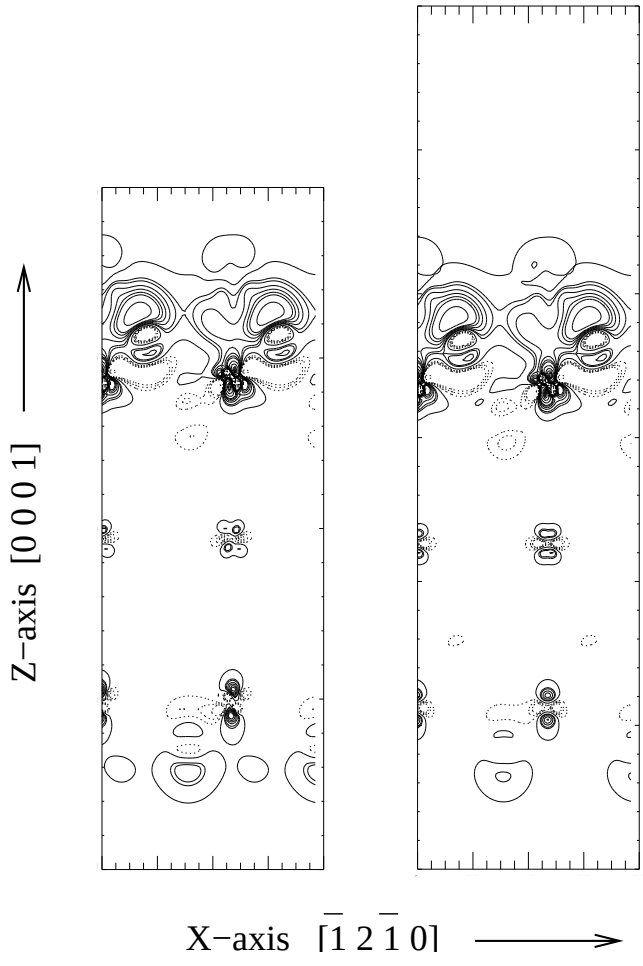

Figure 4.2: Charge density difference of Rb adsorbed on $TiSe_2$ with (left) 7.0 Å and (right) 10.3 Å of vacuum space.

geometry of the adatom and the substrate. The saddle point on this energy surface determines the activation barrier for diffusion along the surface. Since the energy surface $E(x,y)$ must have the same symmetry as the crystal surface, it is only needed to carry out calculations for positions of the adatom in the irreducible part of the supercell. Therefore, the energy surface is only mapped on a (1x1) surface unit cell with a mesh width of one sixth of the unit vectors. This approximation is only used to reduce the number of independent grid points (x,y). The geometry of the adatom and surface is not constrained in any way.

Calculations are performed for lithium on the surface and van der Waals adsorption sites for coverages ranging from $1/16$ to a full monolayer (ML). In particular, coverages of 0.06, 0.11, 0.33, 0.25 ML were calculated using a (4×4), (3×3), $(\sqrt{3}\times\sqrt{3})R30^\circ$, and (2×2) surface unit cells, respectively. Coverages $\Theta_{\mathrm{Li}}=0.5$ and 1 ML were calculated in the (2×2) surface unit cell containing two and four lithium atoms, respectively. The coverage $\Theta=1$ is defined as the ratio of the number of adsorbate atoms to the total number of hcp sites in the substrate.

The total energies of isolated, free atomic Li, Na, Cs, and Rb are calculated in a cubic cell of side lenght 25 a_B with the **k** point (0.5 0.5 0.5) for the Brillouin Zone sampling. The spin polarization effects were not included.

It is useful to define the *adsorption energy per adatom* for the analysis discussed below. The adsorption energy per adatom is defined as the difference of the total energy of the adsorbate system and the total energy of the clean, unreconstructed substrate together with a free, neutral adatom. Using the indices which refer to the adsorption of Li on $TiSe_2$ (0001), the definition of the adsorption energy per adatom is given by

$$E_{\mathrm{ad}}^{\mathrm{Li/TiSe_2\,(0001)}}=\frac{1}{N_{Li}}[E^{\mathrm{Li/TiSe_2\,(0001)}}-(E^{\mathrm{TiSe_2\,(0001)}}+N_{Li}E^{\mathrm{Li\,atom}})], \qquad (4.1)$$

where N_{Li} is the number of Li atoms in the surface unit cell, and the total energy of the adsorbate-substrate system, the clean $TiSe_2\,(0001)$ substrate, and the free Li atom, are represented by $E^{\mathrm{Li/TiSe_2\,(0001)}}$, $E^{\mathrm{TiSe_2\,(0001)}}$, and $E^{\mathrm{Li\,atom}}$, respectively. The binding energy is the energy that a free Li atom gains by its adsorption at the surface. For the on-surface adsorption the *binding* and *adsorption* energies are the same.

To analyze the nature of bonding, it is helpful to consider the *difference electron density* $n^{\Delta}(\mathbf{r})$,

$$n^{\Delta}(\mathbf{r})=n(\mathbf{r})-n^{0}(\mathbf{r})-n^{Li}(\mathbf{r}), \qquad (4.2)$$

where $n(\mathbf{r})$ is the total valence electron density of the substrate-adsorbate system, and $n^{0}(\mathbf{r})$ and $n^{Li}(\mathbf{r})$ are the electron densities of the clean substrate and the free lithium atom, respectively, and the atomic geometry of the substrate is chosen to be that of the relaxed adsorbate system. The *difference electron density* shows the depletion or accumulation of the charge density in the system due to the adatom adsorption on the surface.

4.3 $TiSe_2$ (0001) surface

One aim of this study is to establish the energetic and geometric differences between adsorption of alkali metal atoms on the $TiSe_2$ (0001) surface and intercalation in the van der Waals gap. In order to achieve this, total energy calculations have been carried out for both cases. The supercell used to model the surface must have the same lattice constants for both configurations to make the results comparable. I chose to use the theoretical lattice constants of bulk $TiSe_2$ fully intercalated. The theoretical lattice constants I obtained for bulk $TiSe_2$ fully intercalated with Li, are $a_0 = 6.61$, $c_0 = 11.90$ a_B, (see Table 3.2). The experimental values for bulk $TiSe_2$ fully intercalated with Li are $a_0 = 6.8$ and $c_0 = 12.20$ a_B [57]. The decreased theoretical values are partially due to the local-density approximation for exchange and correlation used in the calculations, which is generally known to yield lattice constants that are smaller by $2-6$ % with respect to experiment [70]. To introduce no stress the theoretical values are used to model the (0001) $TiSe_2$ surface, see Figure (4.1). In order to determine the effects of alkali adsorption on the $TiSe_2$ (0001) surface structure, I first investigated the bare surface.

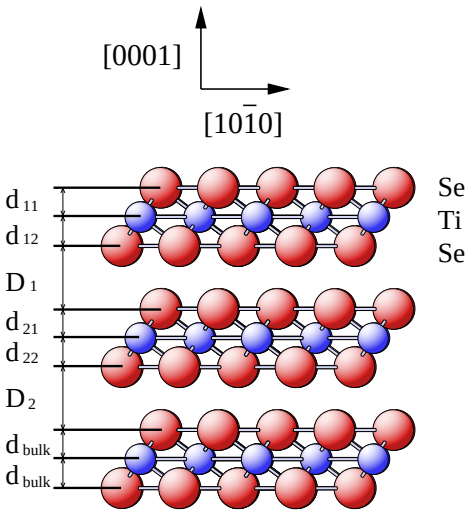

Figure 4.3: Side view of the $(\sqrt{3}\times\sqrt{3})$ unit cell used to represent the $TiSe_2$ (0001) surface. The first two layers are allowed to relax and the one in the bottom is fixed at its relative bulk position. For the distance values, d_i and D_i, between atomic planes, see Table 4.1.

I performed calculations for the atomic relaxation of the clean surface using (4×4), (3×3), $(\sqrt{3}\times\sqrt{3})$, and (2×2) periodicities. These calculations provide a test of the surface relaxation with cell size. The atomic geometry of $(\sqrt{3}\times\sqrt{3})$ $TiSe_2$ (0001) surface is displayed in Figure (4.3). The results of the structural parameter obtained

are summarized on Table 4.1. The distances between the atomic planes from the first and second $TiSe_2$ sandwiches, and their differences with respect to the bulk values are listed in the upper and middle blocks, respectively. In the bottom block the shift of each atomic plane with respect to the bulk positions is given as well.

In all the supercells, except in the (4×4), the first and second sandwich's spacings contracted by 4-5% and 3-4% with respect to the bulk value d_{bulk}, respectively. Therefore, the van der Waals gap width is increased by 3-4%. For the (4×4) supercell, on the contrary, an expansion from both sandwiches of 2% and a decrease of the van der Waals gap width of 3% are obtained.

These results are understandable since the calculations were carried out using the lattice constants of bulk $TiSe_2$ fully intercalated with Li, from which the one in the z direction is 8% larger than in the pure compound.

	$TiSe_2$ (clean)						
supercell	d_{11}	d_{12}	D_1	d_{21}	d_{22}	D_2	d_{bulk}
(4×4)	3.03	3.03	5.76	3.03	3.03	5.89	2.97
(3×3)	2.85	2.85	6.13	2.87	2.87	6.05	2.97
(2×2)	2.86	2.84	6.17	2.85	2.87	6.05	2.97
$(\sqrt{3}\times\sqrt{3})$	2.82	2.83	6.20	2.83	2.83	6.09	2.97
	Δd_{11}	Δd_{12}	ΔD_1	Δd_{21}	Δd_{22}	ΔD_2	Δd_{bulk}
(4×4)	0.06	0.06	-0.19	0.06	0.06	-0.06	0.0
(3×3)	-0.12	-0.12	0.18	-0.10	-0.10	0.10	0.0
(2×2)	-0.11	-0.13	0.22	-0.12	-0.10	0.10	0.0
$(\sqrt{3}\times\sqrt{3})$	-0.15	-0.14	0.25	-0.14	-0.14	0.14	0.0
	relaxation Δz of atomic plane with respect to bulk						
	1rst (Se)	2nd (Ti)	3rd (Se)	4th (Se)	5th (Ti)	6th (Se)	
(4×4)	-0.02	-0.07	-0.12	0.06	0.0	-0.06	
(3×3)	-0.15	-0.04	0.08	-0.10	0.0	0.10	
(2×2)	-0.15	-0.04	0.10	-0.12	0.0	0.10	
$(\sqrt{3}\times\sqrt{3})$	-0.18	-0.03	0.12	-0.14	0.0	0.14	

Table 4.1: Calculated structural parameters (in a_B) for pure $TiSe_2$ (upperblock) and difference with respect to bulk (middle); shift of atomic plane relativ to bulk (bottom), species given in parenthesis.

4.4 On-surface Adsorption

By studying *isolated* adatoms on surfaces the nature of the pure adsorbate - substrate bond can be analyzed. An accurate knowledge of the binding sites for an adatom and their adsorption energy is crucial to analyse the diffusion barriers the adatom may encounter during its translational motion. In this section, I will focus on the first-principles determination of the binding sites for alkali adatoms on $TiSe_2$ (0001) surface and the activation energies for surface diffusion.

To answer the question whether an alkali adatom can be adsorbed on the $TiSe_2$ (0001) surface, I considered four different surface sites, which are especially denoted by hcp, fcc, on-top, and bridge. The first two sites are referred to the stacking of the uppermost Ti plane, the Se plane above, and a full adsorbate plane. The on-top site coincides with the projected Se positions, and the bridge point lies between two of them, see Figure (4.4). At each site the total energy is minimized simultaneously with respect to the electron charge density, the z coordinate of the adatom, and the positions of the substrate atoms at the first two $TiSe_2$ layers.

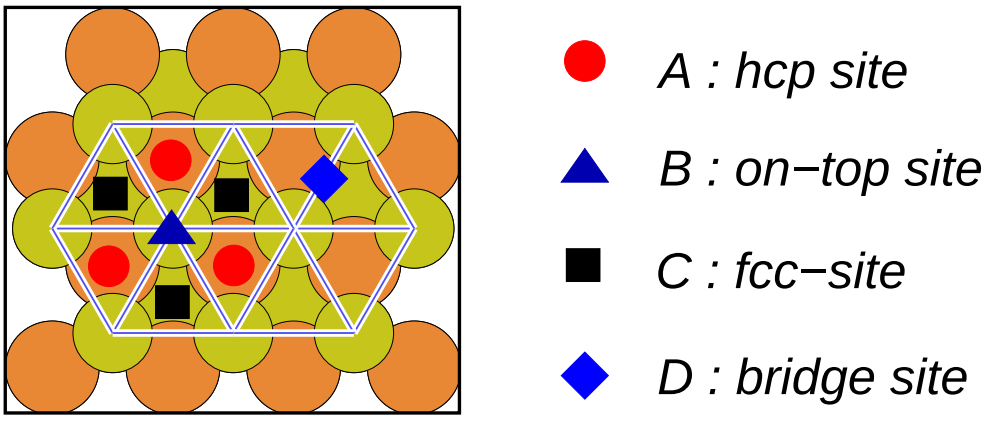

Figure 4.4: Top view of $TiSe_2$ (0001) surface's adsorption sites. The yellow circles represent Se atoms in the first and third atomic plane, and the orange the Ti atoms in the second atomic plane.

It was found that only the hcp and fcc sites are equilibrium adsorption sites, with the hcp (-3.03 eV) energetically slightly preferred over the fcc site (-2.99 eV), see Table 4.2. In both sites the Li adatom is threefold coordinated and forms bonds with the three upper Se atoms. The bridge site is the middle point between hcp and fcc sites, with an adsorption energy of -2.77 eV, while the on-top site represents the maximum in the total energy surface with an energy of -1.90 eV.

The Li-Se bond length increases with increasing coordination number, with (4.26 ± 0.05 a_B) for the onefold on-top, (4.43 ± 0.05 a_B) for the twofold bridge, and (4.58 and 4.50 ± 0.05 a_B) for the threefold hcp and fcc sites, respectively.

Since the barrier height is the *difference* in energies between hcp and the bridge site, the diffusion barrier E_d is 0.26 eV, see Figure (4.6).

The diffusion path, see Figure (4.5), between two hcp sites runs via the direct connection of an adjacent hcp and fcc site over the bridge site. As an adatom moves from a hollow (hcp, fcc) to a bridge site, three Li-Se bonds are replaced by two. To some degree each of the two bonds at the bridge will be stronger than each of the three bonds was in equilibrium. As the adatom moves along the diffusion path its distance to the surface varies: 2.23, 2.82, and 2.48 a_B, at the fcc, bridge and hcp site, respectively.

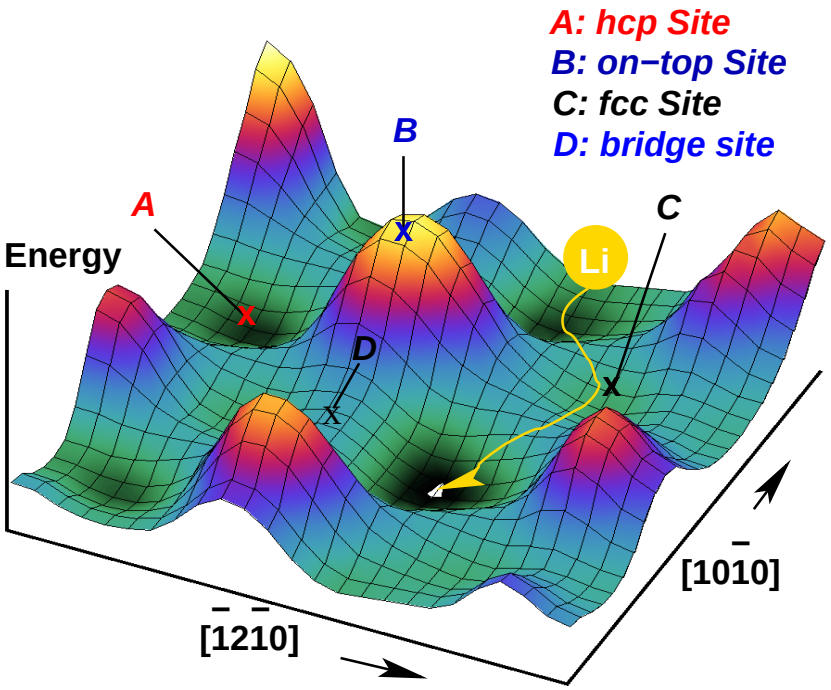

Figure 4.5: Energy surface of Li diffusion on $TiSe_2$ (0001) with a projection of diffusion path (yellow solid line). The values of the energy axis are refered to the cut in Figure (4.6).

In contrast to the results for Li, I found for Na, Rb and Cs that the calculated adsorption energies for the hcp and fcc sites are equal, within the accuracy of the method employed in the present study. For these adatoms the bridge site represents also the saddle point between hcp and fcc, obtaining from their difference the corresponding activation energy E_d. As it can be seen from Table 4.2, E_d becomes lower with increasing alkali atomic radius.

As the atomic radius in the alkali metals increases, ($r^{Li} = 1.51$ Å, $r^{Na} = 1.83$ Å, $r^{Rb} = 2.42$ Å, $r^{Cs} = 2.62$ Å) [82], the adatoms have increasing distance to the surface, (see d_0 in Table 4.3), which implies that they will experience decreasing substrate electron-density and force-field corrugation, and therefore, a lower diffusion barrier. Without calculations I suggest that K will fit into the same pattern.

In Table 4.3 the structural parameters for the different alkali atoms adsorbed on $TiSe_2$ hollow sites are resumed. At the fcc site the adatoms (Li, Na, Rb) sit deeper than at the hcp. Cs instead, adsorbs at the same distance at both sites. When the alkalis are adsorbed at the hcp site, the Ti atom below this site, moves away from the surface (for Li), towards the surface (for Rb and Cs), or does not show any relaxation (for Na), (see Δd in Table 4.3).

The interlayer width (d_{11} + d_{12}) from the first sandwich changes with respect to the clean relaxed $(\sqrt{3} \times \sqrt{3})$ $TiSe_2$ (0001) surface by 0.9, -0.2, -2.0, and -2.5%, for Li, Na, Rb, and Cs situated on hcp site, whereas for all alkali adatoms situated on the fcc site the spacing remains unchanged. For the second interlayer spacing (d_{21} + d_{22}), no difference is found.

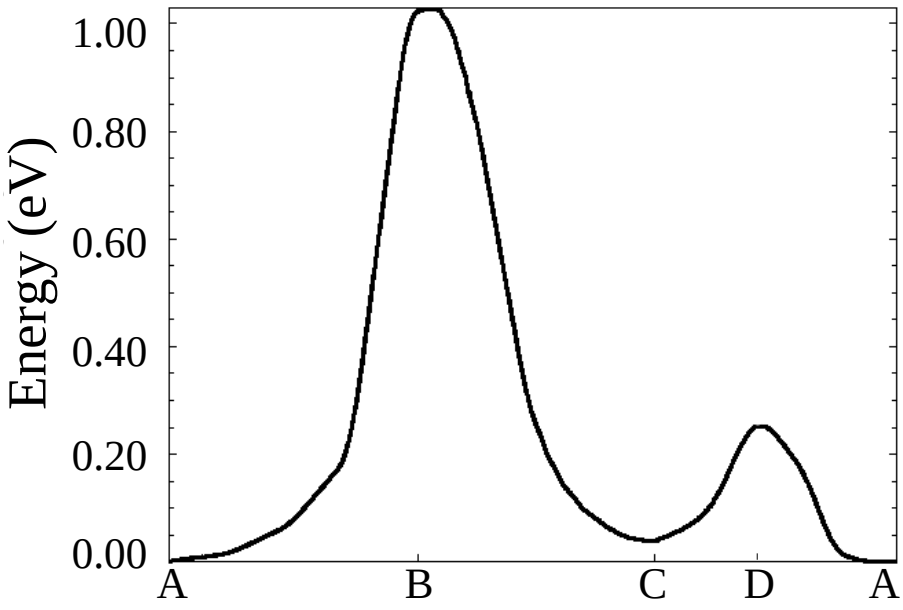

Figure 4.6: One-dimensional cut through the energy surface of Figure (4.5) along the diffusion path.

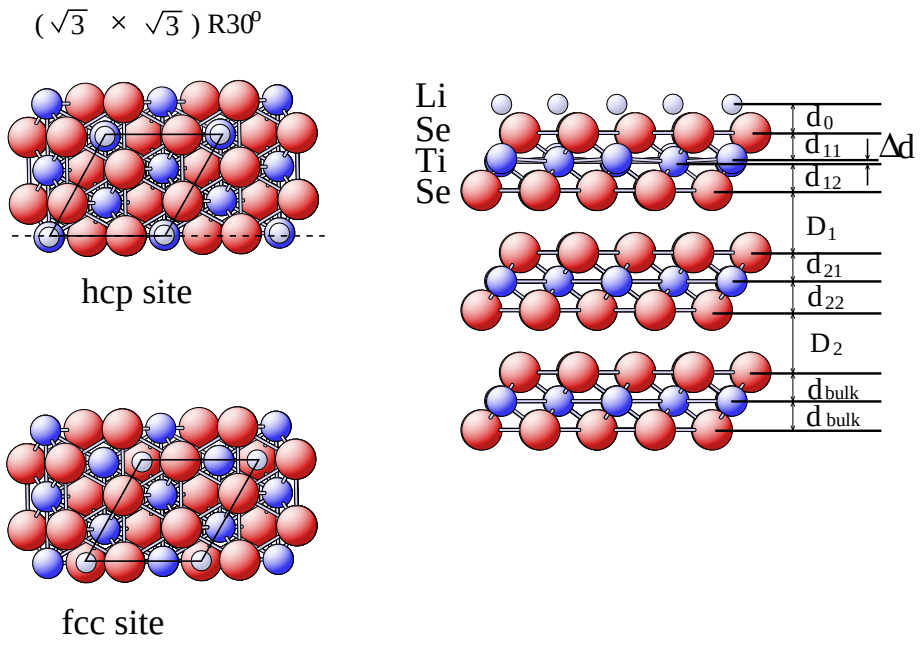

Figure 4.7: Top view (left) and side view (right) of the atomic geometry of $(\sqrt{3} \times \sqrt{3})R30^{\circ}$ Li/$TiSe_2$, with Li adatom on hcp and fcc site. The dashed line (upper left) indicates the plane of the cross section used in the right picture. For the distance values, d_i and D_i, between atomic planes, see Table 4.3.

Alkali Metal	hcp	bridge	fcc	on-top	E_d
Li	-3.03	-2.77	-2.99	-1.98	0.26
Na	-2.61	-2.49	-2.60	-1.81	0.12
Rb	-2.41	-2.35	-2.41	-1.86	0.06
Cs	-2.51	-2.50	-2.51	-2.08	0.01

Table 4.2: Alkali adatom's adsorption energies on $TiSe_2$ (0001) at hcp, bridge, fcc, and on-top sites, and diffusion barrier $E_d = E_{ads}^{hcp} - E_{ads}^{bridge}$, (in eV).

In Table 4.4, the magnitude of the alkali-Se bond lengths are summarized. For the four alkalis studied, the adsorbate-substrate bond becomes longer with the increase of

coordination. In the hcp and fcc sites, the valence electrons are shared among many bonds, thus, each single bond becomes weaker, and an increase of the bond length results.

	d_0	d_{11}	d_{12}	Δd	D_1	d_{21}	d_{22}	D_2	d_{bulk}
Li+$TiSe_2$									
hcp site	2.48	2.94	2.77	-0.05	6.07	2.83	2.83	6.11	2.97
fcc site	2.23	2.90	2.76	0.00	6.10	2.83	2.83	6.11	2.97
Na+$TiSe_2$									
hcp site	3.44	2.89	2.76	0.00	6.19	2.83	2.83	6.10	2.97
fcc site	3.35	2.89	2.79	0.00	6.19	2.83	2.83	6.10	2.97
Rb+$TiSe_2$									
hcp site	4.91	2.83	2.74	0.08	6.04	2.83	2.83	6.10	2.97
fcc site	4.88	2.88	2.77	0.00	6.00	2.83	2.83	6.08	2.97
Cs+$TiSe_2$									
hcp site	5.29	2.79	2.73	0.12	5.99	2.83	2.83	6.09	2.97
fcc site	5.29	2.88	2.77	0.00	6.06	2.83	2.83	6.08	2.97

Table 4.3: Calculated structural parameters (in a_B) for alkali adatoms adsorbed on $TiSe_2$(0001) hollow sites.

Alkali Metal	hcp	fcc	bridge
Li	4.58	4.50	4.43
Na	5.18	5.14	5.01
Rb	6.27	6.25	6.12
Cs	6.58	6.57	6.44

Table 4.4: Bond length (in a_B) between alkali and Se atom.

4.4.1 Difference electron density

From an experimental point of view, the determination of the adsorption positions relatively to substrate sites is relative difficult. From a theoretical point of view, it is clear that for a given substrate the adsorption sites must depend on the direction of charge transfer between substrate and adsorbate, which is governed by the electronic affinity of the adatom, the charges being displaced toward the more electronegative element. Naturally, reliable information can only be given by comparing the adsorption energies for various positions, as done in section 4.4. However, the knowledge of the surface charge density can give some qualitative information.

To gain more insight into the nature of the bonding, I take the total charge density of the Li/$TiSe_2$ surface and substract the charge density of the clean $TiSe_2$ surface as well as the charge density of a free Li adatom (with the same Li-Li spacings as in the overlayer on the $TiSe_2$ surface).

The resulting charge density differences (Figure (4.8)), when Li is adsorbed on the hcp site (upper) and fcc site (lower) on $TiSe_2$ (0001), reveal the charge redistribution upon alkali adsorption. In both cases the charge transfer from the adsorbate towards the substrate is clearly visible. From the vacuum side the lithium looks practically without charge. The first displayed contour near the lithium position has a very low value, indicating that Li is a ionized adatom. This is in accordance with what is expected from electronegativity considerations: Li is electropositive with respect to the neighboring Se atoms, i.e., it gives up an electron more readily than Se. The electron density is accumulated in the region between Se and Li as well as in the position of the Ti orbitals, being in the latter position where the maximum of the charge density difference is located. The orbitals involved in this charge transfer can be clearly identified from the charge difference plots.

When the adatom is adsorbed on the hcp site the electron clouds localized at the Ti site have the shape of a *d*-type orbital, a mixture of d_{z^2}, d_{xz} and d_{yz} with prominence of the first one, with the lobes pointing to the Li position. This is also true for the fcc position of the adatom but d_{xz} and d_{yz} becoming more important. The perturbation of the system caused by the adsorbate does not reach far into the substrate, thus only the changes in the first $TiSe_2$ sandwich are shown. The charge density is essentially identical to that of the clean surface for layers deeper than the first sandwich.

In Figures (4.9) and (4.10) also the charge difference densities induced by Rb adsorption on the $TiSe_2$ hcp and fcc sites are shown. From the contour plots presented in Figure (4.9) it can be seen that the changes in the charge density distribution are similar whether the adsorption site is a hcp or a fcc site. A charge accumulation between the alkali adatom and the Se atoms is observed, showing some noticeable angular polarization. There is also charge transfer to the *d*-orbitals of Ti. From Figure (4.10) these changes of charge density distribution (with Rb adatom on fcc site) can be observed for different planes parallel to the (0001) surface. It is clear that the charge accumulation is located between the Se and the adatom position. The d_{xz} and d_{yz} orbitals of Ti atom can be also easily identified.

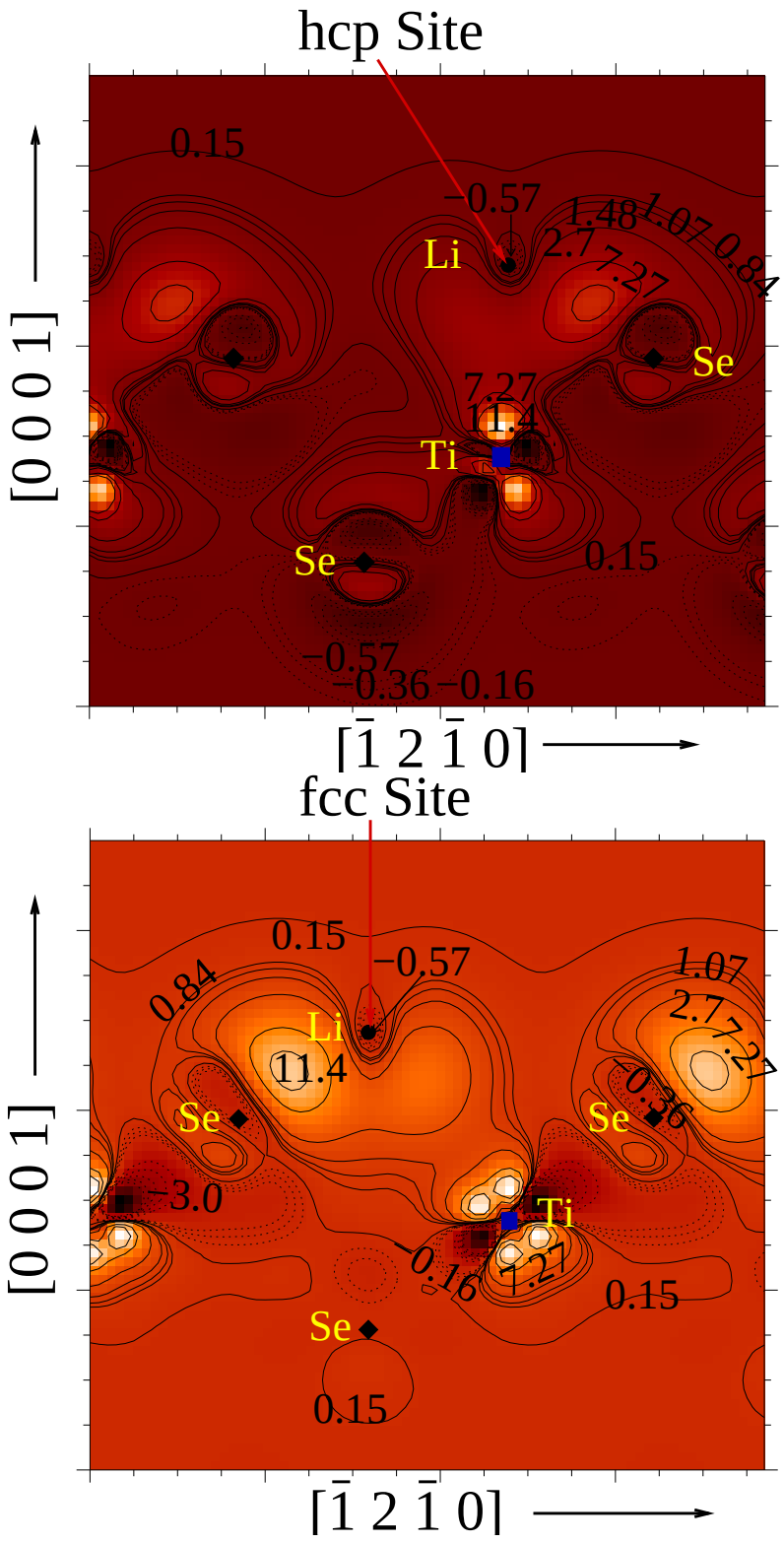

Figure 4.8: Contour plots of the electron difference density $n^{\Delta}(\mathbf{r})$, when Li is adsorbed on the (upper) hcp and (lower) fcc sites, considering for the free adatom the neutral charge state. The figure shows contours in the plane normal to the (0001) surface and the horizontal axis parallel to the $[\bar{1}2\bar{1}0]$ axis. Circles denote Li-, diamonds Se- and squares Ti-atoms. Countour units are 10^{-3} $a_B{}^{-3}$.

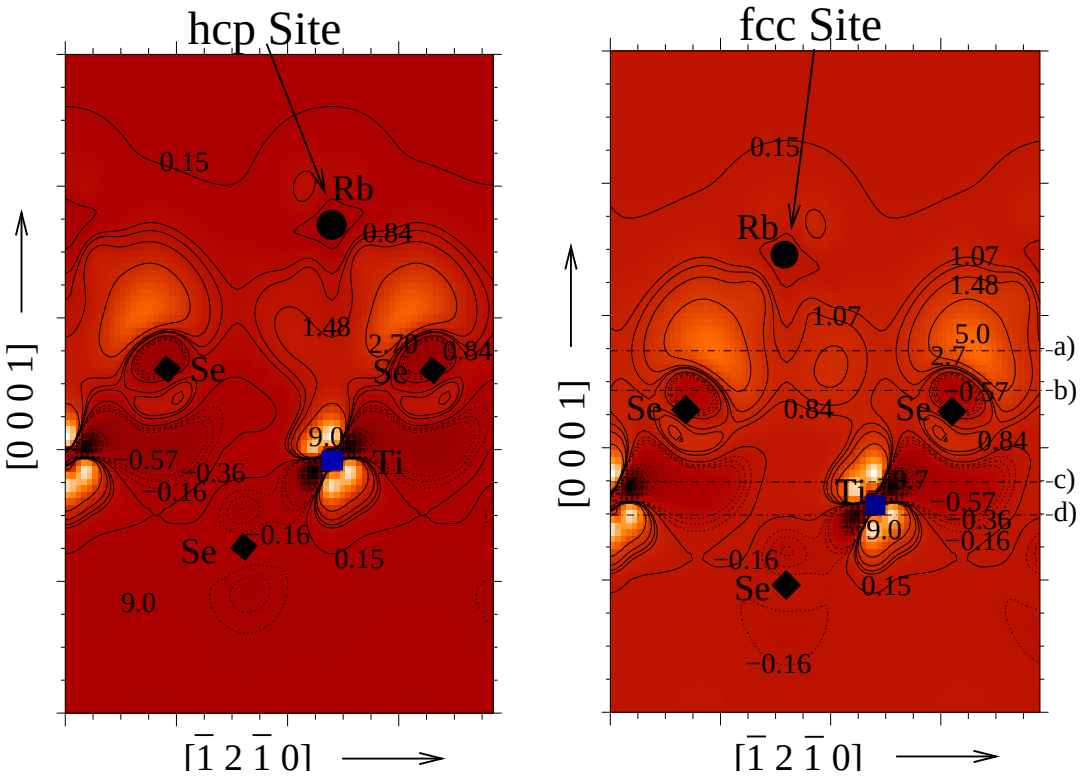

Figure 4.9: Contour plots of the electron difference density, $n^{\Delta}(\mathbf{r})$, for Rb adsorbed on the (left) hcp and (right) fcc $TiSe_2$ sites . Broken lines in (right) plot indicate the planes of the cross section plotted in Figure (4.10 a-d). The figure shows contours in the plane normal to the (0001) surface and the horizontal axis parallel to the $[\bar{1}2\bar{1}0]$ axis. Circles denote Rb-, diamonds Se-, and squares Ti- atoms. Contour units are 10^{-3} $a_B{}^{-3}$.

4.5 Changes with Li Coverage

4.5.1 Change in the surface atomic geometry

One of the interesting characteristics of alkali metal adsorption is the change of several physical quantities as a function of coverage. The most obvious of these properties are the surface atomic geometry and the work function. To learn about the coverage dependence of the surface atomic arrangements and related properties, calculations at five coverages, $\Theta = 0.06$, 0.25, 0.33, 0.5, and 1 ML, of Li adsorbed on $TiSe_2$ (0001) surface, have been performed. Here I present the results of the structure optimization for the different coverages of Li on the hcp site.

Different parameters were obtained, among the important ones are the distance between the adatom and the surface, the bond length Se-Li, the inter- and intra-layer

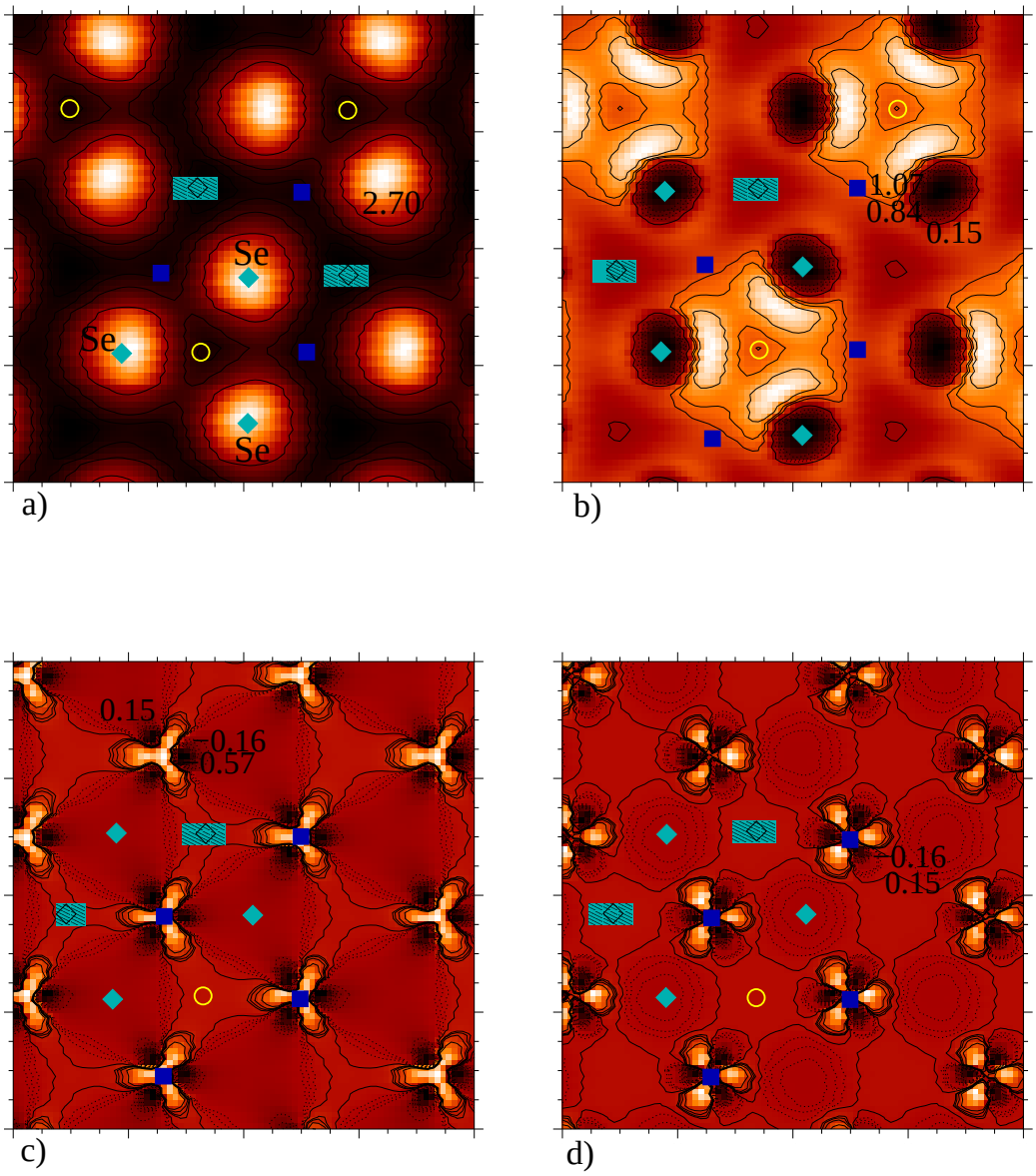

Figure 4.10: Charge density difference plot, $n^{\Delta}(\mathbf{r})$, for Rb on $TiSe_2$ fcc site. The contour plots are from planes parallel to the (0001) surface of the system. The cross section plotted in a),b),c),d) are referred to Figure (4.9)(right picture), where they are indicated by the dashed lines. see Figure (4.9). Circles denote Rb-, diamonds Se-(in the first atomic plane), hatched diamonds Se-(in the third atomic plane), and squares Ti- atoms. Contour units are 10^{-3} bohr^{-3}.

Li adsorbed on $TiSe_2$ (0001)									
Coverage	d_0	d_{11}	d_{12}	Δd	D_1	d_{21}	d_{22}	D_2	Li-Se
0.06	2.58	3.12	2.91	-0.10	5.66	3.03	3.03	5.89	4.64
0.11	2.60	3.00	2.72	-0.12	5.74	2.87	2.86	6.05	4.65
0.25	2.48	2.97	2.71	-0.06	5.99	2.85	2.87	5.82	4.59
0.33	2.48	2.94	2.77	-0.05	6.07	2.83	2.83	6.11	4.58
0.50	2.36	3.00	2.80	-0.04	5.89	2.85	2.87	5.85	4.52
1.00	2.49	3.09	2.75	0.00	5.94	2.85	2.87	5.80	4.56

	Δd_{11}	Δd_{12}	ΔD_1	Δd_{21}	Δd_{22}	ΔD_2
0.06	0.09	-0.12	-0.10	0.00	0.00	0.00
0.11	0.15	-0.13	-0.39	0.00	0.00	0.00
0.25	0.11	-0.13	-0.18	0.00	0.00	-0.23
0.33	0.12	-0.06	-0.13	0.00	0.00	0.02
0.50	0.14	-0.04	-0.28	0.00	0.00	-0.20
1.00	0.23	-0.09	-0.23	0.00	0.00	-0.24

relaxation Δz of atomic plane with respect to pure $TiSe_2$

	1rst (Se)	2nd (Ti)	3rd (Se)	4th (Se)	5th (Ti)	6th (Se)
0.06	-0.13	-0.22	-0.10	-0.00	-0.00	0.00
0.11	-0.37	-0.52	-0.39	0.00	0.00	0.00
0.25	-0.45	-0.56	-0.42	-0.24	-0.24	-0.23
0.33	-0.09	-0.21	-0.15	0.02	0.02	0.02
0.50	-0.38	-0.52	-0.48	-0.20	-0.20	-0.20
1.00	-0.34	-0.57	-0.48	-0.25	-0.25	-0.24

Table 4.5: Calculated structural parameters (in a_B) for Li at the $TiSe_2$ (0001) surface, with different coverages (upperblock) and difference with respect to pure $TiSe_2$ (middle); shift of atomic plane relativ to pure $TiSe_2$ (bottom), species given in parenthesis. See Figure (4.7).

spacings, the lateral and vertical displacements of the adatom and substrate atoms, and the van der Waals gap width.

The calculated vertical spacings d_i are listed in Table 4.5. It can be seen, that on increasing the coverage from very low coverage (0.06 ML), where the Li adatoms are uniformly spread over the surface, to higher coverages the distance from the Li adatom to the surface roughly decreases and varies from 2.58 a_B for 0.06 ML to 2.36 a_B for 0.5 ML. For 1.0 ML the distance increases to 2.49 a_B. The change in the Li-Se distance is also reflected in the bond length.

In the upperblock of Table 4.5, the optimized inter- and intra-layer distances of the substrate are resumed. By comparing these values with those of the clean relaxed substrate, see Table 4.1, the geometrical changes induced by the adsorbate are found, see Table 4.5 (middle block). For all coverages the first interatomic spacing d_{11} increases as a result of an inward displacement of the Ti atomic plane, see Table 4.5 (bottom), whereas the second interatomic spacing d_{12} decreases. The van der Waals width, ΔD_1, decreases for all coverages by about 2-6 % with respect to the pure surface.

At the adsorption geometries, with a Li-coverage of $\Theta = 0.06$, 0.11, 0.25, 0.33, and 0.5 ML, the three Se atoms in the first atomic plane coordinated to the Li adatom move radially away from it. The calculated amplitudes of these in-plane displacements are 0.04 a_B for the first three coverages and 0.03 a_B for the two last. Also small bucklings towards bulk are obtained in these three Se atoms of about 0.04, 0.01, 0.03 a_B for $\Theta =$ 0.06, 0.11, and 0.5 ML, respectively.

The Ti atom localized in the second plane, directly below the adsorbed Li, moves inwards, i.e., to the bulk, with respect to the rest of Ti atoms in the same atomic plane, by 0.10, 0.12, 0.06, 0.05, and 0.04 a_B, for $\Theta = 0.06$, 0.11, 0.25, 0.33, and 0.5 ML, respectively.

For the highest coverage of $\Theta = 1$ML, unlike the lower-coverage cases, no in-plane relaxation is obtained due to the symmetry of the unit cell. The first interlayer spacing is 0.23 a_B larger than in the corresponding clean substrate. The Ti atoms are shifted towards bulk by 0.57 a_B, with respect to the clean surface. The relaxed Li-Se bond length is 4.56a_B, with Li adatom 2.49 a_B above the closest Se layer.

For the structures with a Li-coverage of $\Theta = 0.25$, 0.5, and 1.0 ML, the three atomic planes of the second $TiSe_2$ layer shift inwards by the same amount; thus, no changes in the interlayer spacings with respect to the clean surface are obtained, but a reduction in the intralayer spacing ΔD_2 of about 4%. For the rest of the coverages the second $TiSe_2$ layer keeps the relaxed position of the pure structure. No in-plane relaxations are found in the three atomic planes of the second $TiSe_2$ layer for any coverage.

4.5.2 Change in the work function

The work function, Φ, of a crystal surface is defined as the energy required to extract an electron at the Fermi level from the bulk region of a crystal to the vacuum at infinity.

For years alkali metal adsorption on metallic surfaces has been investigated thor-

oughly. In 1932 Langmuir [83] proposed a model to explain the interaction between these adatoms and surfaces, and which was extended in 1935 by Gurney [84]. According to their model, in a first adsorption phase the low ionisation potential of alkali metals induces a charge transfer when adsorbed on more electronegative substrates. Each partially positively charged adatom then builds up a dipole with the substrate, pointing from the negatively charged substrate to the adatom. This dipole orientation facilitates the escaping of the electrons to the vacuum, i.e. the work function of the clean substrate will strongly decrease. The electrostatic repulsion between the charged alkali ions increases with the coverage. Thus, in a second adsorption phase charge from the substrate feeds back to the alkali metal to weaken the repulsion between alkali ions, inducing an increase of the work function. At higher coverages the work function reaches a saturation level with the value of the bulk alkali metal.

Φ (eV)	(4×4)	(3×3)	(2×2)	$(\sqrt{3}\times\sqrt{3})$
	5.2	5.4	5.4	5.5

Table 4.6: Work function of pure $TiSe_2$ (0001) surface, calculated for different supercells.

The calculated average work function of the clean $TiSe_2$ (0001) surface is Φ=5.3 $\pm$ 0.1 eV, see Table 4.6, in excellent agreement with experiment (5.3 eV) [13].

Figure (4.12) shows the calculated work function change $\Delta\Phi$ as a function of Li coverage. This curve has the characteristic shape found for systems of alkali metal adsorbed on metallic surfaces. Initially, it shows a rapid lowering of the Φ, to a minimum (Φ_{min}= -3.2 eV) at Θ = 0.5 ML, and subsequently an increase at Θ = 1.0 ML (Φ= -2.8 eV).

Such a decrease in the work function upon lithium adsorption reflects the electropositive nature of Li that results in an induced dipole moment $\mu(\Theta)$.

The final increase of Φ has been attributed to a metallization of the alkali overlayer [85, 86]. Taking Φ= 5.3 eV as the value of clean $TiSe_2$ (0001), I obtained a work function of 2.5 eV at 1 ML. Comparing this with the experimental value of Φ=2.93 eV for Li bulk [87], it can be seen that at 1 ML the saturation level has not yet been reached.

In Figure (4.11) the adsorption energy of Li (hcp site) as a function of coverage is presented. It has been found that when increasing the Li coverage from 0.06 to 0.25 ML, the adsorption energy increases (-3.57 to -2.93 eV), indicating a repulsion between adatoms. With increasing coverage the adsorption energy meets its minimum

at Θ= 0.33 ML. From 0.5 to 1 ML the adatoms have to occupy next neighbor sites separated from each other by a distance of 6.61 a_B, which approaches the Li-bulk lattice constant (6.42 a_B) [88]. This gives rise to a strong repulsion between adatoms, which is reflected in the increase of the adsorption energy.

Figure (4.12) shows how the adsorbate-induced dipole moment μ changes with increasing coverage. The coverage dependence of the induced dipole per adatom is a consequence of the dipole-dipole interaction, that gives rise to a depolarization with decreasing Li-Li distance.

As a rough estimation of the charge at the Li atom (with Θ = 0.33, 0.5 and 1 ML), I calcultated the dynamic charge, i.e., the slope of the curve obtained when plotting the surface dipole moment versus vertical distance of Li to the surface. The dynamic charge is of interest to discuss how the bond between the adsorbed alkali metal atom and the surface is best described, whether the adsorbate should be regarded as partly ionic due to a charge transfer to the substrate or as essentially neutral but strongly polarized.

At the three coverages studied, I obtained a linear dependence of the dipole moment with probing a small increase of the adsorbate's distance to the substrate's first atomic plane, indicating a ionic bonding between Li adatom and the substrate. At Θ = 0.33 and 0.5 ML the dynamic charge values are 0.4 and 0.2 electron, whereas at Θ = 1.0 ML the value is -0.3 electron. The decrease and change in sign indicates a flow of charge from the substrate to the adatoms. In Table 4.7 are resumed the adsorption energy, the change in work function, the dipole moment, and the distance from adatom to surface as a function of Li coverage.

Coverage	E_{ads} (eV)	$\Delta\Phi$ (eV)	μ (Debye)	d_0 (a_B)
0.06	-3.57	-0.9	-3.3	2.58
0.11	-3.48	-1.2	-2.8	2.60
0.25	-2.93	-2.3	-2.3	2.48
0.33	-3.03	-2.7	-2.0	2.48
0.50	-2.65	-3.2	-1.6	2.36
1.00	-2.53	-2.8	-0.7	2.49

Table 4.7: Surface: adsorption energy, change in work function, dipole moment, and distance from adatom to surface as a function of Li coverage.

4.5.3 Change in the charge density

In Figures (4.13, 4.14, 4.15) the charge density difference, $n^{\Delta}(\mathbf{r})$, of Li_x adsorbed on $TiSe_2$, (x = 0.06, 0.5, and 1.0 ML) are shown. For the definition of $n^{\Delta}(\mathbf{r})$ see eq. 4.2. On

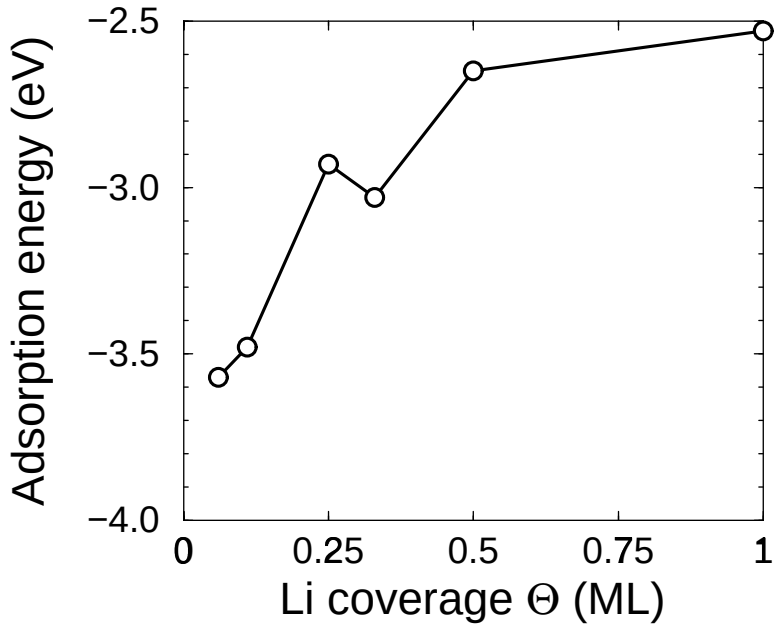

Figure 4.11: Adsorption energy versus coverage for Li on $TiSe_2$ in the hcp (on-surface) sites.

each figure different planes are displayed in order to have a better view of the charge transfer resulted from the adsorption of Li with different coverages. In Figure (4.13), where the amount of Li is very low (x=0.06), most of the charge is located between the Li and the Se atoms that are next to it. Since the Li adatom is adsorbed on the hcp site, also the 3*d* orbitals of the Ti atom below this site, point to the Li position. When the amount of Li increases to x = 0.5 the Ti 3*d* orbitals of the atoms below the adsorption sites seem to be a mixture of d_{z^2}, d_{xz} and d_{yz} with prominence of the first one, whereas for the rest of Ti atoms the d_{xz} and d_{yz} are more important. Also in this case, most of the charge is localized between Li and the Se atoms. Since the Li adatom is adsorbed closer to the surface with x = 0.5 than with x=0.06 coverage, more charge is localized in Ti 3*d* orbitals. With x = 1.0 the charge cloud between the adsorbate and the Se atoms reaffirms that charge is displaced from the vacuum side of the Li towards the substrate side.

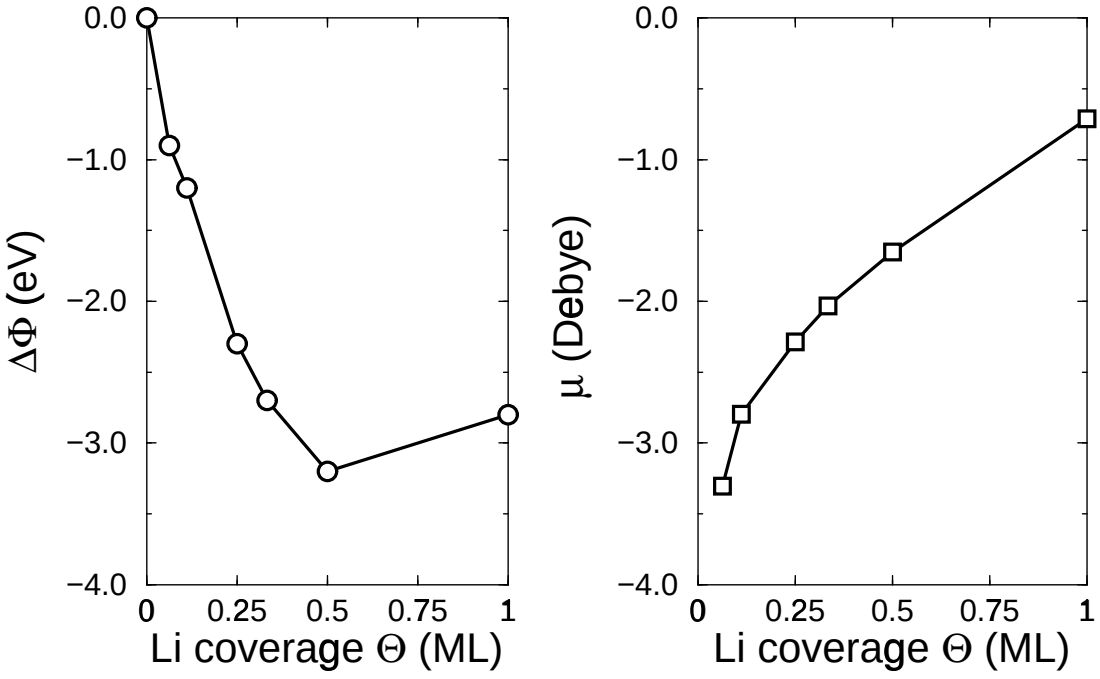

Figure 4.12: (left) Work function change, (right) surface dipole moment for Li on $TiSe_2$ versus Li coverage. Lithium atoms occupy the hcp (on-surface) sites.

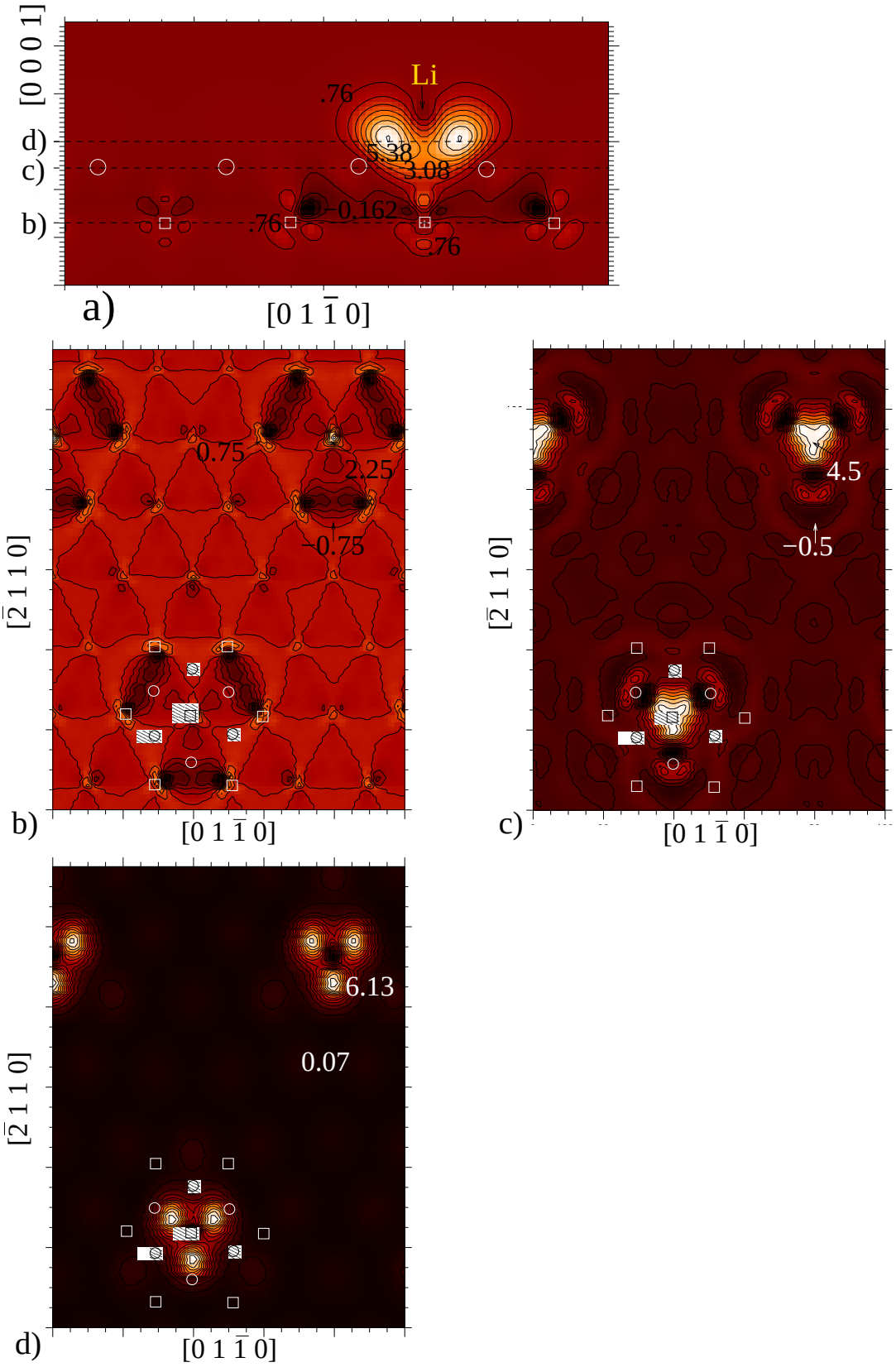

Figure 4.13: Charge density difference, $n^{\Delta}(\mathbf{r})$, of the Li_x adsorbed on $TiSe_2$ system , with $x = 0.06$) for Li in the hcp site. For the definition of $n^{\Delta}(\mathbf{r})$ see equ. 4.2; n^{Li} is taken from a free, neutral atom. The dashed lines in a) indicate the plane of the cross section used in b - d). Open circles indicate position of Se atoms in first atomic plane, hatched circles Se atoms in third atomic plane, squares Ti atoms, and hatched square Li adatom. The contours are displayed in a) a plane perpendicular to the (0001) surface, b)-d) a plane parallel to (0001). The units are 10^{-3} bohr^{-3}.

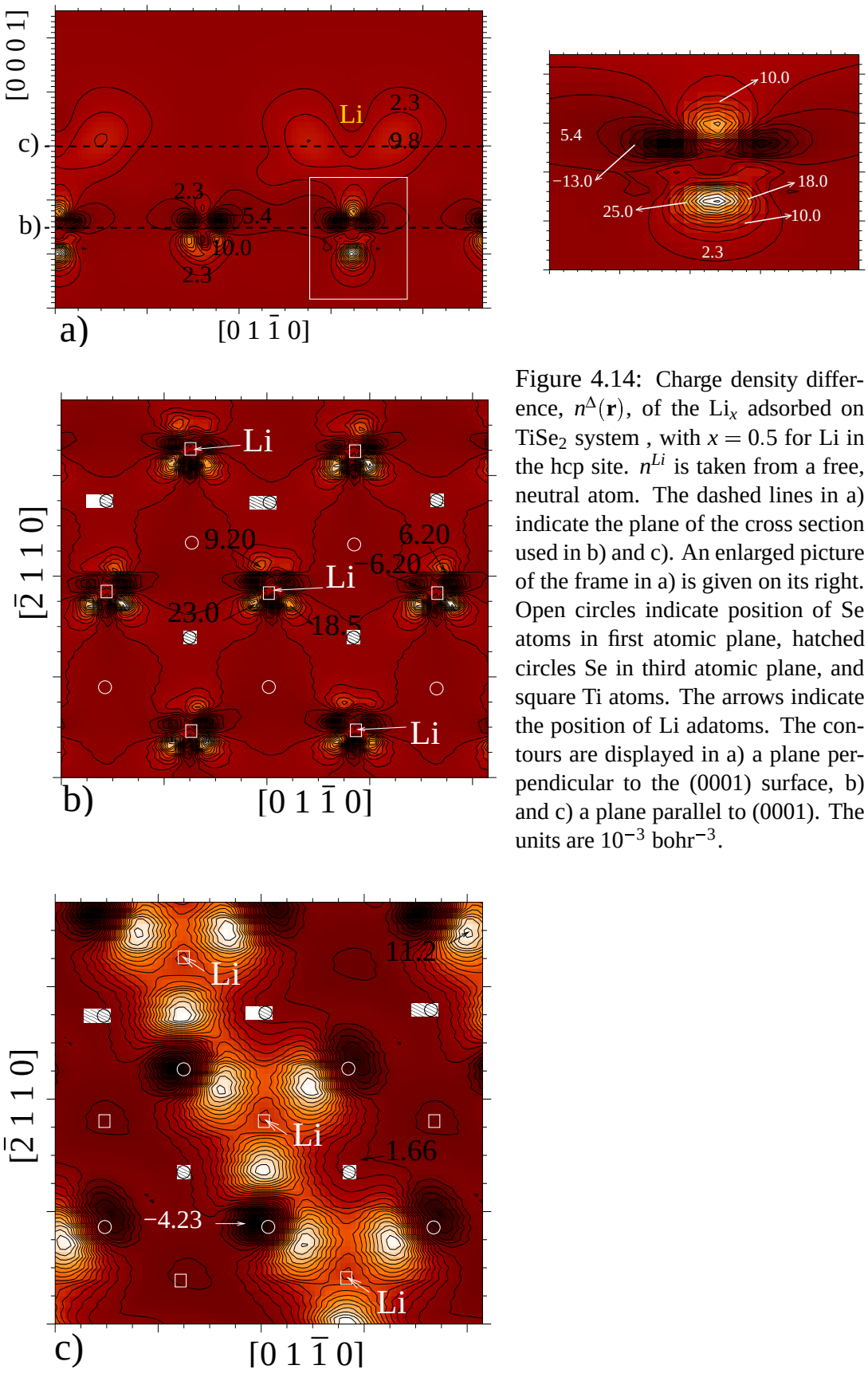

Figure 4.14: Charge density difference, $n^{\Delta}(\mathbf{r})$, of the Li_x adsorbed on $TiSe_2$ system , with $x = 0.5$ for Li in the hcp site. n^{Li} is taken from a free, neutral atom. The dashed lines in a) indicate the plane of the cross section used in b) and c). An enlarged picture of the frame in a) is given on its right. Open circles indicate position of Se atoms in first atomic plane, hatched circles Se in third atomic plane, and square Ti atoms. The arrows indicate the position of Li adatoms. The contours are displayed in a) a plane perpendicular to the (0001) surface, b) and c) a plane parallel to (0001). The units are 10^{-3} bohr^{-3}.

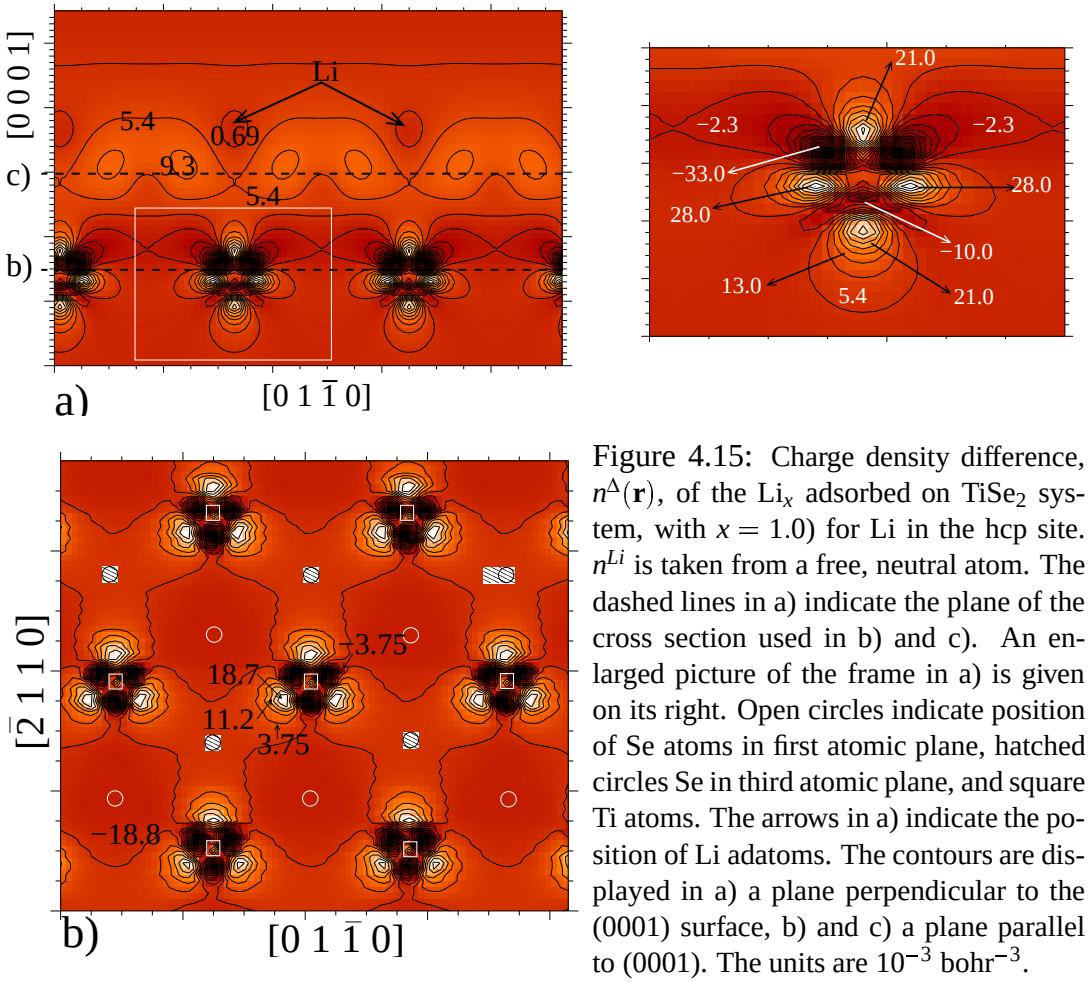

Figure 4.15: Charge density difference, $n^{\Delta}(\mathbf{r})$, of the Li_x adsorbed on $TiSe_2$ system, with $x = 1.0$) for Li in the hcp site. n^{Li} is taken from a free, neutral atom. The dashed lines in a) indicate the plane of the cross section used in b) and c). An enlarged picture of the frame in a) is given on its right. Open circles indicate position of Se atoms in first atomic plane, hatched circles Se in third atomic plane, and square Ti atoms. The arrows in a) indicate the position of Li adatoms. The contours are displayed in a) a plane perpendicular to the (0001) surface, b) and c) a plane parallel to (0001). The units are 10^{-3} bohr^{-3}.

4.6 Diffusion in van der Waals gap

In this section I will discuss, the energetics and structural changes of Li_xTiSe_2, ($0.06 \leq x \leq 1.0$), with Li situated in the first interlayer region of $TiSe_2$. By means of total energy calculations I determined Li atom's most stable positions in the van der Waals gap, and the energy barriers for diffusion along it.

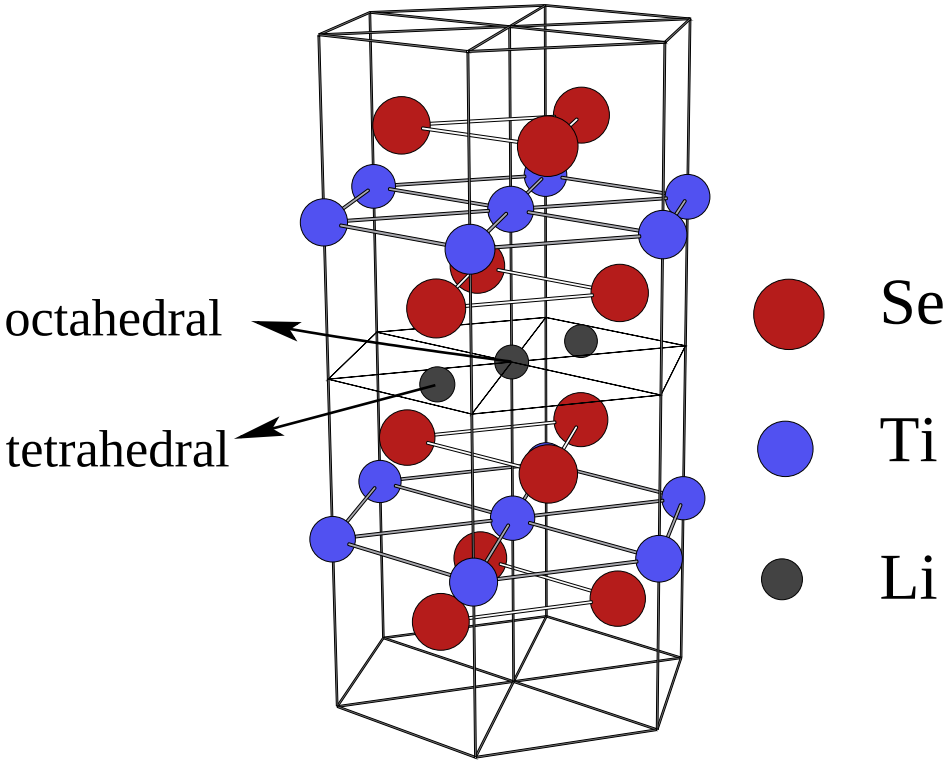

Figure 4.16: Structure model of $TiSe_2$, showing occupation sites in the van der Waals gap. The gray balls show the three inter-sandwich sites, (one octahedral and two tetrahedral).

Pure $TiSe_2$ cristallizes with the 1T-CdI_2 structure, where the metal is octahedrally coordinated by the chalcogen atoms and the layers are stacked without lateral displacements. When intercalation occurs, the intercalant enters the van der Waals gaps between the layers. In Figure (4.16) the three interstitial sites available in the van der Waals gap are shown: one octahedral, which is surrounded by six chalcogen atoms, and two tetrahedrals, which lie immediately below and above the chalcogen atoms.

Using a $(\sqrt{3} \times \sqrt{3})$ supercell (with 3 slabs of $TiSe_2$ and a vacuum space of about 15 a_B), I calculated the total energies of Li_xTiSe_2, (x=0.33), with Li occupying the different interstitial sites. I found the octahedral site to be energetically more favorable

than both tetrahedral, the latter ones having the same energy. The results are listed in Table 4.8. The corresponding binding energies, for all interstitial sites, are markedly lower than the ones in the surface. This reflects the fact that the interlayer sites are considerably more favorable. Most important, it demonstrates the strong tendency of $TiSe_2$ towards intercalation and the stability of the intercalated compound.

Alkali Metal	octahedral	bridge	tetrahedral
Li	-3.58	-3.15	-3.22

Table 4.8: Adsorption energies (in eV) for Li atom in the $TiSe_2$ van der Waals gap at octahedral, bridge, and tetrahedral sites.

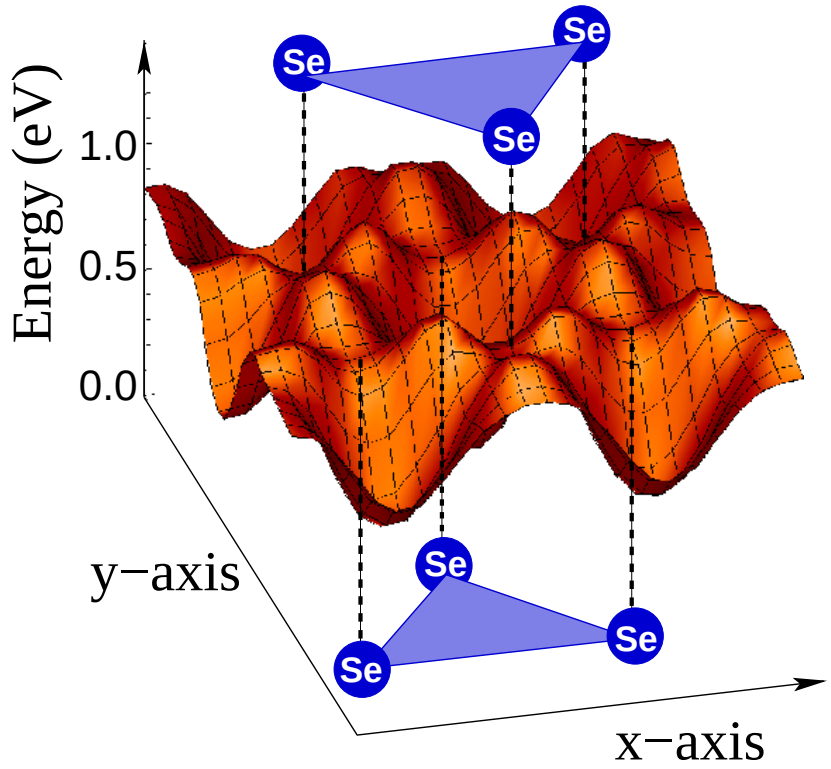

Figure 4.17: Total energy of Li diffusion within the van der Waals gap of $TiSe_2$ bulk.

The migration of Li along the van der Waals gap can be described as a hopping between these sites. To study the diffusion path of Li atom, I calculated the total energy of the system at different configurations, where Li was placed on an equidistant mesh of points, that connect the octahedral and tetrahedral sites. I found that the most favorable diffusion pathway from octahedral to octahedral site involves the intermediate

occupation of a tetrahedral site. Both sites are separated by a saddle point (bridge site) with a binding energy of -3.15 eV. The energy difference between the octahedral and bridge site gives a diffusion barrier value of 0.43 eV.

When the Li atom diffuses within the van der Waals gap (octahedral $\rightarrow$ bridge $\rightarrow$ tetrahedral), the interlayer distance at each site increases (relative to the pure $TiSe_2$) by about 0.2 %, 4.5 % and 6.1 %, respectively, see Table 4.9. At the octahedral site the Li stays at the middle of the van der Waals gap (about 3.1 a_B distance to each layers). At the bridge site the Li relaxes closer to the lower layer (3.6 a_B and 2.8 a_B to the upper and lower layers, respectively). At the tetrahedral site, which lies immediately below a chalcogen atom, the Li stays at a distance of 4.4 a_B and 2.1 a_B from the upper and lower layers, respectively. At the other tetrahedral site, the distances are the same but in the opposite order.

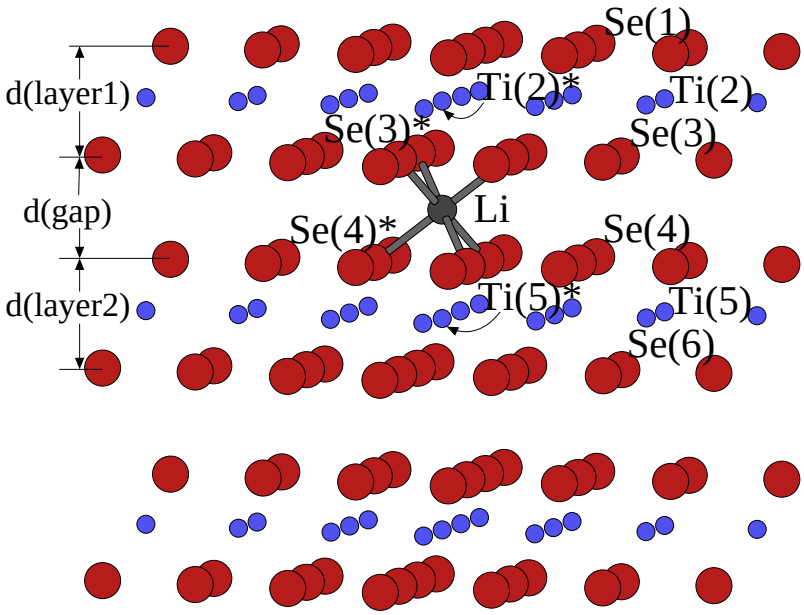

Figure 4.18: Geometric structure of Li_xTiSe_2, with x = 0.06. Number of atomic plane in parenthesis is given for each species. The asterisks denote atoms that form bonds with Li.

For comparison, I determined also the diffusion barrier for Li in the van der Waals gap but with a bulk calculation, i.e., using a (1×1) $TiSe_2$ unit cell with a_{LiTiSe_2}=6.61 a_B, and c_{LiTiSe_2}=11.90 a_B as lattice constants. The total energy was calculated for different configurations, where the Li atom was fixed at equidistant points of the unit cell, and was allowed to relax only in the z-direction. The grid spacing was $1/4$ the distance between tetrahedral and octahedral sites. The Figure (4.17) shows the energy surface obtained.

The diffusion path is similar to that obtained with the supercell model, but the activation barrier increases to 0.6 eV.

To study the dependence of varying concentration x for Li_x, six cases (x = 0.06, 0.11, 0.25, 0.33, 0.5, 1.0) have been investigated. The lithium intercalation complexes of $TiSe_2$ (usually written as Li_xTiSe_2) retain the basic structure of the original $TiSe_2$ lattice. As x increases the Li atoms occupy the octahedral sites in the van der Waals region [52].

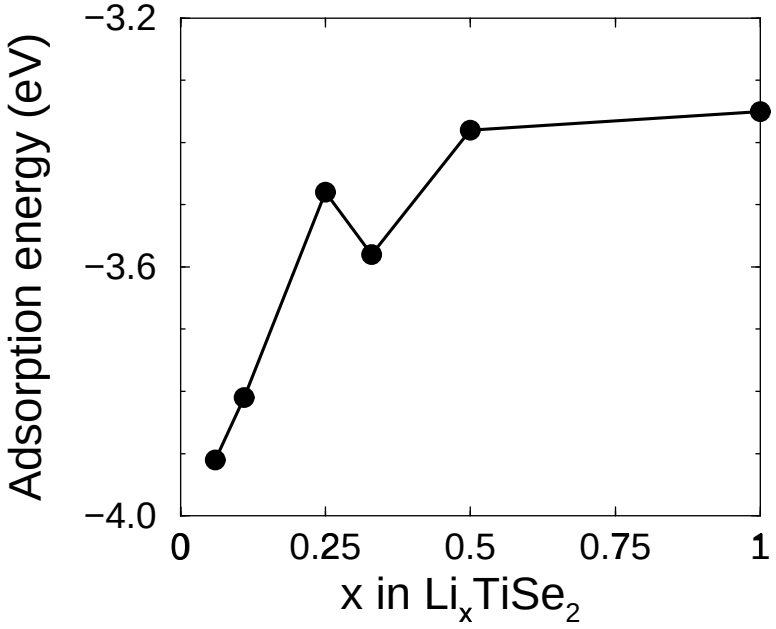

Figure 4.19: Adsorption energy per Li atom versus x Li in the octahedral (van der Waals) sites.

With increasing x, I found that the energy increases linearly from -3.91 eV (at x = 0.06) to a maximum of -3.48 eV (at x = 0.25), then decreases to reach a local minimum of -3.58 eV (at x = 0.33), and then increases again to reach a value of -3.36 eV (at x = 1.0),see Figure (4.19) and Table 4.10. Even at low concentration of Li, an electrostatic repulsion of the ions is obtained. Hibma [89] showed that the repulsion between intercalated alkali is significant only within one lattice constant. From the increasing trend of the energy, the formation of Li island or clusters with $x > 0.5$ is excluded. For Li_xTiS_2 an ordered $(\sqrt{3} \times \sqrt{3})$ superstructure was observed [89], which according to the present calculations, should be the energetically most stable structure. In UHV intercalation only limited concentrations of alkali intercalated have been reported [13, 90, 91, 92, 93, 94]. This has been attributed to the existence of a diffusion barrier for the alkali ions [94].

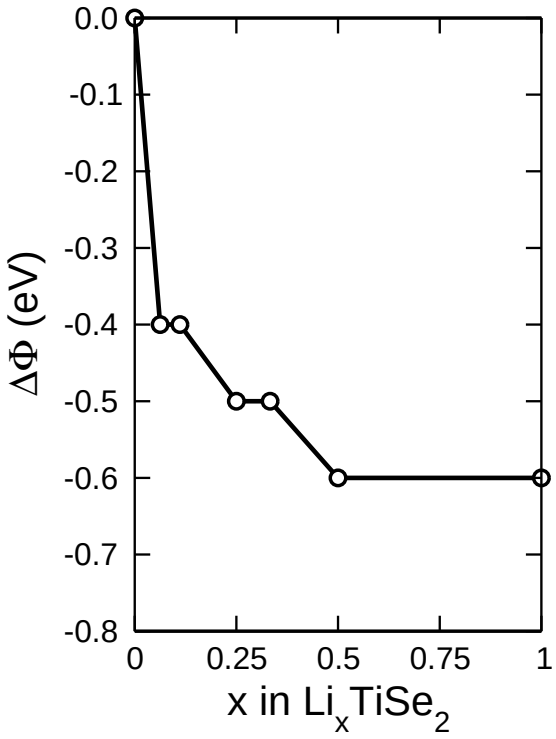

Figure 4.20: Work function change for Li in $TiSe_2$ versus *x* Li. Lithium atoms occupy the van der Waals octahedral sites.

Coverage		Li_xTiSe_2 d(layer1)	d(layer2)	d(gap)	d_zSe(3*,4*)
0.06		6.07	6.06	5.79	5.92
0.11		5.72	5.75	5.96	6.03
0.25		5.70	5.67	6.09	6.10
0.33	octahedral	5.65	5.67	6.21	6.21
	bridge	5.69	5.70	6.19	6.48
	tetrahedral	5.68	5.65	6.36	6.58
0.50		5.67	5.70	6.30	6.30
1.00		5.72	5.75	6.50	6.50
		d_zLiSe(3*)	d_zLiSe(4*)	dLiSe(3*)	dLiSe(4*)
0.06		2.96	2.96	4.85	4.85
0.11		3.02	3.02	4.89	4.89
0.25		3.04	3.06	4.89	4.91
0.33	octahedral	3.12	3.08	4.94	4.92
	bridge	3.63	2.85	4.18	4.43
	tetrahedral	4.42	2.16	4.42	4.49
0.50		3.13	3.15	4.94	4.95
1.00		3.20	3.30	4.98	4.98
		Δd_zSe(3,3*)	Δd_zSe(4,4*)	Δd_zTi(2,2*)	Δd_zTi(5,5*)
0.06		0.06	-0.06	0.08	-0.08
0.11		0.04	-0.03	0.08	-0.07
0.25		0.01	-0.01	0.01	-0.01
0.33	octahedral	0.00	0.00	0.00	-0.00
	bridge	0.22	0.07	-0.02	0.15
	tetrahedral	0.22	0.00	0.00	0.00
0.50		0.01	-0.01	0.02	-0.02

Table 4.9: Structural parameters (in a_B) for Li_xTiSe_2, with $0.06 \leq x \leq 1.0$, Li in the octahedral sites (for x = 0.33, also in bridge and tetrahedral sites are given). (upperblock) Width lengths of $TiSe_2$ layers and van der Waals gap; (middle) distance in z-direction from Li to Se atoms and Li-Se bond lengths; (lowerblock) buckling in z between atoms in the same plane. The atoms are indicated by Se, Ti, and Li (with corresponding atomic plane in parenthesis), the asterisks indicate atoms that form bondings with Li. See Figure (4.18).

x	E_{ads} (eV)	Li_xTiSe_2 $\Delta\Phi$ (eV)	μ (Debye)
0.06	-3.91	-0.4	-0.38
0.11	-3.81	-0.4	-0.35
0.25	-3.48	-0.5	-0.18
0.33	-3.58	-0.5	-0.18
0.50	-3.38	-0.6	-0.10
1.00	-3.35	-0.6	-0.05

Table 4.10: van der Waals gap: adsorption energy, change in work function, and dipole moment as a function of x .

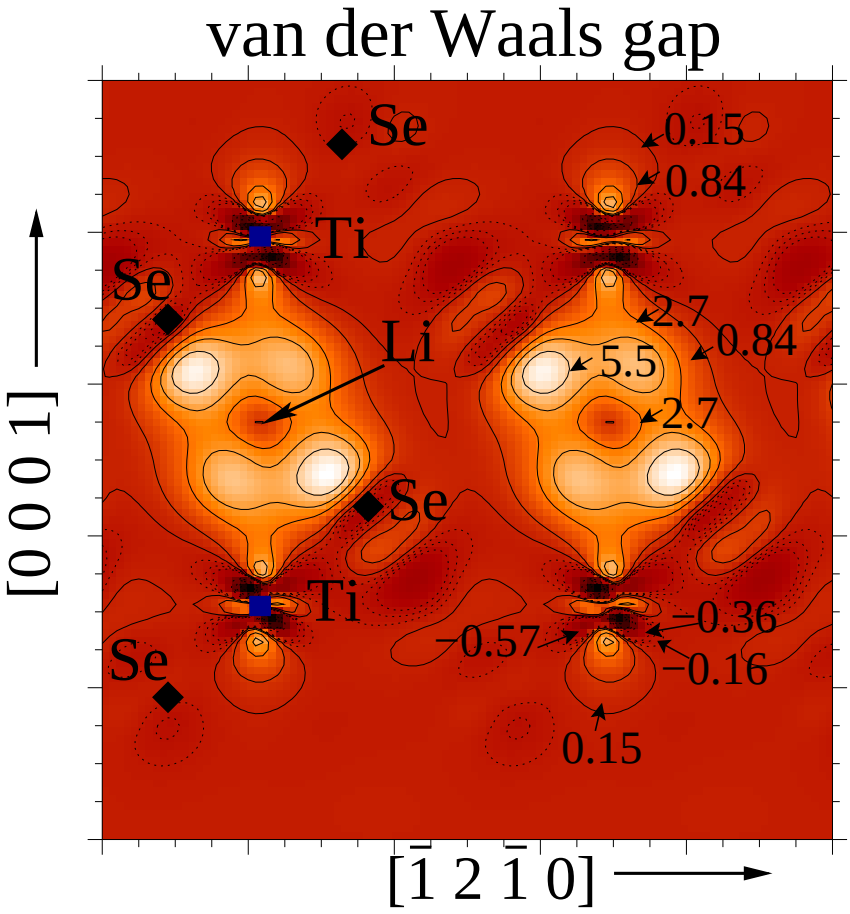

Figure 4.21: Contour plot of the electron difference density for Li at the octahedral site localized in the van der Waals gap. Diamonds denote Se- and squares Ti-atoms. The position of Li atom is indicated by the arrow. contour units are 10^{-3} $a_B{}^{-3}$.

The intercalation of Li in TMDC's has been considered to be topotactic, i.e., the host structure undergoes no distortion by insertion of the alkali [2]. Appart from a slight expansion of the c-axis, no change within the slabs is expected. In order to study the effects of alkali intercalation on TMDC's, many bandstructure calculations have been carried out in the past [49, 95, 96]. In these calculations, experimental lattice constants have been chosen to describe the intercalated compounds, and no structure optimization has been done. The *z* internal structure parameter, which determines the distances between atomic planes has been fixed to the value of the pure bulk structure. Thus, there is a lack of information about the geometric structure changes of alkali intercalated TMDC's in the near-surface region.

As described before, in the present study a structure optimization for Li_xTiSe_2 ($0.06 \leq x \leq 1.00$) has been done, with the following results. In Figure (4.18) the geometric structure of Li_xTiSe_2, with x = 0.06 is displayed, where the atoms and the distances between layers are labelled in order to facilitate their description. Additionally, in Table 4.9 are summarized the structural parameter changes of Li_xTiSe_2 , with $0.06 \leq x \leq 1.0$. As expected the greatest change produced by intercalation is the expansion of the c-lattice, with respect to the pure structure. The slabs' thickness is not significantly altered with the insertion of Li_x (for any x), in agreement with [97], but the van der Waals gap width is changed relative to the clean surface by 2, -2, -1, 0, 2, and 5 % for x= 0.06, 0.11, 0.25, 0.33, 0.5, 1.0, respectively. As it can be noted, for a very low amount of alkali (x=0.06), the gap opens locally by 0.16 a_B, with respect to the clean structure. With increasing intercalation ($0.11 \leq x \leq 0.25$) the gap contracted by about 0.08 a_B, and for x= 0.33, 0.5, and 1.00 it expands by 0.01, 0.08 and 0.33 a_B, respectively.

The Se atoms that form bondings with Li atoms and the Ti atoms that lie above and below these intercalated atoms, shift slightly away from them in z-direction, with respect to the atoms in the same plane, see Δd_zSe(3,3*), Δd_zSe(4,4*), Δd_zTi(5,5*), and Δd_zTi(2,2*) in Table 4.9. These local distortions obtained around the intercalated alkali are isolated at low x, but overlap for x>0.25 to give flat host layers. Fischer *et al.* [98] obtained that the distortion overlap for TiS_2 due to Li intercalation occurs at a lower value of x (x=0.5) than in graphite (x=0.7), thus showing that TiS_2 layers are stiffer than graphite.

The Se-Ti bonds formed by the atoms surrounding the Li intercalated atoms, Ti(2)-Se(3) and Se(3)-Ti(4), are slightly elongated by about 0.06 a_B, whereas Se(1)-Ti(2) and Ti(4)-Se(5) are contracted by about 0.04 a_B.

In Figure (4.20) (left picture) the change in work function versus x is shown. I obtained that the work function decreases smoothly and no minima are observed, in agreement with many experimental results [13, 76, 99, 100, 101].

In Figure (4.21) the difference of density charge $n^{\Delta}(\mathbf{r})$ plot shows a symmetrical distribution of the charge density in both layers separated by the van der Waals gap, where the Li atom is placed. There is an accumulation of charge between Se atoms and Li. But the maximum charge density is located in the positions of the Ti orbitals. Charge transfer to the chalcogen was also found by Umrigar, *et al.* [49] in their

FLAPW calculations on $LiTiS_2$.

4.7 Conclusions

By means of density functional theory, I have investigated the energetics of alkali metal diffusion on the $TiSe_2$ (0001) surface and along the van der Waals gap. A diffusion mechanism is proposed that involves jumps of the guest species between next-nearest sites, in both surface and gap.

Many differences are found between adsorption on the surface and in the van der Waals gap. On the $TiSe_2$ (0001) surface there are two three-fold coordinated adorption sites (hcp- and fcc-site), with the hcp slightly energetically preferred over the fcc. This energy difference becomes smaller with increasing alkali atomic radius. Both equilibrium sites are connected by a transition site, which energy difference with the hcp's energy determines the diffusion barrier value. I found that the energy barriers for alkali metal diffusion range from 0.26 eV for Li to 0.01 eV for Cs.

In the other hand, in the van der Waals gap exist three equilibrium sites per unit cell, one octahedral and two tetrahedral sites, with a strong preference for the octahedral site, which has a binding energy 0.55 eV deeper than at the hcp on-surface site. The migration of the Li atoms can be described as a hopping between octahedral and tetrahedral sites with a barrier of 0.42 eV.

With increasing amount of alkali metal the binding energies on the surface and in the van der Waals gap have similar behaviour but with a difference of 0.33 to 0.80 eV, in favour of the intercalated structure (for all concentrations). According to these results the most stable structure is obtained when Li occupies the octahedral site in the van der Waals gap, with a concentration of x=0.33, and the formation of an ordered $\sqrt{3} \times \sqrt{3}$ superstructure.

For both surface and van der Waals alkali adsorption, I found a charge transfer from the alkali to the substrate. Thus, the charge transfer takes place already on the surface and can not be the driving force for intercalation as it is often assumed [102]. The charge is located between Li and Se atoms, as well as in the *d* orbitals of Ti.

The covalent Ti-Se bond is weakened by adsorption and intercalation of Li, since for both cases a small elongation of the Se-Ti bond length is obtained.

When Li_x ($0.06 \leq x \leq 1.0$) is adsorbed on the surface the *c* lattice constant decreases by about 0.1-0.4 a_B, which yields a decrease in the van der Waals gap length. On the contrary when Li is placed in the van der Waals gap, the *c* lattice constant is expanded for larger concentrations.

When Li atoms are adsorbed on the surface, the changes of the work function can be well described by the Langmuir-Gurney model; at low coverages Φ decreases until it reaches a minimum around Θ=0.5 ML, and then increases approaching the value of the bulk alkali metal. On intercalating substrates, the work function has a smooth decrease and no minima are observed.

Chapter 5

Alkali Metal Intercalation of TMDCs

5.1 Introduction

The first structural studies of alkali intercalated TMDCs have been carried out on samples intercalated e.g. by direct synthesis [103], by inmersion of crystals in a solution of the metal (alkali metal in liquid ammonia, butyllithium, sodium naphthalide) [104, 105, 106], and by electrochemical process (with the host acting as cathode, an alkali metal salt in a non-aqueous solvent as electrolyte, and the alkali metal acting as anode). In these methods the small size of the powder specimens used, allows the homogeneous intercalation of the guest material, but limits a complete understanding of the intercalation mechanism. It has been observed that when cleaved, the resulting alkali intercalated TMDCs surfaces are not appropiate for surface studies.

Recently, the possibility to form high-quality surfaces of intercalated materials by deposition of alkali or noble metals onto TMDCs surfaces has been demonstrated [13, 14, 15, 16]. In this method the intercalant is deposited *in situ* on the TMDCs surface under UHV conditions, from where it "spontaneously" intercalates, after an initial adsorption stage. This intercalation method has shown to be advantageous against the above mentioned, since it gives the possibility to study the samples in every step of the reaction by means of surface science techniques. For example, the evolution of TMDCs electronic structure during the intercalation process can be directly investigated by angle-resolved photoemission spectroscopy.

In the literature exists a large list of reports verifying *in situ* alkali intercalation on TMDCs. For instance, based on core-level spectroscopy Brauer [19] have demonstrated that when Na, K and Cs are deposited on TiS_2, they all intercalated into the van der Waals gaps. In contrast to this, recent studies employing scanning tunneling microscopy combined with angle-resolved photoemission spectroscopy have revealed the formation of networks of metallic nanowires on the (0001) TMDCs surface, after Rb deposition [17, 18].

These studies have provided much new information about the interaction between alkali metal and TMDCs, but at the same time they have given rise to many questions

regarding the *in situ* intercalation process, and the induced structural changes. In particular, it is important to know which factors enhance or inhibit intercalation. On this point, it has been argued that surface defects play an important role for alkali diffusion towards the interior of the crystal [107].

In the previous Chapter, the energetically favorable on-surface adsorption sites as well as the intercalation sites were fully described. It has been demostrated that the Li atoms are more stable intercalated rather than adsorbed. After this result the question that naturally arises is how the alkali atom diffuses from the free-defect surface towards the van der Waals gap. In the present Chapter the attention is focused on simulating structural and energy changes during the process of lithium diffusion within $TiSe_2$ interlayer spacing, in order to get insight into the most favoured mobility paths of the alkali atom, and to estimate the corresponding activation energies.

5.2 Model and Computational Details

Total energy calculations within the *ab-initio* pseudopotential plane-wave formalism had proved to be a reliable tool for describing the diffusion trajectory of alkali ions through crystalline structures [108]. Therefore, this method was applied to determine Li's energetically favorable path of intercalation within $TiSe_2$ atomic planes. The total energies of several configurations were computed, where Li position was varied in the space between the $TiSe_2$ (0001) surface and the van der Waals gap.

Since this path will connect the equilibrium sites of both the surface and the van der Waals gap, the supercell used to determine them (see Sec. (4.2)), was also employed in the present calculations, i.e., a $\sqrt{3} \times \sqrt{3}$ surface unit cell composed by three layers of $TiSe_2$, with a total number of 9 titanium and 18 selenium atoms and a vacuum region of 8.3 Å.

The total energy was calculated for a non-uniform mesh of points. In *z*-direction the distance between the Li on-top adsorption surface site and the middle of the van der Waals gap was divided into 12 planes. On each plane the most stable position of the Li atom was determined by keeping one of its coordinates fixed (in the *z* axis), and allowing the other two (*x* and *y*) to relax. The Ti atoms' *z* coordinate were kept fixed in order to maintain the Li atom between the atomic-planes, otherwise the structure would be completely shifted in *z*-direction to have the Li atom placed on the surface. For every Li position, the Se atoms in the first two sandwiches were allowed to relax without constraints. Because of the crystal symmetry, it was only necessary to calculate the total energy for configurations with Li positioned in the irreducible part of the supercell, i.e. in the triangle formed by the projections of two Se atoms (in the first and third atomic-plane) and one Ti atom (in the second plane). This can be seen in Figure (5.1) where the irreducible part of the first layer of the supercell is shown.

The points with minimum energy on each plane were considered to form the intercalation path. To check the continuity of this path the total energy of some intermediate points was also computed. The path with the lowest diffusion barrier was chosen to

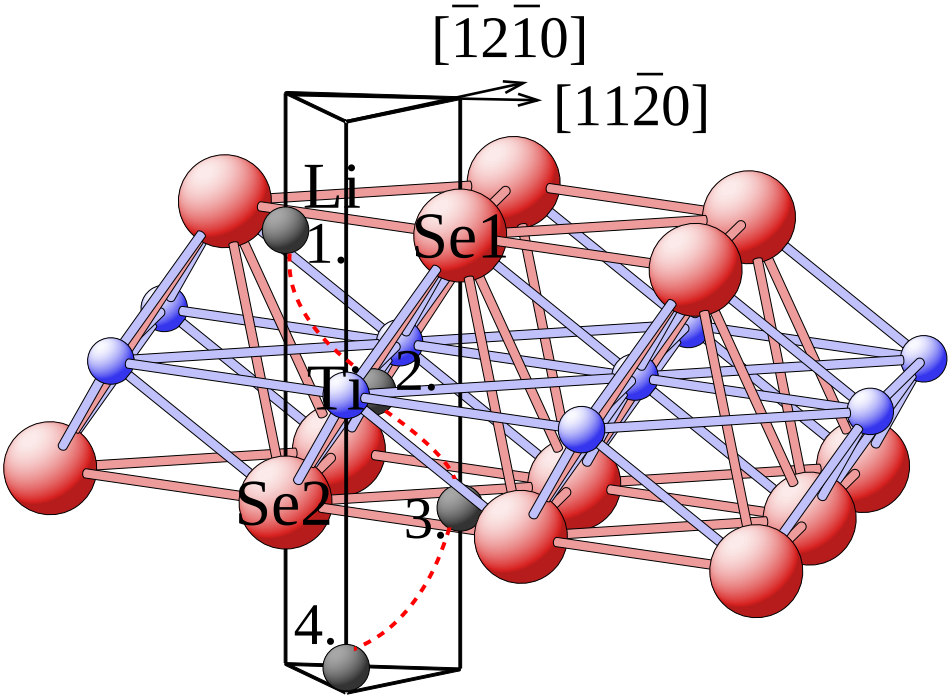

Figure 5.1: Irreducible part of the first layer of $TiSe_2$ (0001) surface limited by the triangular prism, where the total energy calculations were carried out to find the energetically favorable intercalation path. The gray spheres describe Li-atom's pathway through the atomic layers.

be the optimum one, and the diffusion barrier, E_d, was calculated as $E_d = E_{sad} - E_{min}$ where E_{sad} and E_{min} are the total energies of the system with the adatom at the saddle point and at the equilibrium adsorption site, respectively.

5.3 Results and Discussion

5.3.1 *Ab* -surface intercalation pathway

The alkali metal intercalation path I am searching for, has to begin on the (0001) free-defect surface, continue through the atomic-planes, and end in the van der Waals gap of $TiSe_2$. From all investigated paths the one shown schematically in Figure (5.1) represents the path with the lowest energy barrier. The gray spheres denoted the Li positions on each atomic-plane. This path (brocken red line) starts at a point located in the first Se atomic-plane directly below the fcc surface site, and continues entirely

within the single plane perpendicular to the layers containing the starting point, two Se atoms, and one Ti atom.

The total energy contour-plot and surface for Li atom displacement are presented in Figures (5.2) and (5.3) respectively. The energy zero of these graphics corresponds to the energy of the hcp adsorption surface site (-3.58 eV). In both graphics the atomic positions of the clean substrate are indicated by the element symbols. The *y*-axis is parallel to the $[11\bar{2}0]$ vector and z-axis normal to the (0001) surface.

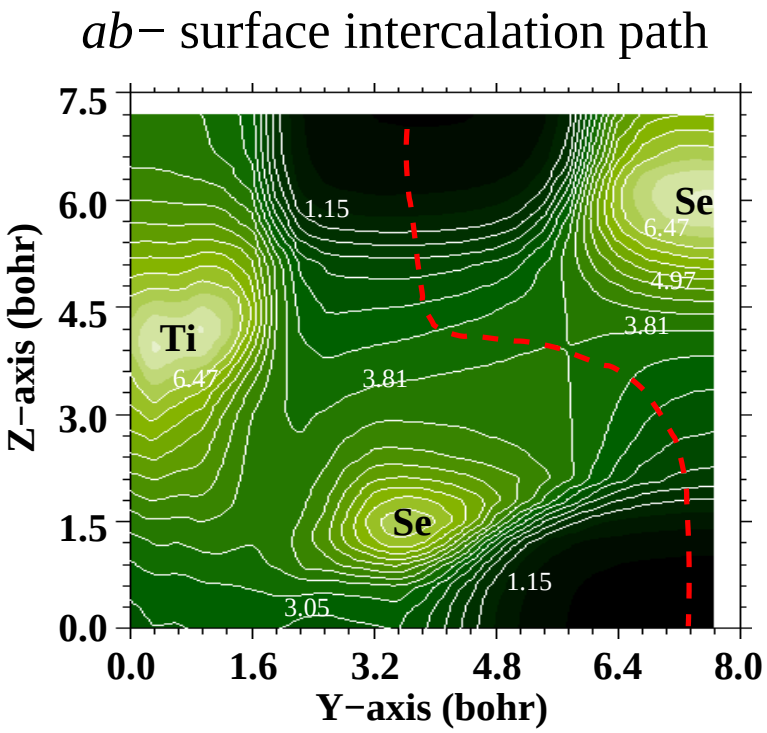

Figure 5.2: Contour plot of total energy in intercalation plane comprising Se atom of the first, Ti of the second, and Se of the third atomic-plane. The y-axis is parallel to the $[11\bar{2}0]$ vector and z-axis normal to the (0001) surface. Energy zero corresponds to the hcp surface adsorption site located at $z = 9.15$ a_B; center of van der Waals gap at $z = -1.7$ a_B; contour-line spacing 0.38 eV. The dashed red line indicates the energetically favorable intercalation path.

From the results presented in the previous Chapter, there are two possible on-surface sites from where the alkali metal atom can reach the first atomic-plane of the substrate, namely the hcp and fcc sites. The hcp site has a higher adsorption energy than the fcc site, yet the Li adatom is adsorbed closer to the substrate atomic-planes at the fcc, i.e., the distance from the Li to the first Se-plane is 2.23, and 2.48 a_B at the fcc- and hcp-site, respectively.

The reason for the larger Li adsorption distance at the hcp site is its proximity with the Ti atom, which is located below this site in the second atomic-plane. The stong electrostatic repulsion between Li and Ti atoms is better screened at the fcc site, allowing the Li atoms to come closer to the surface.

From any of these two adsorption sites it is evident that the Li atom experiences an energy barrier as it approches the Se plane, increasing stronger from the hcp site. Thus, the path will begin at the fcc-site and run vertically towards bulk, always accompanied by an increase in the total energy of the system. As it can be seen in Figure (5.2), the energy has already increased by 1.15 eV, when the Li was just localized in the first atomic-plane. When the alkali atom is 0.3 a_B above the second atomic-plane (Ti), its closeness with the Se atom in the third atomic-plane 3.4 a_B, and the distortion of the lattice due to the large displacement in *z*-axis of this Se atom (0.8 a_B towards bulk), forced it to change direction towards an unnocuppied site, e.g., to the on-top site projection in the third atomic-plane (Li in the third position of Figure (5.1)). To achieve it the Li atom has to cross between two Ti atoms, forcing them to increase their distance to a maximum value. Consequently the total energy of the system reaches its maximum value of 3.81 eV.

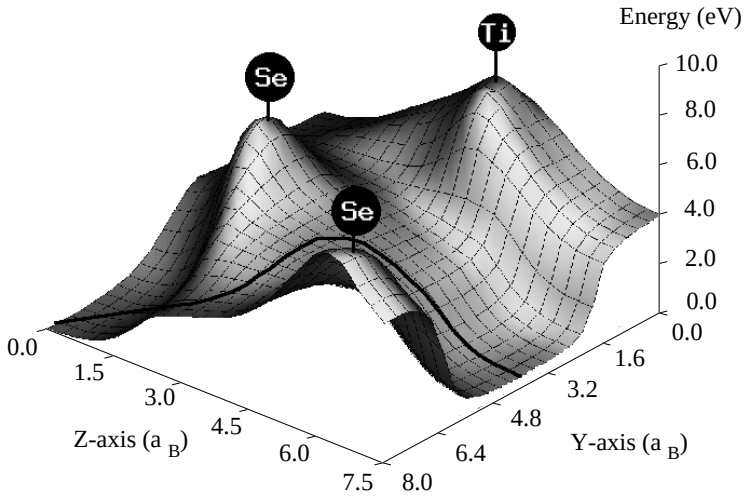

Figure 5.3: Intercalation energy surface with respect to the position of the intercalant in the intercalation plane; intercalation path denoted by solid line. The y-axis is parallel to the $[11\bar{2}0]$ vector and z-axis normal to the (0001) surface. Energy zero corresponds to the hcp surface adsorption site located at $z = 9.15$ a_B; center of van der Waals gap at $z = -1.7$ a_B.

Once the Li has moved from this saddle point, the energy begins to decrease as the Li moves towards the tetrahedral site in the van der Waals gap with an energy of -0.19 eV, already well below its minimum energy when adsorbed at the surface. From this position Li moves to the octahedral site close to the middle plane of the gap, which

exhibits its lowest energy of -0.55 eV. This last step experiences a slight energy barrier of 0.06 eV. The reverse moving (octahedral → bridge → tetrahedral) would thus meet a barrier of 0.42 eV showing the stability of the octahedral intercalation site in the van der Waals gap.

In the literature mainly direct intercalation and intercalation via defects are considered. Especially, Li generally was thought to be a candidate for direct intercalation because of its small size. Our calculations show that even this material has a far too high energy barrier for direct intercalation being possible.

5.3.2 Geometrical changes

To get insight into the substrate geometrical changes induced by the presence of the alkali, additional calculations were done. Four points in the pathway were chosen, see Figure (5.1).

The first three points are situated in the same plane of the atoms constituing the substrate, and the fourth of them at the van der Waals gap equilibrium site. At each plane, the relaxation of the atoms forming it have been constrained to the x-y plane, in order to estimate the expansion of the *a*-lattice constant due to the insertion of the alkali atom.

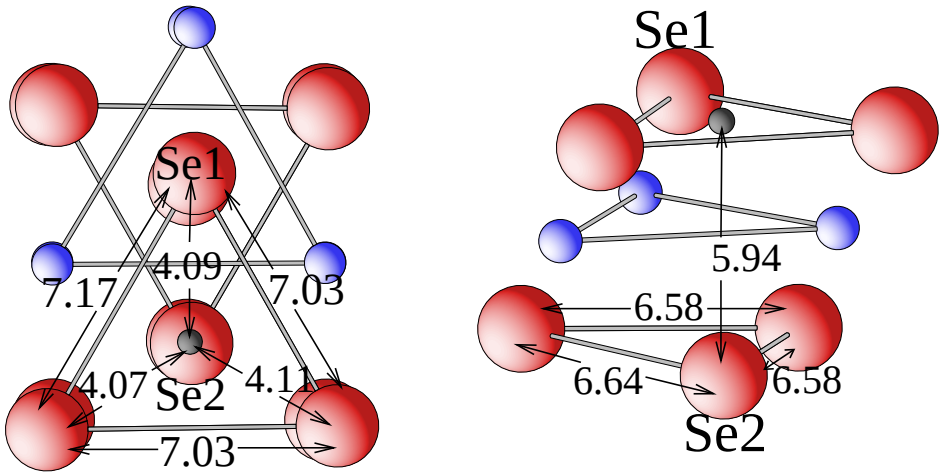

Figure 5.4: Top and side view of the geometrical changes induced by the insertion of Li. The Li is positioned in the first atomic-plane, in the projection of the on-surface fcc adsorption site. Units are in a_B.

As it can be seen in Figure (5.4), when the Li atom is in the first atomic-plane (Se), below the fcc on-surface adsorption site, the Se-atoms move radially away from the Li atom by about 0.30 a_B from their original position, increasing their separation from 6.60 a_B to 7.03, 7.03, and 7.17 a_B. The Li-Se bonds have a length of 4.09, 4.07, and 4.11 a_B. The Se atoms in the third plane are slightly taken away from their equilibrium position. Only one of them is shifted 0.26 a_B vertically in the surface direction, changing the distance between the Se atoms by 6.64, 6.58, and 6.58 a_B. The distance between Ti atoms is changed to 6.65, 6.55, and 6.60 a_B.

In the next point, see Figure (5.5), when the Li atom is in the Ti atomic-plane, a notoriously large displacement of 0.98 a_B for two of the Ti atoms, away from the Li, is obtained. The strong repulsion between Ti and Li atoms forced them to keep a minimum distance of 4.28 a_B, leading to an expansion in the Ti-Ti separation from 6.60 a_B to 8.57, 7.21, 7.21 a_B. This position is found to be the saddle point of the surface energy, with a value of 3.81 eV.

Due to the symmetry of the slab, the geometrical changes with Li in the third atomic-plane are similar to the ones with Li in the first atomic-plane.

5.4 Conclusions

I have determined the energetically minimal path of intercalation for Li, with the result of an activation barrier of 3.81 eV, which excludes this type of intercalation. The analysis done to determine this path revealed that the strong repulsion between Ti- and the Li- atoms, and the consequent lattice deformation, give rise to the high diffusion barrier encountered.

To resume, the intercalation pathway found is constituted of the following steps:

1. Li attains the first Se atomic-plane via the fcc surface site with a cost of 1.15 eV.

2. It moves to a bridge position between two Ti ions at the second atomic-plane with a cost of 3.81 eV.

3. It goes to the third atomic-plane, to the projection of the on-top adsorption site, i.e., below the Se atom of the first atomic-plane, and reach the tetrahedral site in the van der Waals gap with an energy gain of 0.19 eV.

4. It finishes intercalation via a bridge position symmetric to that at the surface by reaching the octahedral hole made of six Se ions surrounding the van der Waals gap with an energy gain of 0.55 eV.

Here the energies are given with respect to the hcp's site adsorption energy.

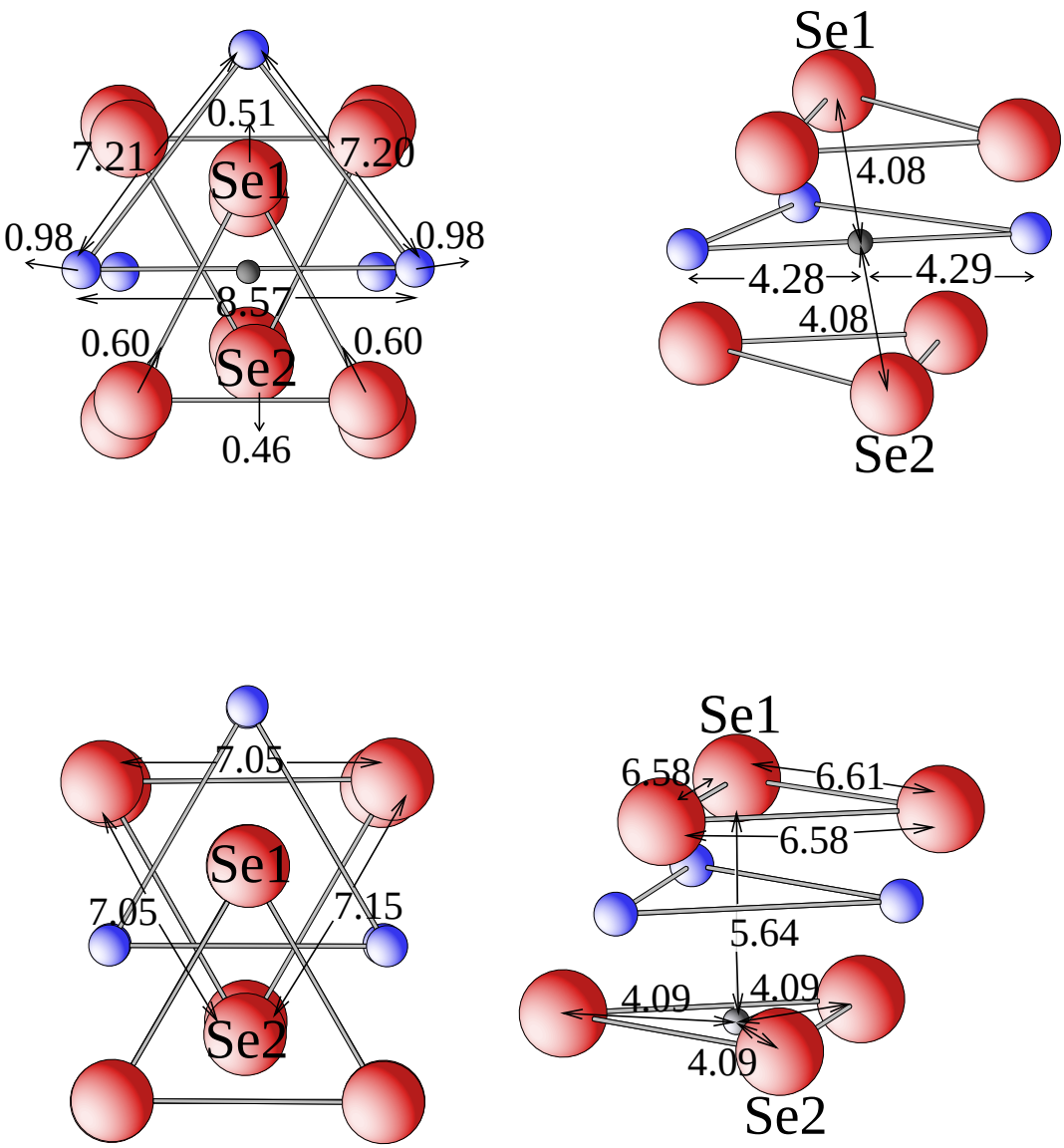

Figure 5.5: Top and side view of the geometrical changes induced by the insertion of Li. (upper) Li atom is positioned in the second-, and (lower) third- atomic-plane. Units are in a_B.

Chapter 6

Adsorption and Diffusion of Alkali metal on TMDCs Steps

6.1 Introduction

The details of alkali intercalation into transition metal dichalcogenides represent an unsolved problem to date. According to the results described in the former Chapter, alkali intercalation is difficult for atoms starting from a clean $TiSe_2$ (0001) surface into the van der Waals gap. However, it seems to be possible from a step edge or into a surface fissure in order to explain the easy intercalation found in the liquid phase and in various growth techniques. Especially, from stereochemistry the intercalation of the heavier alkali atoms looks rather improbable at a defect free surface. The recently observed intercalation via wire-like fissures in the surface [18] shows a possible path for this process. The STM experiments [109] favor mainly the two steps here considered.

Employing total-energy density-functional theory calculations the adsorption energies, the diffusion pathways and barriers for a Li adatom on stepped $TiSe_2$ surfaces with full relaxation of the atomic environment were studied.

The minimum path for Li diffusion on $TiSe_2$ (0001) surface and across the $(10\bar{1}0)$ and $(\bar{1}2\bar{1}1)$ steps have been calculated. To approach the $(\bar{1}2\bar{1}1)$ step edge an Ehrlich-Schwoebel barrier of 0.31 eV was obtained, which is additional to the diffusion barrier of 0.25 eV on the flat surface. The energies for subsequent diffusion within the van der Waals gap have been calculated, too.

In Figure (6.1) the $(10\bar{1}0)$ and $(\bar{1}2\bar{1}1)$ step orientations are shown.

6.2 $TiSe_2$ (0001) surface with a $(10\bar{1}0)$ step

6.2.1 Simulation of a $(10\bar{1}0)$ $TiSe_2$ oriented step

In the present calculations the local density approximation for the exchange-correlation functional and separable *ab initio* pseudopotentials are used. The adsorption and dif-

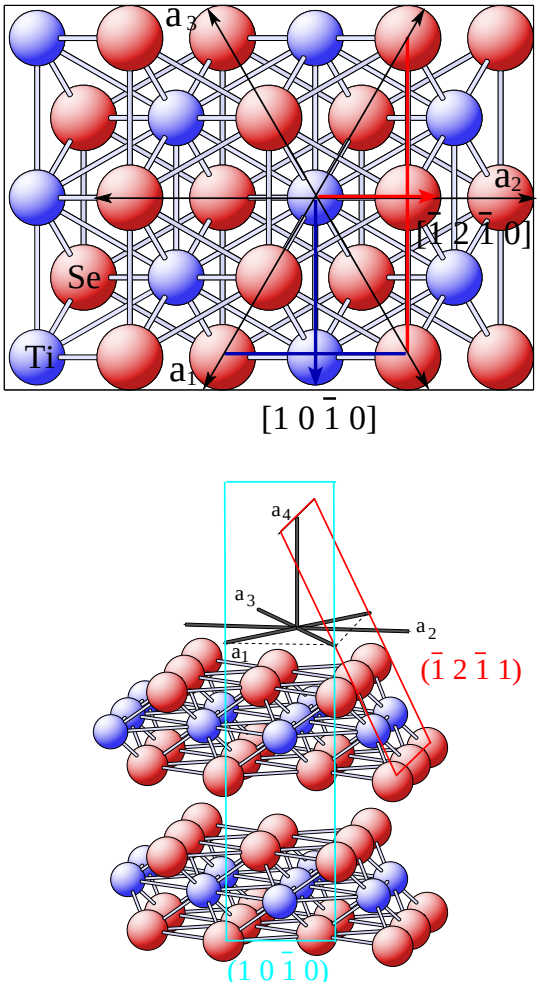

Figure 6.1: (top) View of $TiSe_2$ (0001) surface with the $[10\bar{1}0]$ and $[\bar{1}2\bar{1}0]$ directions indicated. (left) The $(10\bar{1}0)$ and $(\bar{1}2\bar{1}1)$ step orientations. Red and blue spheres represent Se and Ti atoms respectively.

fusion of an isolated adatom on an infinite crystal is modeled by using a slab in a supercell, formed by two layers of $TiSe_2$, with at least 17 a_B of vacuum spacing, where the adatom is adsorbed on one side only.. Each layer of $TiSe_2$ is composed of 12 Ti- and 24 Se-atoms, i.e. of 12 $TiSe_2$ unit cells (Se-Ti-Se). When comparing it with the energy of a layer with 14 $TiSe_2$ unit cells, the difference per unit cell was of 0.01 eV. To model the $(10\bar{1}0)$ $TiSe_2$ step one third of the atoms in the first layer is removed, leaving a total of 20 Ti and 40 Se atoms altogether. In Figure (6.2) the schematic representation of the supercell used to simulate this step is shown. The unit cell, enclosed by the solid square, is repeated periodically in *x*, *y*, and *z* directions. As it can be seen in Figure (6.2) the atoms forming the step are separated from the next cell by 19.8 a_B, thus, a Li adatom at this step can be considered isolated. Also, from the calculations of Li diffusion presented in Sec. (6.2.3), the number of atoms in the first layer is enough to simulate the $TiSe_2$ (0001) surface. The lattice constants used are the theoretical val-

ues obtained for bulk $TiSe_2$ fully intercalated with Li, $a = 6.61$ a_B and $c = 11.90$ a_B, (see Table 3.2). The electron eigenfunctions are expanded in a plane-wave basis using a cutoff of 40 Ry with two special **k** points in the surface Brillouin zone [81].

In order to study the structural changes of the stepped (0 0 0 1) surface a geometry optimization was carried out. The atomic positions of all atoms in the first layer and the first atomic plane (Se atoms) of the second layer were allowed to relax. While the rest two atomic planes (Ti and Se atoms) of the second layer were fixed in their bulk positons.

For studying the adsorption and diffusion of Li at this system the total energy of the Li placed on the symmetrical points of the (0001) surface was calculated, as well as on the edge of the $(10\bar{1}0)$ step and across it, with relaxation of the enviroment. The height of the step in this material is about 9 bohr, which is the thickness of one layer of $TiSe_2$ together with the van der Waals gap. When calculating the adsorption energy of Li on each symetrical point (hcp and fcc sites), first the *z* coordinate was optimized, while the *x* and *y* coordinates of the adatom were kept fixed. Once this was done, the *x* and *y* adatom coordinates were also allowed to relaxed, to obtain the absolute position of the adsorption sites, and finally the barrier sites between them were found.

6.2.2 Relaxation of the $TiSe_2$ (0001) surface with a $(10\bar{1}0)$ step

When the geometry of the $TiSe_2$ (0001) surface with a $(10\bar{1}0)$ step was optimized, it was obtained that only the position of the atoms (in the first layer) located near the step edge changed with respect to the geometry of the $TiSe_2$ (0001) surface. In Figure (6.2) these atoms are enclosed in a dashed square, which is enlarged in Figure (6.3). The changes in the position of the atoms, with respect to the $TiSe_2$ (0001) flat surface (calculated with a 2×2 surface unit cell), are resumed in Table 6.1. The selenium atoms (1 and 2), are moved closer in the *z* direction, reducing their distance from 6.88 a_B to 6.58 a_B, while the Ti (1) is displaced towards Ti (3) changing their bond length from 6.61 a_B (the lattice constant value) to 5.86 a_B. According to the results of Table 6.1 only the Se (1,2,5,6) and Ti (1,2) atoms changed their positions as a consequence of the missing neighboring bonds originated from the step formation.

6.2.3 Li diffusion across and along $TiSe_2$ $(10\bar{1}0)$ step

From all possible Li adatom diffusion pathways that were found, the one illustrated in Figure (6.4), represents the energetically minimal diffusion path. Top views of this diffusion path at the (0001) surface and across the $(10\bar{1}0)$ step (top picture) and along the van der Waals gap (lower picture) are presented in Figure (6.5). The points in the surface and in the van der Waals gap are labeled by s_i and g_i, respectively. The diffusion path starts at the point s_0, which is an fcc adsorption site in the surface. From this point the adatom hops to a bridge site s_1 situated between two atop sites (above Se positioned in the first layer), to continue to the *hcp* site s_2. The energy value

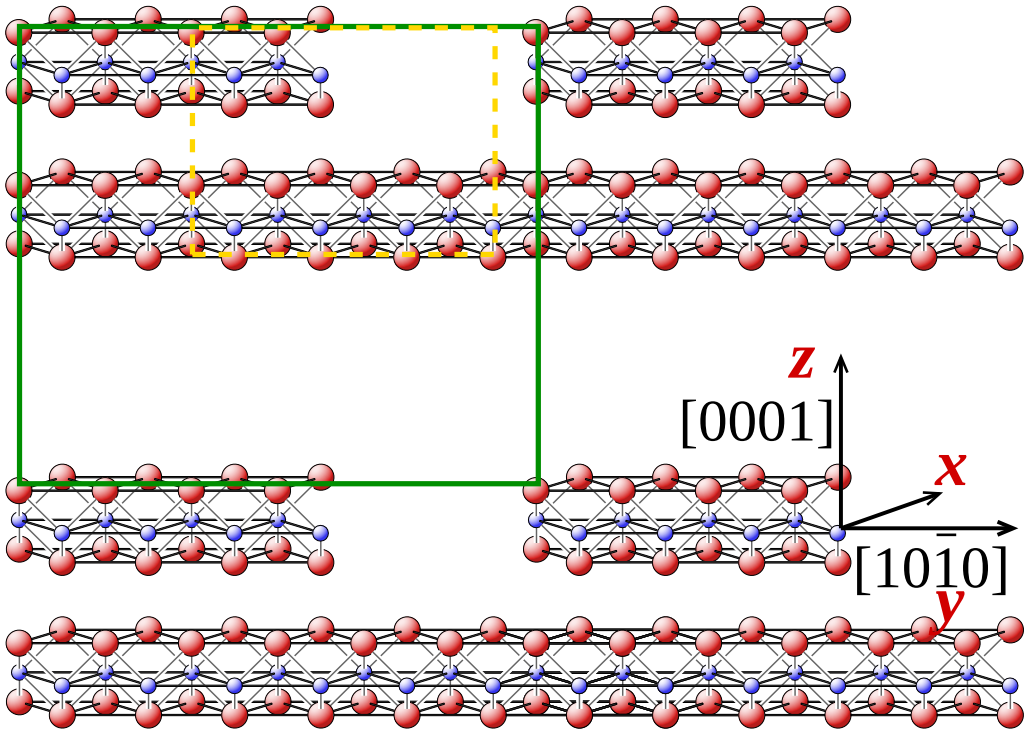

Figure 6.2: Supercell used to model the (0001) $TiSe_2$ surface with a $(10\bar{1}0)$ step. The solid square enclose the unit cell, which is repeated periodically in the *x*, *y*, and *z* directions. The dashed square indicates the part of the unit cell where the most significant structural changes take place.

at the latter position is taken as the zero energy reference, see Figure (6.6) (top picture).

The adatom continues hopping to another bridge site s_3 from where it reaches s_4, an fcc site located in the edge of the step. In the absence of a step the adatom would continue diffusing along the (0001) surface in complete agreement with the diffusion path previously studied (see, Secc. 4.4), ($fcc \rightarrow bridge \rightarrow hcp \rightarrow bridge \rightarrow fcc$ ...). Moreover, the values for the diffusion barriers on the (0001) surface that were found in the present study, [0.23 and 0.25 eV, see Figure (6.6) (top)], also agreed with the results presented in Chapter 4. When the Li adatom reaches the edge of the step s_4, this fcc site is no longer a minimal energy adsorption point, therefore the Li adatom continues descending to s_5, see Figure (6.6) (bottom), where it finds an adsorption site 0.10 eV deeper than an fcc site on the surface. To move forward from this adsorption site the adatom has to overcome a barrier of 0.14 eV (encountered in s_6), which is 0.10 eV lower than the diffusion barrier in the flat (0001) surface. From this point the adatom moves without further energy barrier across the step getting to g_5 site, which

is located in the van der Waals gap below Se_1, (see Figure (6.4) bottom). The Se_2 from Figure (6.4) was removed to facilitate the sight of the complete diffusion pathway, in particular of the g_5 site. Once the Li adatom attains the van der Waals gap, it diffuses along the gap without energy barrier to reach g_3, an octahedral site surrounded by six seleniums, three from each upper and lower sandwich. This octahedral site is the most energetically stable site in the van der Waals gap, with an energy of -0.57 eV with respect to the hcp site in the surface. In order to keep diffusing along the van der Waals gap, the Li adatom moves to g_0, which is a tetrahedrally coordinated intersandwich site lying inmediately below a chalcogen atom, over g_1. The latter site is 0.54 eV higher in energy than the octahedral site, and constitutes the diffusion barrier in the van der Waals gap. The adatom could diffuse in the opposite direction, from g_3 to g_6 with a significantly lower diffusion barrier of just 0.24 eV, and then without barrier to g_7, but to get away from this site, it has to overcome a barrier of about 0.70 eV.

A sequence of pictures showing the atomic positions of Li adatom along its diffusion path and the subsequent substrate structural changes are displayed in Figure (6.7). The cost of displacing a Li adatom from the *hcp* three-fold hollow (s_2) to a bridge (s_3) site is that of replacing three Li-Se bonds (4.43, 4.49, and 4.51 a_B) by two (4.3 and 4.68 a_B). On the flat surface the s_4 site would be a *fcc* three-fold hollow site,

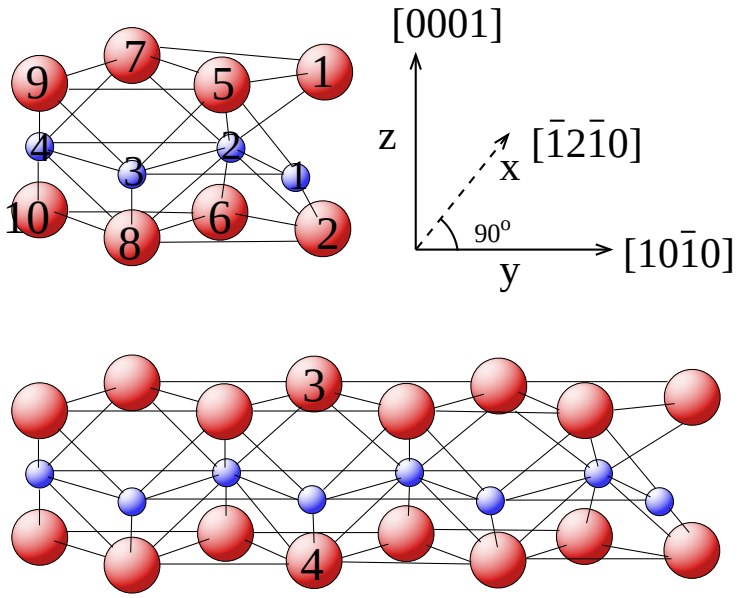

Figure 6.3: Enlarged picture of the unit cell's section indicated in Figure (6.2), where structural changes occur due to the presence of a $(10\bar{1}0)$ step. The red and blue spheres represent Se and Ti atoms, respectively. Some atoms are numbered to facilitate the description of their relaxations, (see Table 6.1).

Atom	Δ x	Δ y	Δ z
Se			
1	0.28	0.28	-0.52
2	-0.26	0.22	0.25
3	0.00	-0.02	-0.02
4	-	-	-
5	0.10	-0.08	-0.07
6	-0.08	-0.14	-0.07
7	0.01	-0.01	-0.01
8	-0.01	0.00	0.00
9	0.00	0.00	0.00
10	0.00	0.00	0.00
Ti			
1	0.01	-0.75	-0.06
2	0.01	0.24	-0.06
3	0.01	0.07	0.02
4	0.00	0.01	0.01

Table 6.1: Atomic displacements with respect to the $TiSe_2$ (0001) surface positions (in a_B). The Se and Ti indices are referred to Figure (6.3). The first layer and the first (Se) atomic plane of the second layer were allowed to relax.

where the Li would be bonded to three Se atoms. Due to the presence of the step, the adatom has to migrate deeper (to s_5) in order to form three Li-Se bonds (5.07, 4.85, and 4.44 a_B). The s_6 point is a barrier site at the edge of the step. Here the energy of the system increases, but the amount is by 0.1 eV lower than for a comparable barrier site on the flat surface. At this site (s_6) the Li adatom stills forming three Li-Se bonds (4.56, 4.21, and 5.07 a_B), one more than at an equivalent site on the flat surface. From this point moving deeper in *c* direction the Li adatom bonds with two Se, until the s_9 site, where again three Li-Se (4.58, 4.96, and 5.2 a_B) are formed. Finally, the Li adatom intercalates into the van der Waals gap and reaches site g_3, where it forms six Li-Se bonds (4.77, 4.78, 4.79, 4.89, 4.89, and 4.83 a_B).

The diffusion along the step bottom, i.e. in the $[\bar{1}2\bar{1}0]$ direction, was also calculated. In this case, the total energy of the system was calculated with Li situated at the different points presented in Figure (6.8). The *x* and *y* coordinates of the Li adatom were kept fixed, while the *z* coordinated was allowed to relaxed. The substrate was relaxed as described before. The Li adatom diffuses between both $TiSe_2$ layers (at the van der Waals gap), below the atoms forming the edge of the step. At the site (1) above the Ti(2) the Li founds an equilibrium site with an energy of -0.53 eV, and forms five Li-Se bonds (4.95 4.92 4.94 4.90 4.88 a_B). Then it moves to the site (3) (above Se(4)), where the energy is -0.48 eV and forms four Li-Se bonds (4.52, 4.68, 4.70, 4.64 a_B).

To reach this point the Li meets a barrier of 0.15 eV at the middle of both equilibrium sites (2), where the the Li adatom forms three bonds with Se atoms (4.60 4.47 4.59 a_B). The Li continues hopping to the site (5) overcoming a barrier of 0.23 eV at (4). The (5) site has an energy of -0.45 eV and forms three Li-Se bonds (4.36, 4.59, 4.52 a_B). From this site it goes again to another site equivalent to (1), (not shown in Figure (6.8) but labelled as (7) in Figure (6.9)), in this case the barrier to overcome is 0.24 eV, found at site (6). At both barrier sites (4) and (6) the Li adatom forms only bonds with two Se atoms, with have the following lengths: 4.39, 4.37 a_B and 4.36, 4.37 a_B, respectively. In Figure (6.9) are shown the corresponding energies of the path. It can be seen that to move from site (7), to (6), the barrier energy between them is 0.32 eV, i.e. 0.08 eV higher than by the reverse moving. From these results it is clear that the sites where the Li can form bonds with Se atoms are energetically favoured. The site (5) is the same as g_5 from the diffusion path along the van der Waals gap, (see Figure (6.5) bottom). At this site the Li adatom would have the possibility to diffuse within the gap to the most energetically favorable site found (octahedral), to diffuse on the lower terrace, or to move to the most stable site at the bottom of the step (1). In the first case the Li adatom diffuses with a gain 0.12 eV, in the second with a cost of 0.09 eV, and in the third also with a cost of 0.24 eV.

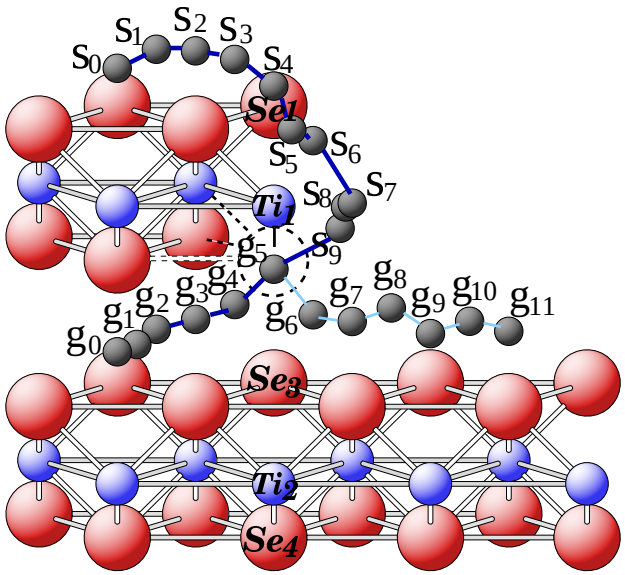

Figure 6.4: Schematic display of $TiSe_2$ $(10\bar{1}0)$ step. The Li adatom's positions during its diffusion pathway are represented by the black spheres. The adatom's positions at the (0001) surface and $TiSe_2$ $(10\bar{1}1)$ step are denoted with s_i and g_i, respectively. The position of a Se atom in the third atomic plane is indicated by the dashed circle; it was removed in order to show point g_5. The diffusion pathway is denoted by the dark blue line. The light blue line denotes an alternative diffusion path at the height of van der Waal gap.

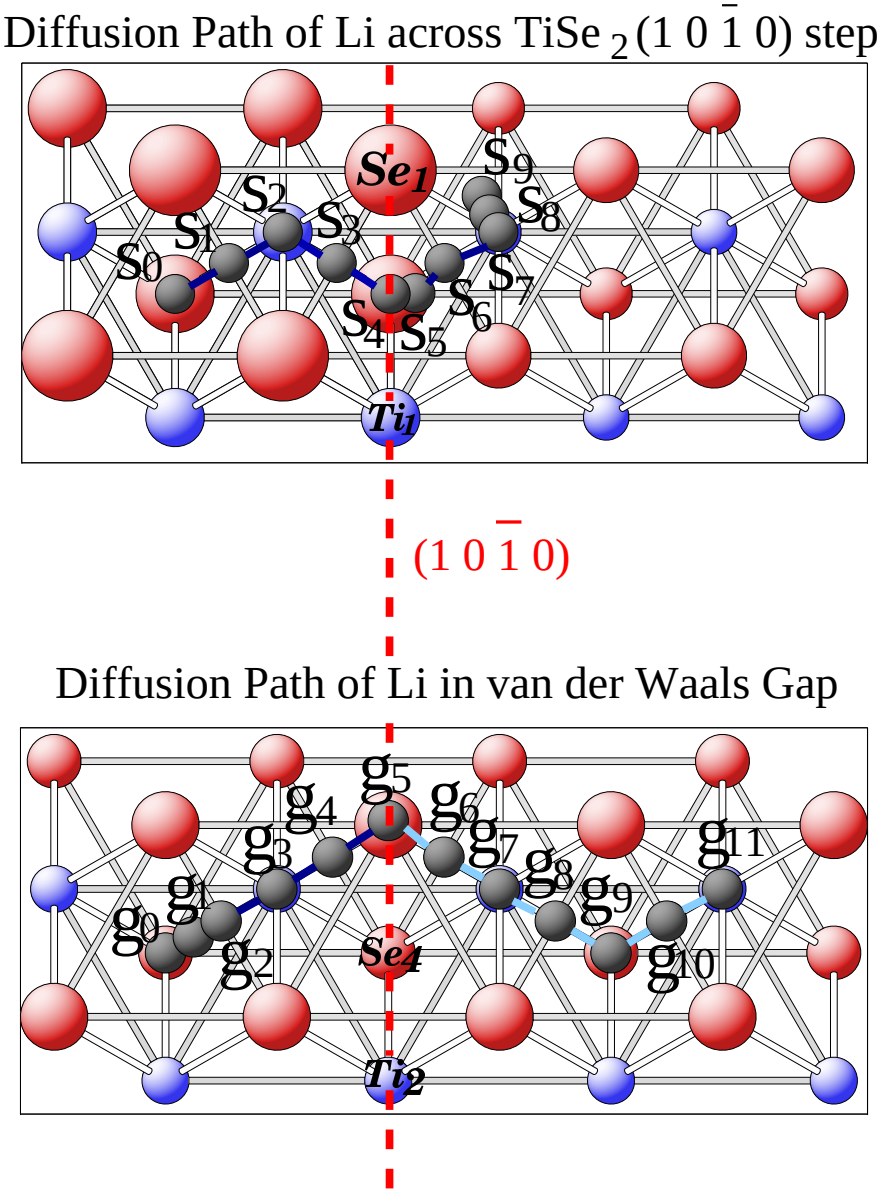

Figure 6.5: Top view of the diffusion path, (upper) across $TiSe_2$ $(10\bar{1}0)$ step and (bottom) along the van der Waals gap. The selenium and titanium atoms are denoted by red and blue spheres, respectively, whose sizes decrease according to their distance from the surface. The blacks spheres represent the Li adatom's positions. The seleniums with indices are at the surface's edge. See Figure (6.4).

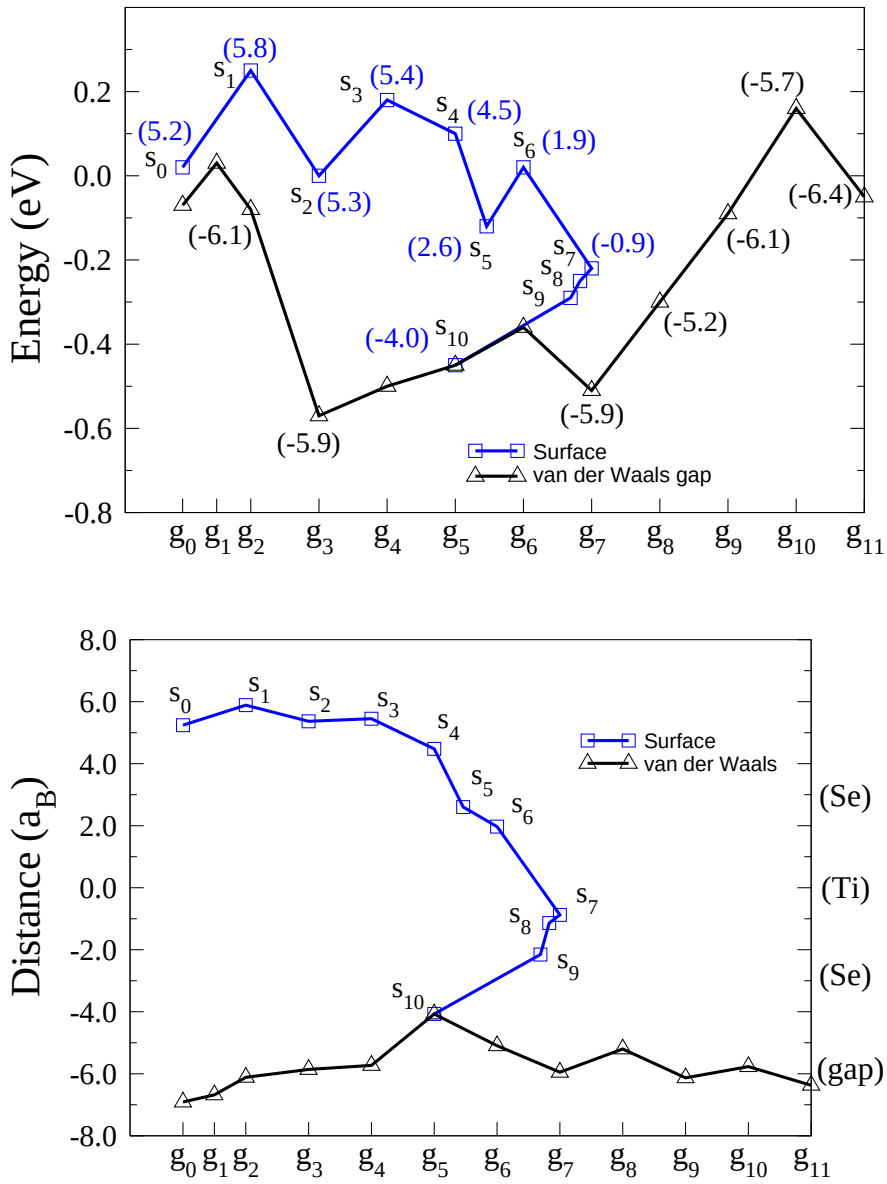

Figure 6.6: (Top) Total energy for a Li diffusing on the (0001) surface and $(10\bar{1}0)$ $TiSe_2$ step (blue line), and in the van der Waals gap (black line). The zero energy corresponds to the s_2 site, which has the minimum energy in the surface. The points on the surface and in the van der Waals gap are labeled by s_i and g_i, respectively. (bottom) The values of Li height (in a_B) with respect to the titanium atomic plane position in the first sandwich; they are enclosed in parentheses in the figure on top. The position of the selenium and titanium atomic planes in the first sandwich of $TiSe_2$ and of the van der Waals gap are marked at the right axis of the graphic.

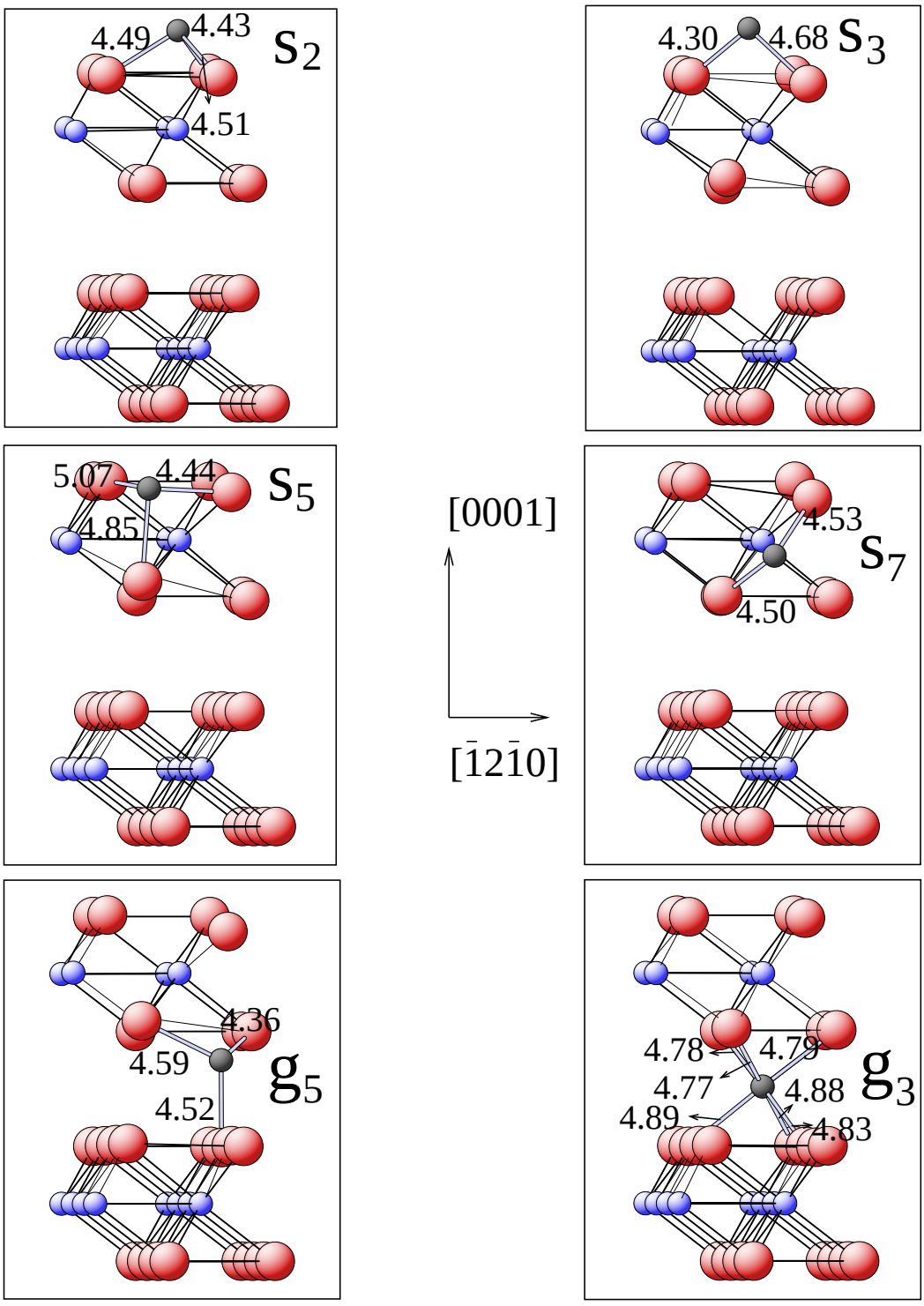

Figure 6.7: Pictures of Li adatom along (0001) $TiSe_2$ surface and $(10\bar{1}0)$ step. The Li-Se bond lengths are given in a_B. The sites are referred to Figure (6.4).

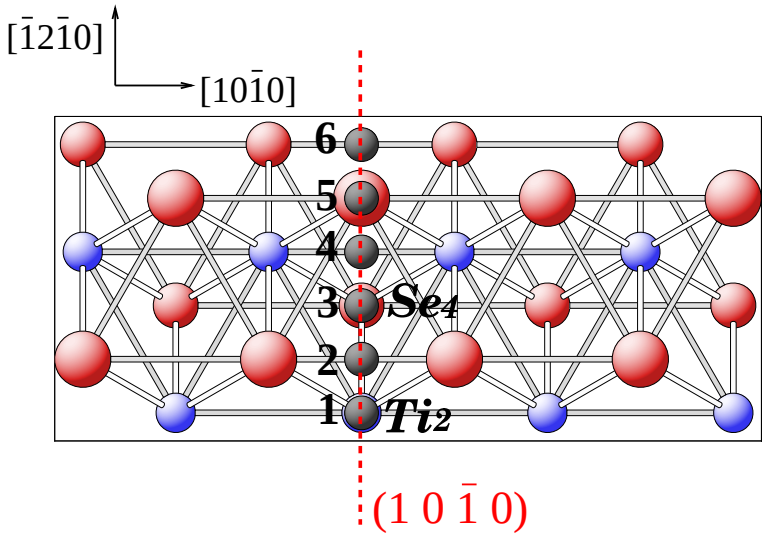

Figure 6.8: Top view of the diffusion path along the bottom of a $(10\bar{1}0)$ step. Only the lower $TiSe_2$ layer is shown.

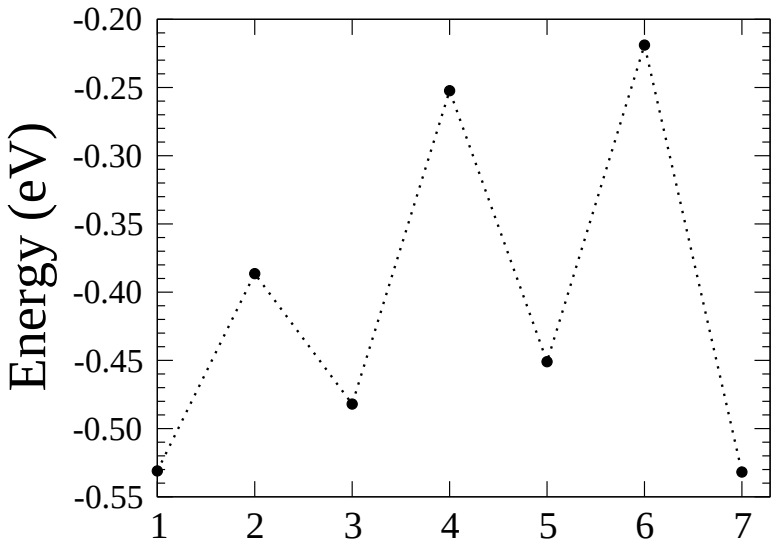

Figure 6.9: Energy plot of the diffusion along the bottom of a $(10\bar{1}0)$ step. The position of the Li atom (x-axis) are referred to Figure (6.8). The energies are relative to the *hcp* on-surface site energy.

6.3 $TiSe_2$ (0001) surface with a $(\bar{1}2\bar{1}1)$ step

6.3.1 Simulation of a $(\bar{1}2\bar{1}1)$ $TiSe_2$ oriented step

In order to assess the activation energy that a Li adatom requires to diffuse across and along a $TiSe_2$ step facing a $(\bar{1}2\bar{1}1)$ plane, total energy calculations have been

performed within the supercell approximation. A (0001) $TiSe_2$ surface with a $(\bar{1}2\bar{1}1)$ oriented step was simulated by a repeating slab, composed by two layers of $TiSe_2$, and a 17 a_B vacuum region. In the lateral $[\bar{1}010]$ direction two $TiSe_2$ unit cells (Se-Ti-Se) were taken, while in the $[\bar{1}2\bar{1}0]$ direction four $TiSe_2$ unit cells were used for the top layer and six for the bottom layer, giving a total of 40 Se and 20 Ti atoms. The lattice constants of the $TiSe_2$ unit cell used here are the same as for the $(10\bar{1}0)$ step ($a = 6.61$ a_B and $c = 11.90$ a_B). When calculating the diffusion energy of Li adatom on the first layer, the result is comparable with the diffusion on the flat (0001) surface. Therefore, the size of the first layer gives a right description of this surface. The distance between the atoms in the step edge and the next cell in *y*-direction is of about 15 a_B, thus a Li adatom at this step edge can be considered isolated, Because of the large size of this supercell only one special **k** point in the surface Brillouin zone was sufficient to give energy differences, which were within 0.05 eV of those obtained by using two or four times the number of **k** points. The 30 Ry plane wave cutoff was tested to give adsorption energies differences to a numerical accuracy better than 0.05 eV.

6.3.2 Relaxation of the $TiSe_2$ (0001) surface with a $(\bar{1}2\bar{1}1)$ step

For the $(\bar{1}2\bar{1}1)$ step the first $TiSe_2$ slab was full relaxed as well as the first atomic plane of the second layer. The two atomic planes in the second layer were fixed at the bulk positions obtained for $TiSe_2$ fully intercalated with Li. In Figure (6.10) a schematic representation of the structure is shown. Here the numbered atoms were the ones that presented a displacement, with the exception of Se(4) atom that was kept fixed. The nearest neighbors (in the *x*-direction) of the numbered atoms moved together with these ones.

In this step only the atoms located at the edge, Se (1,2) and Ti(1), showed a large deviation from the positions obtained for the flat surface. The values of these deviations are resumed in Table 6.2. The Se atoms (1 and 2) moved in *z* direction toward Ti(1) reducing the thickness of the first layer from 5.7 to 5.16 a_B, while the Ti(1) atom is displaced toward the bulk and away from the step edge. The deviations of the Se(5,6)- and Ti(2)-atomic positions from the flat surface are small, which has made possible to use only four unit-cell along the *y*-axis to represent the (0001) stepped surface.

6.3.3 Li diffusion across and along a $(\bar{1}2\bar{1}1)$ step

Among many possible pathways for Li surface diffusion, Figure (6.11) shows the pathway which gives the lowest potential barrier. The points that are situated on the surface are labeled by s_i, while those at the van der Waal gap by g_i. In Figure (6.12) a top view of this pathway is displayed, showing in the upper picture the diffusion positions on the (0001) surface and on the descending step. In the lower picture three paths at the van der Waals gap are depicted: one indicates the way within the van der Waals gap, representing the intercalation path, the second one the diffusion away from the step,

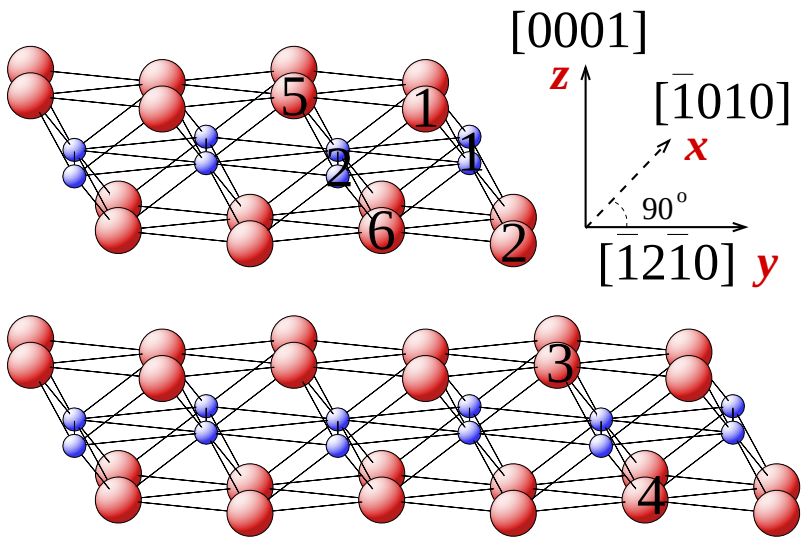

Figure 6.10: Geometry of the (0001) surface with a $(\bar{1}2\bar{1}1)$ step. The red and blue spheres represent Se and Ti atoms, respectively. Some atoms are numbered to facilitate the description of their relaxations, (see Table 6.2).

Atom	Δ x	Δ y	Δ z
Se			
1	0.0	0.07	-0.50
2	0.0	0.23	0.27
3	0.0	0.0	0.04
4	-	-	-
5	0.0	0.03	0.04
6	0.0	-0.05	-0.04
Ti			
1	0.0	-0.30	-0.68
2	0.0	-0.04	-0.06

Table 6.2: Atomic displacements with respect to the $TiSe_2$ (0001) surface positions (in a_B). The Se and Ti indices are referred to Figure (6.10). The first layer and the first (Se) atomic plane of the second layer were allowed to relax.

and the third one the path along the edge of the step. In Figure (6.13) the total energy of the system along the diffusion path is shown, as well as the height of the Li adatom

with respect to the Ti-plane (first layer). The adsorption energy at s_0 is taken as the zero energy reference.

In these calculations the diffusion barrier of the Li adatom on the (0001) surface is comparable with that on the flat surface. The Li adatom starts the diffusion path at s_0, an *hcp* adsorption site on the (0001) surface, overcomes a barrier of 0.25 eV at the *brigde* site (s_1), and reaches an fcc adsorption site (s_2). Again it diffuses to a bridge site s_3 with an energy cost of 0.25 eV. At this site the Li adatom begins descending the step, meeting at s_6 an additional potential barrier of 0.31 eV, the so-called Ehrlich-Schwoebel barrier. Once the adatom reaches the s_6, it continues diffusing along the $(\bar{1}2\bar{1}1)$ surface without barrier, until it approaches the van der Waals gap, where it can either intercalate within the $TiSe_2$ layers or diffuse on the lower terrace. At g_5 is the

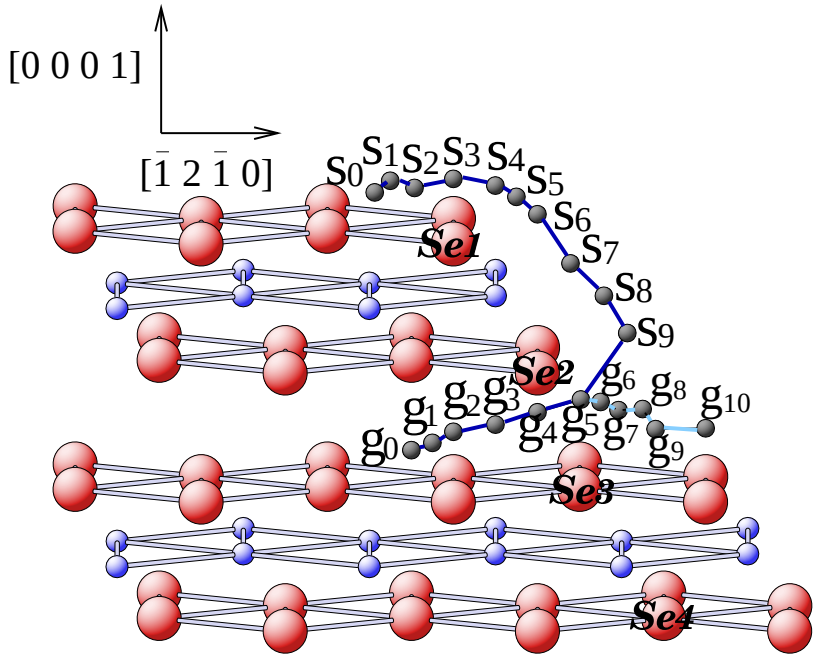

Figure 6.11: Schematic illustration of the sites involved in the diffusion of Li across a $TiSe_2$ $(\bar{1}2\bar{1}1)$ step. Points labeled by s_i and g_i are on the (0001) surface and in the van der Waals gap, respectively. The dark blue line joining the points represents the diffusion path with minimum energy. The light-blue line joints the points of the diffusion path on the second terrace. The red and blue spheres stand for selenium and titanium atoms, respectively.

site where the Li adatom reaches the van der Waals gap, with an energy gain of -0.43 eV. To move between the layers and reach g_3, an octahedral site with an energy of -0.58 eV, the Li adatom has to overcome a small barrier of 0.05 eV at g_4. To leave the stable octahedral site toward g_0 the adatom encounters at g_1 a barrier of 0.6 eV, which

is 0.19 eV higher than the barrier found for diffusion along the van der Waals gap without steps. To diffuse in the opposite direction, i.e. away from the step, the adatom finds a barrier of 0.17 eV at g_6. It reaches then g_7 a stable site -0.52 eV deeper than the reference site. This stable site is separated by a barrier of 0.7 eV from the nearest terrace site, therefore the probability for detachment from this step edge is relatively low.

However, also for the $(\bar{1}2\bar{1}1)$ step there is the possibility that the adatom diffuses along its edge with a diffusion barrier equal to that of the flat surface (0.25 eV). The path along the edge involves hopping from site g_5 to g_7 surmounting the barrier of 0.17 eV at g_6, and from g_7 to g_5' via g_6', with an energy cost of 0.25 eV, (where g_5' and g_6' are mirror-symmetric to g_5 and g_6), see Figure (6.12).

Site	Li-Se bonds	bond length			
s_0	3	4.7	4.7	4.6	
s_1	2	4.4	4.5		
s_2	3	4.6	4.5	4.5	
s_3	2	4.5	4.4		
s_4	2	4.5	4.5		
s_5	2	4.7	4.7		
s_6	2	5.0	5.0		
s_7	2	4.9	4.9		
s_8	2	4.6	4.6		
s_9	2	4.5	4.5		
	van der Waals Gap				
g_0	4	4.4	4.4	4.4	4.3
g_1	3	4.3	4.3	4.3	
g_2	3	4.4	4.4	4.2	
g_3	6	5.0	5.0	5.0	
		4.9	4.9	4.9	
g_4	3	4.6	4.6	4.4	
g_5	3	4.6	4.6	4.7	
g_6	2	4.4	4.5		
g_7	4	4.9	4.9	4.7	5.0
g_8	2	4.8	4.8		
g_9	3	4.6	4.9	4.9	
g_{10}	2	4.5	4.5		

Table 6.3: Number of Li-Se bonds and bond lengths (in a_B).

In Table 6.3 the number of Li-Se bonds at each site, as well as their length are given. On the (0001) surface the more stable sites are at the three-fold sites (*hcp* and

fcc) with longer bonds in the first one, due to the adatom's proximity to a Ti atom. When the adatom moves from s_2 to the step edge its coordination changes from three to two, giving rise to an increase in the energy. Until the adatom reaches the higher energy site (s_6), the bond lengths increase together with the energy. From this barrier site until the adatom reaches the van der Waals gap the two-fold coordination is kept but with decreasing bond lengths. At the van der Waals gap the energy decreases with increasing coordination number. Therefore the most stable site is the octahedral, where the Li adatom binds with six Se atoms.

6.4 Conclusions

The investigation of diffusion barriers along several paths in the vicinity of $(10\bar{1}0)$ and $(\bar{1}2\bar{1}1)$ steps shows that there exists a difference in approaching both steps. For the $(10\bar{1}0)$ step the Li adatom encounters a negative Schwoebel barrier, which enhances its incorporation to the lower terrace. In contrast to this, to approach the $(\bar{1}2\bar{1}1)$ step the adatom has to overcome an Ehrlich-Schwoebel barrier of 0.31 eV. On the other hand, once the adatom reaches the van der Waals gap, its migration within the gap is energetically favoured against continuing diffusion along the lower terrace, independently from the orientation of the step. In both steps, it was obtained that the adatom occupies the first octahedral site near the step bottom and requires 0.54-0.60 eV for moving to another site. This energy represents the diffusion barrier within the gap and demonstrates the stability of the octahedral site. Moreover, to diffuse away from the steps, i.e. along the lower terrace the adatom finds an initial barrier of about 0.7 eV. This barrier is significantly higher than within the gap, so the probability that the Li adatom is detached from the step bottoms is relative low.

The Li diffusion along both step bottoms was also investigated. In both cases the adatom can diffuse with a barrier comparable with that on the (0001) surface (about 0.25 eV). For the $(10\bar{1}0)$ step, the potential seen by the alkali adatom is not inversion symmetric. In the $(\bar{1}2\bar{1}0)$ direction the diffusion barrier is 0.24 eV, while in the opposite moving the barrier increases to 0.32 eV. For the $(\bar{1}2\bar{1}1)$ step, the barrier to diffuse is 0.25 eV.

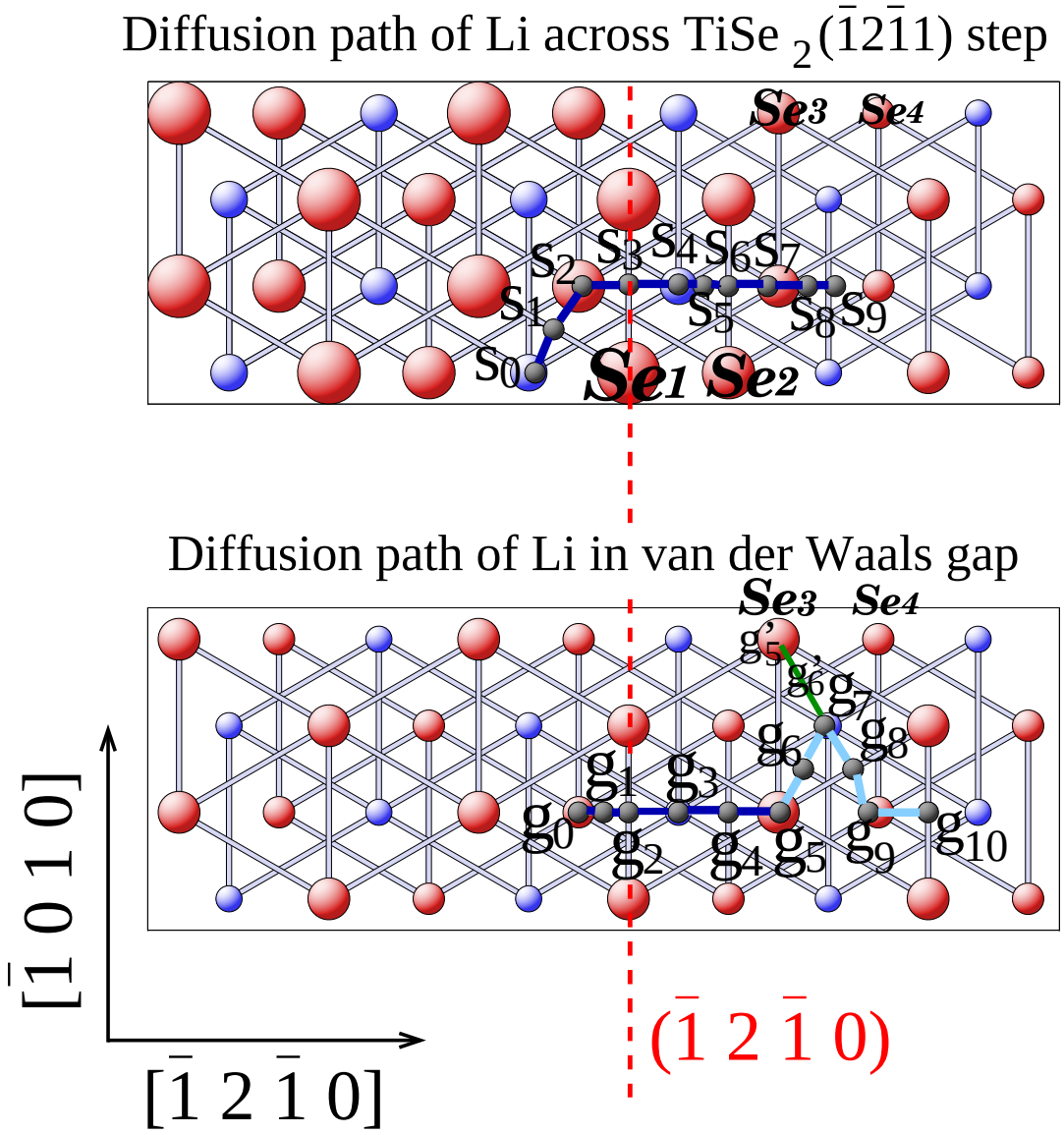

Figure 6.12: Top view of the sites on the (0001) surface and $(\bar{1}2\bar{1}1)$ step. The red and blue spheres stand for selenium and titanium atoms, respectively. Their size decreases according to their distance from the surface. (bottom) Top view of the sites in the van de Waals gap. The seleniums with indices are at the surface's edges. The dark blue line joining the points represents the diffusion path with minimum energy. The light-blue line joints the points of the diffusion path on the second terrace. The green line shows the alternative path paralell to the step edge.

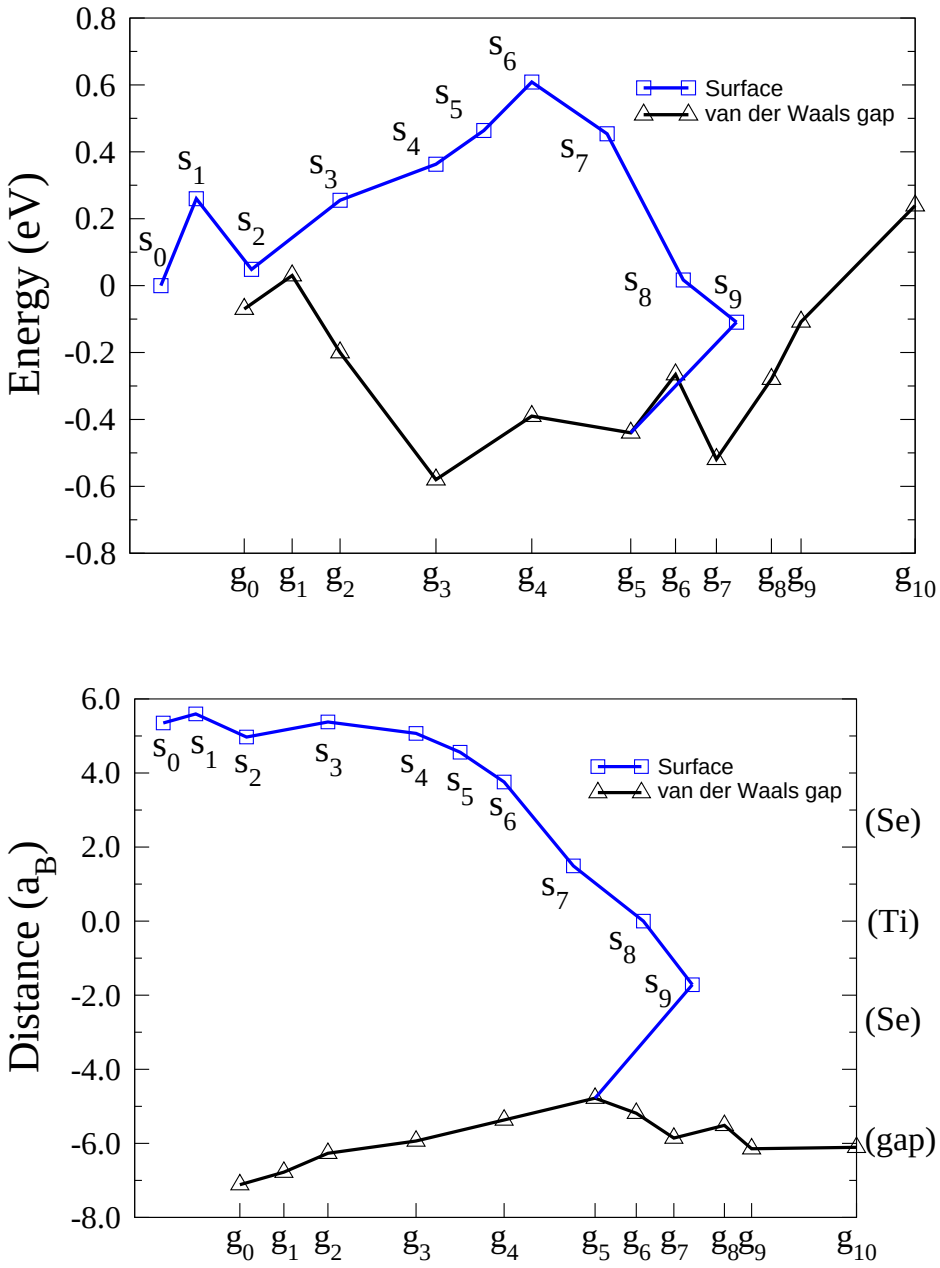

Figure 6.13: (top) Total energy for a Li diffusing on the (0001) surface along a $(\bar{1}2\bar{1}1)$ $TiSe_2$ step, and in the van der Waals gap. The zero energy corresponds to the s_2 site, which has the minimum energy in the surface. The points on the surface and in the van der Waals gap are labeled by s_i and g_i, respectively. (bottom) The height of Li adatom in the diffusion path, with respect to the Ti plane position in the first sandwich. The position of the selenium and titanium atomic planes in the first sandwich of $TiSe_2$ and of the van der Waals gap are marked at the right axis of the graphic.

Chapter 7

Conclusions

The diffusion mechanisms that are relevant to alkali metal intercalation in $TiSe_2$ have been investigated by means of *ab initio* total-energy calculations. The adsorption sites and the diffusion barriers along several paths for hopping processes on the flat surface, on surfaces with $(10\bar{1}0)$ and $(\bar{1}2\bar{1}1)$ steps, as well as in the van der Waals gap have been calculated.

Since the problem of surface diffusion is intimately related to the morphology of the surface on which this process takes place, the optimization of $TiSe_2$ (0001) geometry has been first addressed. Furthermore, extensive and detailed calculations of Li adsorbed on this surface at coverages ranging from 0.06 to 1 ML have been presented. The change in the work function with Li coverage can be well described by the Langmuir-Gurney model; at low coverages Φ decreases until it reaches a minimum around Θ=0.5 ML, and then increases approaching the value of the bulk alkali metal.

Two adsorption sites have been obtained on the $TiSe_2$ (0001) surface: hcp and fcc. For Li adatom the hcp site is slightly energetically preferred over the fcc, while for Na, Rb, and Cs both sites have the same adsorption energy. The surface diffusion path between two hcp sites runs via the direct connection of an adjacent hcp and fcc site over a bridge site: $hcp \rightarrow bridge \rightarrow fcc \rightarrow bridge \rightarrow hcp \ldots$. It has been found that the energy barrier for alkali metal diffusion range from 0.26 eV for Li to 0.01 eV for Cs.

In the van der Waals gap there are three equilibrium sites: one octahedral and two tetrahedral sites, where the first is energetically strongly preferred. The corresponding binding energies for all these sites, are markedly lower than the ones in the surface. This fact demonstrates the strong tendency of $TiSe_2$ towards intercalation and the stability of the intercalated compound. To diffuse away from the octahedral site the Li atom has to overcome a barrier of 0.42 eV.

Once the equilibrium sites in the surface and in the van der Waals gap were determined, the intercalation path of Li adatom within $TiSe_2$ atomic layers was investigated. Because of the large energy barrier involved in this process (3.81 eV), this type of intercalation can be excluded.

A second possible intercalation path has been investigated, namely via surface

steps. The diffusion of Li adatom across and along two different steps, $(10\bar{1}0)$ and $(\bar{1}2\bar{1}1)$ steps, has been studied. For the $(10\bar{1}0)$ step the Li adatom encounters a negative Ehrlich-Schwoebel barrier, which enhances its incorporation to the lower terrace. Contrarily, to approach the $(\bar{1}2\bar{1}1)$ step the adatom has to overcome an Ehrlich-Schwoebel barrier of 0.31 eV. However, once the adatom reaches the van der Waals gap, its migration within the gap (and therefore intercalation), is energetically favoured against continuing diffusion along the lower terrace, independently from the orientation of the step. For both steps the adatom occupies the first octahedral site near the step bottom, which is a thermodynamically stable site in the van der Waals gap. To continue diffusing along the van der Waals gap, the adatom has to overcome the corresponding diffusion barrier.

The diffusion of Li adatom along the bottom edge of both steps was also investigated. In both cases the adatom can diffuse with a barrier comparable with that on the (0001) flat surface. For the $(10\bar{1}0)$ lower step edge, there exists a non inversion symmetric potential.

To summarize, Li adatoms can intercalate into $TiSe_2$ without any additional energy barrier via a $(10\bar{1}0)$ step.

List of Tables

List of Figures

Bibliography

[1] J.A. Wilson and A.D. Yoffe
The transition metal dichalcogenides. Discussion and interpretation of the observed optical, electrical and structural properties.
Adv. Phys. **18** 193 (1969).

[2] W.Y. Liang
Intercalation in Layered Materials, edited by M.S. Dresselhaus (New York: Plenum 1986) p 31.

[3] R.A. Bromley and R.B. Murray
The band structures of some transition metal dichalcogenides. I. A semiempirical tight binding method
J. Phys. C: Solid St. Phys. **5**, 738 (1972).

[4] L.F. Mattheiss
Band Structures of Transition-Metal-Dichalcogenide Layer Compounds
Phys. Rev. B **8**, 3719 (1973).

[5] A. Zunger, A.J. Freeman
Self-consistent numerical-basis-set linear-combination-of-atomic-orbitals investigation of the electronic structure and properties of TiS_2
Phys. Rev. B **16**, 906 (1977).

[6] E. Pehlke and W. Schattke O. Anderson, R. Manzke, and M. Skibowski
Photoemission from the (001) surface of 1T-$TiSe_2$: Comparison of calculation with experiment
Phys. Rev. B **41**, 2982 (1990).

[7] M. Traving, M. Boehme, L. Kipp, M. Skibowski, F. Starrost, E.E. Krasovskii, A. Perlov, and W. Schattke
Electronic structure of WSe_2: A combined photoemission and inverse photoemission study
Phys. Rev. B **55**, 10392 (1997).

[8] O.Anderson, R. Manzke, and M. Skibowski
Three-Dimensional and Relativistic Effects in Layered 1T-$TiSe_2$
Phys. Rev. Lett. **55**, 2188 (1985).

[9] W. Drube, I. Schäfer, G. Karschnick, and M. Skibowski
Inverse photoemission study of the conduction bands in $TiSe_2$
Phys. Rev. B **30**, 6248 (1984).

[10] D. Straub, M. Skibowski, F.J. Himpsel, and W. Drube
Interlayer interaction in the conduction bands of layered transition-metal dichalcogenides studied by inverse photoemission
Phys. Rev. B **31**, 8254 (1985).

[11] M.S. Whittingham
Electrical Energy Storage and Intercalation Chemistry
Science **192**, 1126 (1976).

[12] M.S. Whittingham and L.B. Ebert
Intercalated Layered Materials, edited by F. A. Levy (Dordrecht: Reidel 1979).

[13] W. Jaegermann, C. Pettenkofer, A. Schellengerger, C.A. Papageorgopoulos, M. Kamaratos, D. Vlachos, Y. Tomm
Photoelectron spectroscopy of UHV in situ intercalated Li/$TiSe_2$. Experimental proof of the rigid band model
Chem. Phys. Letters **221**, 441-446 (1994).

[14] H.I. Starnberg and H.P. Hughes
Photo-emission study of in situ intercalation of TiS2 with Ag
J. Phys. C: Solid St. Phys. **20**, 4429 (1987).

[15] C. Pettenkofer, W. Jaegermann, A. Schellenberger, E. Holub-Krappe, C.A. Papageorgopoulos, M. Kamaratos, and A. Papageorgopoulos
Cs deposition on layered 2H $TaSe_2$ (0001) surfaces: adsorption or intercalation?
Solid State Commun. **84**, 921 (1992).

[16] A. Schellenberger, W. Jaegermann, C. Pettenkofer, C.A. Papageorgopoulos, and M. Kamaratos
Alkali intercalation into layered compounds: UHV in-situ preparation and reactivity
Ber. Bunsenges. Phys. Chem. **96** No. 11, 1755 (1992).

[17] R. Adelung, L. Kipp, J. Brandt, L. Tarcak, M. Traving, C. Kreis, and M. Skibowski
Nanowire networks on perfectly flat surfaces
Appl. Phys. Lett. **74**, 3053 (1999).

[18] R. Adelung, J. Brandt, K. Roßnagel, O. Seifarth, L. Kipp, M. Skibowski, C. Ramírez, T. Strasser, and W. Schattke
Tuning dimensionality by nanowire adsorption on layered materials
Phys. Rev. Lett. **86**, 1303 (2001).

[19] H. Brauer, PhD. Thesis, Göteborg University and Chalmers University of Technology, Göteborg (1996).

[20] N. Troullier and J. L. Martins
Efficient pseudopotentials for plane-wave calculations
Phys. Rev. B **43**, 1993 (1991).

[21] M. Born and R. Oppenheimer
Zur Quantentheorie der Molekeln
Ann. Phys. **84** (20), 457 (1927).

[22] P. Hohenberg and W. Kohn
Inhomogeneous Electron Gas
Phys. Rev. **136**, B864 (1964).

[23] P. W. Kohn and L. J. Sham
Self-Consistent Equations Including Exchange and Correlation Effects
Phys. Rev. **140**, A1133 (1965).

[24] J. P. Perdew and A. Zunger
Self-interaction correction to density-functional approximations for many-electron systems
Phys. Rev. B **23**, 5048 (1981).

[25] D. M. Ceperley and B. J. Alder
Ground State of the Electron Gas by a Stochastic Method
Phys. Rev. Lett. **45**, 566 (1980).

[26] H.J. Monkhorst and J.D. Pack
Special points for Brillouin-zone integrations
Phys. Rev. B **13**, 5188 (1976).

[27] U. von Barth and C.D. Gelatt
Validity of the frozen-core approximation and pseudopotential theory for cohesive energy calculations
Phys. Rev. B **21**, 2222 (1980).

[28] D.R. Hamann, M. Schlüter, and C. Chiang
Norm-Conserving Pseudopotentials
Phys. Rev. Lett. **43**, 1494 (1979).

[29] G.B. Bachelet, D.R. Hamann, and M. Schlüter
Pseudopotentials that work: From H to Pu
Phys. Rev. B **26**, 4199 (1982).

[30] D. Vanderbilt
Soft self-consistent pseudopotentials in a generalized eigenvalue formalism
Phys. Rev. B **41**, 7892 (1990).

[31] X. Gonze, R. Stumpf, and M. Scheffler
Analysis of separable potentials
Phys. Rev. B **44**, 8503 (1991).

[32] M. Teter
Additional condition for transferability in pseudopotentials
Phys. Rev. B **48**, 5031 (1993).

[33] A. Filippetti, D. Vanderbilt, W. Zhong, and Y. Cai
Chemical hardness, linear response, and pseudopotential transferability
Phys. Rev. B **52**, 11793 (1995).

[34] L. Kleinman and D.M. Bylander
Efficacious Form for Model Pseudopotentials
Phys. Rev. Lett. **48**, 1425 (1982).

[35] X. Gonze, P. Käckel and M. Scheffler
Ghost states for separable, norm-conserving, ab initio pseudopotentials
Phys. Rev. B **41**, 12264 (1990).

[36] R. Car and M. Parrinello
Unified approach for molecular dynamics and density-functional theory
Phys. Rev. Lett. **55**, 2471 (1985).

[37] S. Kirkpatrick, C.D. Gelatt, Jr., and M.P. Vecchi
Optimization by Simulated Annealing
Science **220**, 671 (1983).

[38] L. Verlet
Computer "Experiments" on Classical Fluids. I. Thermodynamical Properties of Lennard-Jones Molecules
Phys. Rev. **159**, 98 (1967).

[39] M. C. Payne, M. P. Teter, D. C. Allan, T. A. Arias and J. D. Joannopoulos
Iterative minimization techniques for ab initio total-energy calculations: molecular dynamics and conjugate gradients
Rev. Mod. Phys. **64**, 1045 (1992).

[40] I. Stich, R. Car, M. Parrinello, and S. Baroni
Conjugate gradient minimization of the energy functional: A new method for electronic structure calculation
Phys. Rev. B **39**, 4997 (1989).

[41] M.P. Teter, M.C. Payne, D.C. Allan
Solution of Schrödinger's equation for large systems
Phys. Rev. B **40**, 12255 (1989).

[42] M.J. Gillan
Calculation of the vacancy formation energy in aluminium
J. Phys.: Condens. Matter **1**, 689 (1989).

[43] A. Williams and J. Soler
Bull. Am. Phys. Soc. **32**, 562 (1987).

[44] H. Hellmann
Einfuhrung in die Quantumchemi, (Deutickem Leipzig), 1937.

[45] R.P. Feynman
Forces in Molecules
Phys. Rev. **56**, 340 (1939).

[46] M. Bockstedte, A. Kley, J. Neugebauer, and M. Scheffler
Density-functional theory calculations for poly-atomic systems: electronic structure, static and elastic properties and ab-initio molecular dynamics
Comp. Phys. Comm. **107**, 187 (1997).

[47] P. Kratzer, C.C. Morgan, E. Penev, A.L. Rosa, A. Schindlmayr, L.G. Wang, and T. Zywietz
FHI98MD, *Computer code for density-functional theory calculations for poly-atomic systems User's Manual*
Fritz-Haber-Institut der Max-Planck-Gesellschaft, Berlin, 1999.

[48] C.M. Fang, R.A. de Groot, and C. Haas
Bulk and surface electronic structure of 1T-TiS_2 and 1T-$TiSe_2$
Phys. Rev. B **56**, 4455 (1997).

[49] Cyrus Umrigar, D.E. Ellis, Ding-Sheng Wang, H. Krakauer, and M. Posternak
Band structure, intercalation, and interlayer interactions of transition-metal dichalcogenides: TiS_2 and $LiTiS_2$
Phys. Rev. B **26**, 4935 (1982).

[50] S. Sharma, T. Nautiyal, G.S. Singh, S. Auluck, P. Blaha, and C. Ambrosch-Draxl
Electronic structure of 1T-TiS_2
Phys. Rev. B **59**, 14833 (1999).

[51] T. Hibma
Structural aspects of monovalent cation intercalates of layered dichalcogenides in *Intercalation Chemistry*
edited by M.S. Whittingham and A.J. Jacobson, (Academic Press, London 1982).

[52] R.H. Friend and A.D. Yoffe
Electronic properties of intercalation complexes of the transition metal dichalcogenides
Adv. Phys. **36**, 1 (1987).

[53] H.I. Starnberg, H.E. Brauer, L.J. Holleboom and H.P. Huges
3D-to-2D transition by Cs intercalation of VSe_2
Phys. Rev. Lett. **70**, 3111 (1993).

[54] H.E. Brauer, H.I. Starnberg, L.J. Holleboom, and H.P. Hughes
In situ intercalation of the layered compounds TiS_2, $ZrSe_2$ and VSe_2
Surf. Sci. **331-333**, 419 (1995).

[55] J. Rouxel
Structural Chemistry of layered materials and their intercalates
Physica B **99**, 3 (1980).

[56] F.J. Di Salvo, D.E. Moncton, J.V. Waszczak
Electronic properties and superlattice formation in the semimetal $TiSe_2$
Phys. Rev. B **14**, 4321 (1976).

[57] M. S. Whittinghan and F. R. Gamble
The lithium intercalated of the transition metal dichalcogenides
Mater. Res. Bull. **10**, 363 (1975).

[58] R.B. Murray and A.D.Yoffe
The band structures of some transition metal dichalcogenides: band structures of the titanium dichalcogenides
J. Phys. C: Solid St. Phys. **5** 3038 (1972).

[59] H.W. Myron and A.J. Freeman
Electronic structure and optical properties of layered dichalcogenides: TiS_2 and $TiSe_2$
Phys. Rev. B **9**, 481 (1974).

[60] A. Zunger, A. J. Freeman
Band structure and lattice instability of $TiSe_2$
Phys. Rev. B **17**, 1839 (1978).

[61] H. Isomäki, J. von Boehm, and P. Krusius
Band structure of group IVA transition-metal dichalcogenides
J. Phys. C: Solid St. Phys. **12** 3239 (1979).

[62] G.A. Benesh, A.M. Woolley, and C. Umrigar
The pressure dependences of TiS2 and TiSe2 band structures
J. Phys. C: Solid St. Phys. **18** 1595 (1985).

[63] R.Z. Bachrach, M. Skibowski F.C. Brown
Angle-Resolved Photoemission from $TiSe_2$ Using Synchrotron Radiation
Phys. Rev. Lett. 37, 40-42 (1976).

[64] M.M. Traum, G. Margaritondo, N.V. Smith, J.E. Rowe, and F.J. Di Salvo
$TiSe_2$: Semiconductor, semimetal, or excitonic insulator
Phys. Rev. B **17**, 1836 (1978).

[65] C.H. Chen, W. Fabian, F.C. Brown, K.C. Woo, B. Davies, B. DeLong, and A.H. Thompson
Angle-resolved photoemission studies of the band structure of $TiSe_2$ and TiS_2
Phys. Rev. B **21**, 615 (1980).

[66] M. Fuchs and M. Scheffler
Ab initio pseudopotentials for electronic structure calculations of poly-atomic systems using density-functional theory
Comput. Phys. Commun. **119**, 67-98 (1999).

[67] S.C. Louie, S. Froyen, and M.L. Cohen
Nonlinear ionic pseudopotentials in spin-density-functional calculations
Phys. Rev. B **26**, 1738 (1982).

[68] W.B. Pearson
A Handbook of lattice spacings and structures of metals and alloys
Pergamon Press, Inc., New York, 1958.

[69] L.F. Mattheiss
Energy Bands for the Iron Transition Series
Phys. Rev. **134**, A970 (1964).

[70] R. Ahuja, O. Eriksson, J.M. Wills, and B. Johansson
Structural, elastic, and high-pressure properties of cubic TiC, TiN, and TiO
Phys. Rev. B **53**, 3072 (1996).

[71] R. Schlaf, A. Klein, C. Pettenkofer, and W. Jaegermann
Laterally inhomogeneous surface-potential distribution and photovoltage at clustered In/WSe_2(0001) interfaces
Phys. Rev. B **48**, 14242 (1993).

[72] G. Prasad and O. Srivastava
The high-efficiency (17.1%) WSe_2 photo-electrochemical solar cell
J. Phys. D **21**, 1028 (1988).

[73] L. Rapoport, Y. Bilik, Y. Feldman, M. Homyonfer, S. R. Cohen and R. Tenne
Hollow nanoparticles of WS_2 as potential solid-state lubricants
Nature **387**, 791 (1997).

[74] S. R. Cohen, Y. Feldman, H. Cohen and R. Tenne
Nanotribology of novel metal dichalcogenides
Appl. Surf. Sci. **145**, 603 (1999).

[75] H. Tributsch
Z. Naturforsch. **32a**, 972 (1977).

[76] S. Kennou, S. Ladas, and C. A. Papageorgopoulos
The behavior of Cs on MoS_2
Surf. Sci. **152-153** , 1213 (1985).

[77] C. Papageorgopoulos, M. Kamaratos, A. Papageorgopoulos, A. Schellenberger, E. Holub-Krappe, C. Pettenkofer, and W. Jaegermann
Adsorption of Cs on WSe_2 van der Waals surfaces: temperature and sputter effects on growth properties Surf. Sci. **275**, 314 (1992).

[78] A. Koma, K. Sunouchi, and T. Miyajima
Fabrication of ultrathin heterostructures with van der Waals epitaxy
J. Vac. Sci. Technol. B 3, 724 (1985).

[79] M. Whittinghan
Chemistry of intercalation compounds: metal guests in chalcogenide hosts
Prog. Solid State Chem. **12**, 41 (1978).

[80] J. Neugebauer and M. Scheffler
Adsorbate-substrate and adsorbate-adsorbate interactions of Na and K adlayers on Al(111)
Phys. Rev. B **46**, 16067 (1992).

[81] S. L. Cunningham
Special points in the two-dimensional Brillouin zone
Phys. Rev. B **10**, 4988 (1974).

[82] N. W. Ashcroft, N. D. Mermin
Solid State Physics, Holt Rinehart and Winston, 1976.

[83] I. Langmuir
J. Am. Chem. Soc. **54**, 2798 (1932).

[84] R.W. Gurney
Theory of Electrical Double Layers in Adsorbed Films
Phys. Rev. **47**, 479 (1935).

[85] C.A. Papageorgopoulos and J.M. Chen
Coadsorption of electropositive and electronegative elements; II. Cs and O_2 on W (100)
Surf. Sci. **39**, 313 (1973).

[86] C.A. Papageorgopoulos and J.M. Chen
Coadsorption of cesium and oxygen on Ni(100); I. Cesium probing of Ni—O bonding
Surf. Sci. **52**, 40 (1975).

[87] *CRC Handbook of Chemistry and Physics*
64th edition. CRC Press, Boca Raton, FL, 1983.

[88] M. Dacorogna and M. Cohen
First-principles study of the structural properties of alkali metals
Phys. Rev. B **34**, 4996 (1986).

[89] T. Hibma
Ordering of the alkali ions in Na_xTiS_2 and Li_xTiS_2
Physica B **99**, 136 (1980).

[90] A. Schellenberger, R. Schlaf, C. Pettenkofer, and W. Jaegermann
Synchrotron-induced surface-photovoltage saturation at intercalated Na/WSe_2 interfaces
Phys. Rev. B **45**, 3538 (1992).

[91] H.E. Brauer, I. Ekvall, H. Olin, H.I. Starnberg, E. Wahlström, H.P. Hughes, and V.N. Strocov
Na intercalation of VSe_2 studied by photoemission and scanning tunneling microscopy
Phys. Rev. B **55**, 10022 (1997).

[92] H.E. Brauer, H.I. Starnberg, L.J. Holleboom, V.N. Strocov, and H.P. Hughes
Electronic structure of pure and alkali-metal-intercalated VSe_2
Phys. Rev. B **58**, 10031 (1998).

[93] C. Pettenkofer and W. Jaegermann
Charge-density-wave transformation induced by Na intercalation into 1T-TaS_2
Phys. Rev. B **50**, 8816 (1994).

[94] M. Bronold, C. Pettenkofer, and W. Jaegermann
Alkali metal intercalation into SnS_2 UHV Investigations of (0001) Surfaces
Appl. Phys. A **52**, 171 (1991).

[95] H.E. Brauer, H.I. Starnberg, H.P. Hughes, L.J. Holleboom
Band mapping of in situ Cs intercalated transition metal dichalcogenides
Surf. Sci. **357-358**, 345 (1996).

[96] P. Blaha
Electronic structure and electric field gradients in 2H-TaS_2, $LiTaS_2$ and $SnTaS_2$
J. Phys.: Condens. Matter **3**, 9381 (1991).

[97] T. Butz, A. Vasquez, H. Saitovitch, R. M̈hlberger and A. Lerf
Perturbed angular correlation studies of layered compunds and intercalates
Physica B and C **99**, 69 (1980).

[98] J.E. Fischer and H.J. Kim
Elastic effects in intercalation compounds: Comparison of lithium in graphite and TiS_2
Phys. Rev. B **35**, 3295 (1987).

[99] A. Schellenberger, PhD. Thesis, Freie Universität, Berlin (1992).

[100] M. Boehme, PhD. Thesis, Christian-Albrechts-Universität, Kiel (1998).

[101] D. Tonti, PhD. Thesis, Freie Universität, Berlin (2000).

[102] H.H. Weitering
Growth and electronic structure of some monovalent metals on TiS_2 (001)
J. Phys.: Condens. Matter **3**, 8535 (1991).

[103] A. Herold
Chemical Physics of Intercalation, Vol. B 172 edited by A.P. Legrand and S. Flandrois (New York: Plenum Press 1987)

[104] W. Rudorff and H.H. Sick
Angew. Chem. **71**, 127 (1959).

[105] J. Rouxel
Intercalated Layered Materials, edited by F.A Levy, 1979, p. 201.

[106] Z.Y. Wu, G. Ouvrard, S. Lemaux, P. Moreau, P. Gressier, F. Lemoigno, and J. Rouxel
Sulfur K-edge X-ray-absorption study of the charge transfer upon lithium intercalation into titanium disulfide
Phys. Rev. Lett. **77**, 2101 (1996).

[107] M. Remškar, A. Popović, H.I. Starnberg
Stacking transformation and defect creation in Cs intercalated TiS_2 single crystals
Surf. Sci. **430**, 199 (1999).

[108] M.V. Koudriachova, N.M. Harrison, and Simon W. de Leeuw
Effect of diffusion on lithium intercalation on titanium dioxide
Phys. Rev. Lett. **86**, 1275 (2001).

[109] R. Adelung and L. Kipp
private comunication.

Acknowledgments

I would like to express my sincere gratitude and appreciation to my supervisor, Prof. Dr. W. Schattke, not only for his guidance and keen editorial eye, but also for his encouragement and support throughout the development of this project.

I wish to thank Dr. Rainer Adelung for the fruitfull collaboration that helped me gain a better understanding of the intercalation process. I benefited from discussions with Priv-Doz. Dr. Lutz Kipp.

I thank Prof. Dr. E. Pehlke for his valuable help throughout the course of this work.

I would like also to emphasize the importance of all the members of the group. In particular: Thomas Strasser for his willingness to read all the chapters in detail, for making constructive suggestions to improve various aspects of the thesis and specially for his friendship; Dr. Robert Bahnsen, who helped me with his clearness and organization when I needed it; Dr. Frank Starrost for providing continous thougthful comments and pushing me forward to write my dissertation; Dr. Oliver Tiedje, whose helpful inspiring discussions and suggestions have play a key role in the course of this work. I am especially grateful to Dr. Eugene Krasovskii and Dr. Olga Krasovska for their permanent encouragement.

Sincere thanks are also given to Frau Schulz and Herr Grage for their assistance.

This thesis would not have been possible without the financial support of the mexican National Council for Science and Technology CONACYT.

I thank also my enthusiastic and caring friends: Nicoline Henkel, Eduardo Carrizosa, Inés Franco, Carlos Palacio, Marcela Velázquez, Mauricio y Fernando Toro, and Orgilmaa Dagvadorj . Each of them, in their own way, helped me make this a valuable learning experience.

My sincere gratitude goes to my family: my father for his unconditional support and encouragement to pursue my interests, my mother for her lovely help and her confidence in me, and my sisters for their cheers, and constant care during the course of my research.

I also thank Eduardo for motivating me to be better and for the time we shared together.

Finally, and definitely not least, my biggest thanks go to my daughter Andrea for her patience and for being the catalyst of this work.

Abstract

The aim of this work was to understand how alkali metal atoms intercalate into transition metal dichalcogenides (TMDCs). To this end, a detailed investigation into the geometrical and electronic effects on TMDCs caused by adsorption and intercalation of alkali atoms was carried out by means of ab initio density-functional theory.

The TMDCs have been studied extensively because of their interesting properties such as phase transitions, charge density waves and quasi two-dimensional electronic structures, and because of their potential technological applications in solar cells and batteries. Their structure is built by sandwiches consisting of chalcogen-metal-chalcogen planes forming layers, which are held together by van der Waals interaction. Their layered structure gives them the possibility to form intercalation compounds by acting as host of foreign atoms or molecules. The most modern methods for producing *in situ* TMDCs intercalated compounds had made possible to study the samples in every step of the reaction by means of angle-resolved photoelectron spectroscopy in combination with scanning tunneling microscopy, providing not only new insights into the electronic and geometrical structures of this compounds, but also pointing out the need of a detailed study of the single phenomena involved in the intercalation process.

The calculations here presented are based on the local-density approximation. The interaction between ions and electrons are described using pseudopotentials. Equilibrium configurations are calculated by minimizing the total energy while diffusion paths of the adatoms are determined by the energy of consecutive minima.

The geometrical and electronic properties of clean $TiSe_2$ (0001) surface were studied. Also, the adsorption sites and diffusion of alkali atoms on $TiSe_2$ (0001) surface were computed and compared with those obtained at the van der Waals gap. At the surface, the alkali atoms are adsorbed at the at the hcp and fcc sites, both with similar adsorption energy, hcp slightly preferred. In the intersandwich gap there are two equilibrium sites, the octahedral and tetrahedral position, whose total energies are 0.5 eV higher than at those on the surface. The electron charge distribution caused by alkali atoms on $TiSe_2$ (0001) surface was analysed. A shift of charge from the adsorbate onto the bonding region is observed. The alkali coverage dependence of the physical properties adsorption energy, work function, and valence electron distribution was also studied.

The question of whether the alkali atoms can reach the van der Waals gap from the plain surface through the atomic planes was addressed. Because of the huge energy barrier involved in this process (3.81 eV), this type of intercalation can be excluded. Thus, the experimentally found intercalation processes must be associated with defects, such as steps or dislocations at the surface. The diffusion of Li adatom across and along two different step, $(10\bar{1}0)$ and $(\bar{1}2\bar{1}1)$, was studied. STM experiments favor mainly the two step here considered. For the $(10\bar{1}0)$ step the Li adatom encounters a negative Schwoebel barrier, which enhances its incorporation to the lower terrace. In contrast to this, to approach the $(\bar{1}2\bar{1}1)$ step the adatom has to overcome an Ehrlich-Schwoebel barrier of 0.31 eV. A model of alkali intercalation into TMDCs was obtained, namely via a $(10\bar{1}0)$ step.

Zusammenfassung

Ziel dieser Arbeit ist es zu verstehen, wie Alkalimetallatome in Übergangs-Metall-Dichalkogenid-Schichtkristallen (ÜMDC) interkalieren. Zu diesem Zweck wurde eine ausführliche Untersuchung des Einflusses der Adsorption und Interkalation von Alkali-Atomen auf die geometrische und elektronische Struktur von ÜMDC mittels ab initio Dichte Funktional Theorie durchgeführt.
ÜMDC werden aufgrund ihrer interessanten Eigenschaften, wie Phasenübergänge, Ladungsdichtewellen, ihrer quasi zweidimensionalen elektronischen Struktur und ihrer zahlreichen technischen Anwendungsmöglichkeiten in Solarzellen und Batterien umfassend untersucht. Ihre Struktur besteht aus sandwichartigen Lagen, die jeweils aus Chalkogen-Metall-Chalkogen Ebenen gebildet werden und untereinander von van der Waals Kräften gebunden sind. Diese schichtförmige Struktur ermöglicht die Bildung von Interkalationsverbindungen, indem die ÜMDC als Wirt für Fremdatome oder Moleküle wirken.
Moderne Herstellungsmethoden von in situ ÜMDC Interkalationsverbindungen haben es ermöglicht, die Proben während jeder Phase der Reaktion durch winkelaufgelöste Photoemission gemeinsam mit Rastertunnelmikroskopie zu untersuchen. Dies brachte nicht nur neue Erkenntnisse über die elektronische und geometrische Struktur dieser Kristalle, sondern machte auch deutlich, wie wichtig eine detaillierte Untersuchung der einzelnen Phänomene im Interkalationsprozess ist.
Die Rechnungen in dieser Arbeit basieren auf der Lokalen-Dichte-Approximation. Die Wechselwirkung zwischen Ionen und Elektronen werden durch Pseudopotentiale beschrieben. Gleichgewichtskonfigurationen werden durch Energieminimierung berechnet, die Diffusionspfade der Adatome folgen aus aufeinander folgenden Minima der Gesamtenergie.
Ausgangspunkt ist die Bestimmung der strukturellen und elektronischen Eigenschaften der reinen $TiSe_2$ (0001) Oberfläche. Aufbauend hierzu, werden die Adsorptionsplätze und die Diffusion von Alkaliatomen auf der TiSe2 (0001) Oberfläche berechnet und mit Gesamtenergien für in der van der Waals Lücke eingelagerten Alkaliatomen verglichen. Auf der Oberfläche binden die Alkaliatome an den hcp und fcc Plätzen, beide mit einer vergleichbaren Adsorptionsenergie, die nur etwas größer für die hcp Plätze ist. Innerhalb der van der Waals Lücke gibt es zwei Gleichgewichtsplätze, einen oktaedrischen und einen Tetraederplatz, die energetisch um 0,5 eV günstiger sind, als die Bindungsplätze an der Oberfläche.
Zusätzlich konnte der Einfluß der Alkaliatome auf die Ladungsdichteverteilung der Elektronen an der Oberfläche untersucht werden. Hierbei zeigt sich eine Verschiebung der Ladungsdichte weg von den Alkaliatomen, hin zur Bindung zwischen ihnen und den Chalkogenatomen. Des weitern erlauben die Rechungen, die Abhängigkeit der physikalischen Eigenschaften Adsorptionsenergie, Austrittsarbeit und Ladungsdichteverteilung von der Alkalibedeckung zu analysieren.
Es stellte sich die Frage, wie die Alkaliatome von der ungestörten Oberfläche durch die Atomlagen hindurch, in die van der Waals Lücke gelangen. Aufgrund der großen Energiebarriere (3,81 eV) ist die direkte Interkalation durch die Schichten ausgeschlossen. Daher muss die experimentell gefundene Interkalation an Defekten, wie Stufen oder Versetzungen an der Oberfläche erfolgen. Hierzu wurde die Diffusion von Li Adatomen über und entlang zweier verschiedener Stufen, $(10\bar{1}0)$ und $(\bar{1}2\bar{1}1)$, untersucht. Diese Auswahl legen STM Untersuchungen nahe. Die Rechungen zeigen, dass die Li Atome an der $(10\bar{1}0)$ Stufe eine negative Ehrlich-Schwoebel Barriere spüren, was die Einlagerung auf der unteren Terrasse erleichtert. Im Gegensatz hierzu muß das Adatom an der $(\bar{1}2\bar{1}1)$ Stufe eine Ehrlich-Schwoebel Barriere von 0.31 eV überwinden. Hieraus konnte ein Model für die Interkalation in ÜMDC über $(10\bar{1}0)$ Stufen entwickelt werden.